Università degli studi di Firenze
Dipartimento di Fisica

European Laboratory for
Non-linear Spectroscopy

Dottorato in Fisica
XX ciclo

Sub-wavelength probing and modification of complex photonic structures

Silvia Vignolini

19 February 2009

Settore disciplinare FIS/03

Supervisor Dr. Diederik S. Wiersma

Fisico. Eureca, eureca.
Metafisico. Che è? che hai trovato?
Fisico. L'arte di vivere lungamente.
Metafisico. E cotesto libro che porti?
Fisico. Qui la dichiaro: e per questa invenzione, se gli altri vivranno lungo tempo, io vivró per lo meno in eterno; voglio dire che ne acquisterò gloria immortale.
Metafisico. Fa una cosa a mio modo. Trova una cassettina di piombo, chiudivi cotesto libro, sotterrala, e prima di morire ricordati di lasciar detto il luogo, acciocché vi si possa andare, e cavare il libro, quando sará trovata l'arte di vivere felicemente...

(Giacomo Leopardi "Operette morali: Dialogo di un fisico e un metafisico")

Contents

Introduction

The aim of this thesis consists in the study and modification of complex photonic nanostructures. Nowadays, propagation of light in such materials is a rich and fascinating area of research, both for its fundamental implications and for its practical technological impact. To deeply investigate light propagation inside these structures a high spatial resolution technique is required, especially because intriguing effects often occur on length scales comparable with the diffraction-limit or involve coupling phenomena on this length scale. For this reason in this thesis a Scanning Near-field Optical Microscope (SNOM) represents one the most straightforward tool to combine the spectroscopic information with a resolution beyond the diffraction limit.

Near-field probing of light in complex photonic structures

The term complex dielectrics refers to dielectric structures with a refractive index variation comparable to the wavelength of light used to investigate them. Consequently, such structures strongly scatter light. Light scattering occurs due to the refractive index contrast between the scattering elements that differs from the index of the surrounding medium.

In order to realize a complex dielectric material one can assemble different scattering elements, and, in this thesis, two particular building blocks will be used: an air hole surrounded by a high-refractive index medium (in the case of two dimensional system) and a high refractive index microsphere in air (in the case of three dimensional system). Moreover, as it is shown in Figure 0.1, these elements can be differently assembled. In particular, a fully ordered assembly can be found for example, in the chapters 2, 3, while a completely disordered packing is reported in chapter 5. Of course, by gradually introducing disorder in perfect ordered structures also intermediate situation can be fund, and in the chapter 0.1 an intriguing example of this peculiar situation is discussed. Even though the same scattering elements with the same single scattering properties are used as building blocks of the materials, their cumulative behavior after assembly will depend on the way the building blocks are packed together.

In figure 0.1 the two possible packings for a collection of air cylinders in a dielectric medium and dielectric spheres in air are schematized. If the holes/spheres are periodically packed according to a crystal-like structure, then, once illuminated by light, the interference will be constructive only on certain defined directions, giving rise to Bragg refractions

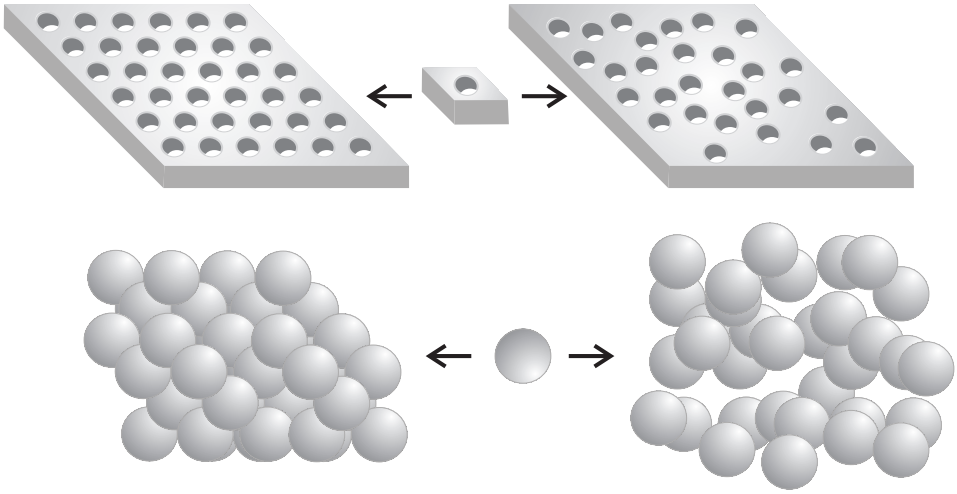

Figure 0.1: Ordered and disordered photonic structures derived from the same building block. In the two dimensional case the building block is a air cylinder embedded in a dielectric medium, for the three dimensional case is an high refractive index sphere in air.

and reflections. These particular structures are usually called Photonic Crystals. While in the disordered case the light waves will perform a random walk from one hole/sphere to the other. In this configuration the interference effects become more complicates but they however turn out to be peculiar in such structures.

In order to study these material an high spatial resolution technique is necessary. Near-field Optical Microscopy offers a resolution that is smaller with respect the dimension of the building blocks that constitute the studied material and moreover permits to combine this spectroscopic information to the morphology of the sample.

Outline of this thesis

In this thesis different photonic crystal structures will be analyzed by using a SNOM: from photonic crystal structures to completely random samples passing the intermediated situations where the role of structural disorder in perfect periodic structures where transport of light goes beyond the standard description in terms of Bloch Waves. The work is organized as follows:

- **Chapter 1** is a syntectic introduction of the main concepts that are necessary to understand the thesis. In the first part of the chapter a brief introduction of photonic

crystal and multiple scattering of light will be proposed, while in the second part some basic concept on near-field microscopy will be provided.

- **Chapter 2** proposes two new methods to spectrally tune the resonances of two dimensional photonic crystal nano-cavities via the introduction of an illuminating sub-wavelength size glass tip. Using a scanning near-field optical microscope the direct measurement of the density of states associated to the resonances of the nano-cavities is obtained. These results open new and intriguing prospectives in the use of this particular techniques for studying and modify photonic structures. At the end of the chapter polarization-resolved measurements of photonic crystal cavities will be shown to demonstrate that it is possible to obtain no-diffraction limited map of the electric field components.

- **Chapter 3** introduces a method to obtain re-writable photonic structures by infiltrating the pores of two dimensional photonic crystals with liquid suspensions. This method is then exploited to realize both passive and active components inside 2D photonic crystal platforms.

- **Chapter 4** investigates the properties of a three dimensional photonic crystal with a certain degree of disorder. By studying this system with a phase-sensitive scanning near-field optical microscope a quantitative characterization of the light propagation inside the sample is obtained. The statistical property of the phase singularity assures that the presence of disorder in such system is not negligible.

- **Chapter 5** investigates the properties of a two dimensional random structure. By analyzing the spectral behavior of photoluminescent sources embedded in the photonic structures, Anderson localization in a two dimensional system is demonstrated.

1 Perfect ordered and completely disordered structures

In this chapter the basic concept regarding photonic crystal structures and completely random structures are introduced. An intuitive explanation of the mechanisms that regulate the behavior of light in photonic crystal is provided. The case of two and three dimensional structures will be particularly considered. In the second part of this introductive chapter the light behavior in multiple scattering regime is discussed and the limits of the diffusion equation are shown.

1.1 Photonic Crystals

Photonic crystals are materials characterized by a periodical modulation of the refractive index of the same order of magnitude of the wavelength used to investigate them [1, 2]. The perfect arrangement of the materials that constituted that structures produces, due to multiple internal reflections and refractions, interference phenomena that mould the light propagation in their inside.

Depending on the modulation, if it is along one, two or three dimensions of the space, one, two or three-dimensional photonic crystals can be created. See figure 1.1. In a 1-dimensional crystal, when the period corresponds to half of the wavelength of light in the medium, Bragg reflection [3] will occur. The incident light along the periodicity direction will be reflected back with nearly 100% efficiency.

Also in the case of two and three dimensional structures, if the refractive index contrast is big enough and the absorption is negligible, the scattering at the dielectric interface can cause the formation of frequency regions where the propagation of light is inhibited for some particular directions. These frequency regions are called Photonic Band Gaps (PBG) in analogy with respect to the electronic band gap which is responsible of the electrons behavior in semiconductors [4]. Also in the case of photonic crystal the Bloch formalism [5] can be applied due to the periodicity of the dielectric constant. Even thought the behavior of electrons in semiconductors is different with respect the light propagation in photonic crystals, from the theoretical point of view there are some analogies between photons in photonic crystals and electrons in semiconductors if one considers the periodicity induced

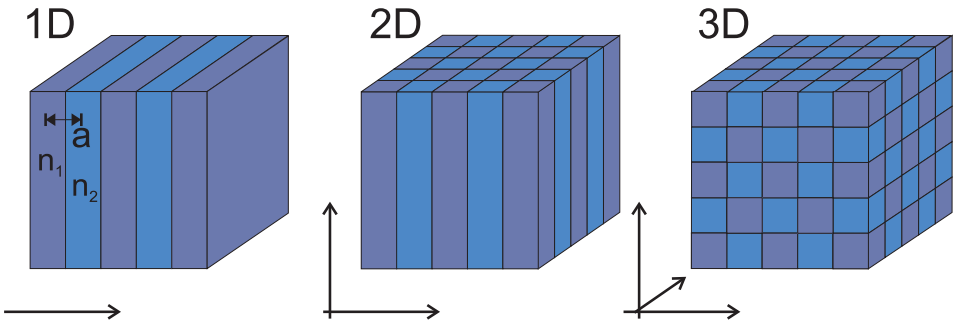

Figure 1.1: Schematic representation of three types of photonic crystals. From left to right: a multi-layer stack of materials, a periodic stacking of pillars and a cubic lattice of cubes. In the figure a define the lattice constant of the photonic crystal. The two different colors represent material with different refractive index.

by the periodical modulation of the refractive index as the periodical modulation of the electric potential due to the atomic lattice [6, 7].

For visible and near-infrared light, the lattice period of a photonic crystal must therefore be of the order of few hundred nanometers. Nowadays, due to the enormous progress in lithographic techniques, fabrication resolutions down to tens of nanometers are attainable, allowing the manufacturing of photonic crystals with very high quality [8].

By introducing a defect in the periodicity it is possible to obtain a state inside PBG region. The light associated to this state is spatially confined in correspondence of the defect due to PBG effect, consequently the defect can be exploited for example as a nano-cavity. By engineering the property of the defect one can modify the behavior of the cavity. The typical modal volume of such cavities (V) can be of the order of a cubic wavelength. Consequently when the cavity quality factor $Q = \omega/\Delta\omega$ becomes sufficiently large, the emission coupled to the cavity mode can be significantly enhanced by a factor of $Q\lambda^3/V$ through the Purcell effect [9]. The ability to modify how and if light can propagate through a material leads to a way to control how embedded sources can emit light. Modifying emission using photonic crystals has already been demonstrated to enhance or reduce emission rates [10, 11, 12, 13, 14] and can drastically improve efficiency of light emitting diodes [12, 15]

These considerations directly explain the importance of photonic crystals: by engineering their band diagram and consequently the Density Of State (DOS) one can manipulate light in their insight.

Bloch waves and Density of States

In order to better understand the reasons why photonic crystals can mold the flow of light, it is convenient to introduce the concept of DOS and to describe the propagation of light through the easiest example: a one-dimensional photonic crystal [16].

Due to the discrete translational symmetry, the propagation of light is governed by Bloch theorem [4], which states that the amplitude of the light propagating in such materials must conform to the imposed periodicity,

$$\Psi_k(y) = u_k(y)\exp(iky), \tag{1.1}$$

where $u_k(y) = u_k(y+a)$. The Bloch wave $\Psi_k(y)$, with a wavevector k, has a periodic amplitude modulation in space $u_k(y)$, which coincides with the lattice period a. In order to satisfy the equation 1.1 any Bloch wave can be written as:

$$\Psi_k(y) = \Sigma_m a_m \exp(i(k + m\frac{2\pi}{a})y), \tag{1.2}$$

where $m \in \mathbb{Z}$. These plane waves, indexed with m, are called Bloch harmonics. The wavevector of each harmonic is spaced one reciprocal lattice vector ($2\pi/a$) apart. The Bloch wave generally has one dominant harmonic called fundamental. The additional harmonics introduce a spatial beating which coincides with the periodic lattice. This spatial beating is of course the amplitude modulation $u_k(y)$ in equation 1.1.

The optical properties of a material are described by the dispersion relation, which relates wavevector and optical frequency of a wave. The dispersion relation of the first few Bloch modes is schematically depicted in figures 1.2. In particular, figure 1.2(a) shows the dispersion relation of a homogeneous medium (with a refractive index n), without any modulation of the refractive index. In this case the relation between the frequency ν and the wavelength λ of light is simply given by

$$v = \lambda\nu \tag{1.3}$$

where v is the phase velocity $v = c/n$ (c is the speed of light). Consequently the dispersion relation is a straight curve that starts from zero and has a slope given by the phase velocity (black curve in figure 1.2(a)):

$$\omega = ck/n. \tag{1.4}$$

Note that the slope of the dispersion relation also determines the direction of propagation. Both the forward and backward propagating waves are depicted in figure 1.2. Waves in a homogenous medium can be considered a special class of Bloch waves without a spatial modulation $u_k(y)$. The harmonics (in grey) all having $m \neq 0$ in equation 1.2 have zero

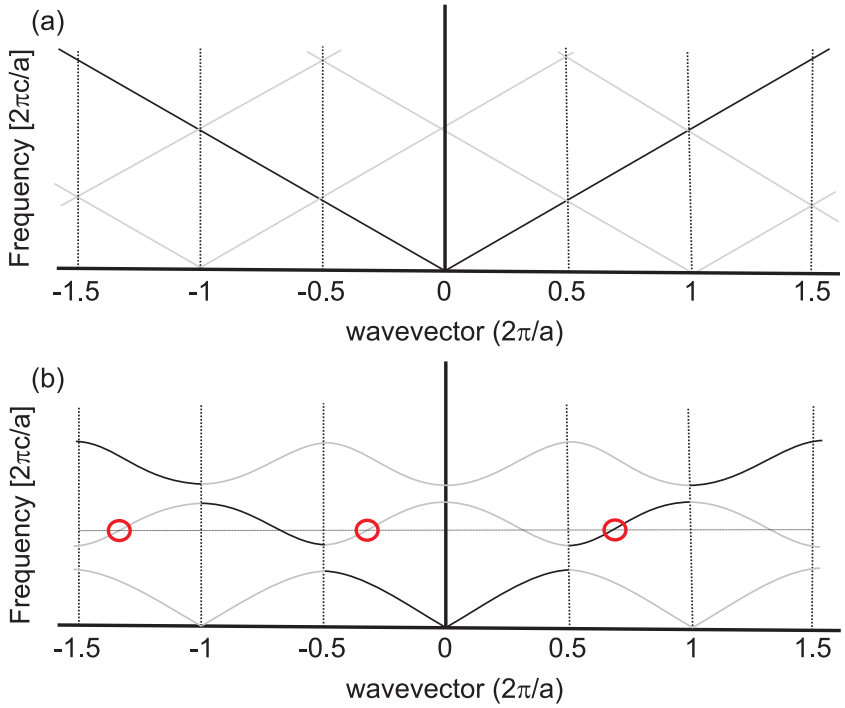

Figure 1.2: (a) Dispersion relation of a homogeneous medium indicated by the black line. The Bloch harmonics of a superimposed artificial periodicity (homogeneous medium) are indicated by the grey lines. (b) In case there is a periodic modulation of the refractive index, avoided crossings appear at the Brillouin zone edges (vertical dashed lines) and mode gaps appear.

amplitude.

When a refractive index contrast is present, the dispersion relation has avoided crossings at the edges of the Brillouin zones, resulting in the dispersion relation shown in figure 1.2(b). These edges are indicated by the vertical dotted lines. Where the avoided crossings occur, a range of optical frequencies has no modes. No states exist for these frequencies and consequently the DOS for this range of frequencies has to be zero. At the frequency indicated by the horizontal line, a photonic eigenstate is found, which means a propagating wave exists and DOS $\neq 0$. The Bloch wave excited at this frequency is composed of multiple wavevectors as is indicated by the red encircled intersections, as well as the wavevectors of the harmonics outside the plotted range. All modes allowed in a periodic medium have harmonics in all Brillouin zones, including one harmonic in the first Brillouin zone. In a one-dimensional representation, this zone is between $k = -\pi/a$ and $k = \pi/a$. A dispersion

relation in which only the wavevectors in the first irreducible Brillouin zone are described, therefore includes all the modes allowed in the structure. By unfolding the dispersion relation of the first irreducible Brillouin zone into the adjacent zones, the full dispersion relation as is depicted in figure 1.2(b)is obtained. The wavevectors in such a dispersion relation are usually depicted in normalized units of $2\pi/a$ and the frequency has normalized units of $2\pi c/a$.

3D Photonic Crystals

To completely control the light behavior using Photonic Crystals, three dimensional structures are required. The first example of a complete photonic band gap material was reported by Yablonovitch et al. in 1991 [17]. This particular structure presents a PBG in the microwaves range, in fact the lattice constant in this particular structure was $a = 1$cm. That parameter, in fact, determines the wavelength range in which destructive interference gives rise to the PBG of the photonic crystal. In order to work in the telecom and visible region one requires structures with a nanometric-scale modulation of the refractive index and consequently one requires sophisticated techniques to obtain such modulation. However, in the last two decades, also for this frequency region, a rich variety of photonic crystal structures and devices were proposed and fabricated [18, 19, 20, 21].

Also from the theoretical point of view in the last ten years several simulation methods were developed (also freely available online [22, 23]), that permit to solve Maxwell equations and to predict how an electromagnetic wave propagates through a photonic crystal and to calculate the density of states and the band diagram of these structures. An example of a band diagram and DOS for a three-dimensional photonic crystal is depicted in figure 1.3. In particular in figure 1.3(a) the band diagram is shown, where the normalized frequency is plotted in function of the k vectors of the first Brillouin zone (the symmetry points are reported, not the values of k), for an ordered structure having a FCC lattice [7, 4]. Such structure shows a complete photonic band gap around 0.8 in normalized units (that corresponds to 1.5μm if $a = 1.2\mu$m), which means that in this wavelength range the light with any k vector can not propagate inside the sample and it is necessary reflected back. In figure 1.3(b) the DOS versus the normalized frequency is shown for the same sample. The two red zones in the figure highlight the frequency region of the photonic band gap (around at $\omega a/2\pi c = 0.8$) and of the main pseudo-gap (centered $\omega a/2\pi c = 0.5$) for the band diagram and for the DOS. The pseudo-gap is a range of frequencies where the propagation of light is forbidden in the structure for only some k vectors. The DOS is zero in the photonic band gap, and very low in the pseudo gap.

Even if fabrication breakthroughs drastically improved the performances of three dimensional photonic crystals, there are still some unsolved problems in the development of such structures. The most common typologies of three dimensional photonic crystal are layer-

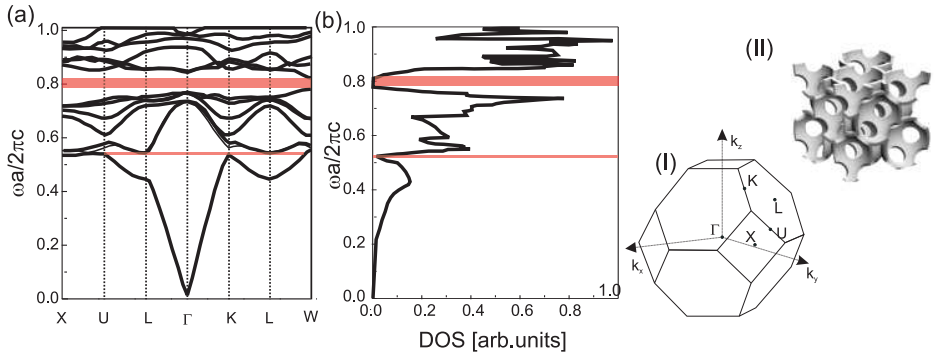

Figure 1.3: (a) Band diagram for a three-dimensional photonic crystal with an inverted FCC structure. The band gap opens around $\omega a/2\pi c = 0.8$ and a main stop band is present around $\omega a/2\pi c = 0.5$. (b) DOS of the same system presented in (a). Note that DOS = 0 in the band gap. The behavior is very different from the parabolic one in free space of equation 1.4. Inset (I) schematic representation of the Brillouin zone associated to the structures. Inset (II) schematic representation of the structure.

by-layer deposited structures and self assembly ones. The first typology is time consuming and expensive, because it consists of layer-by-layer deposition of dielectric materials. Moreover, in this technique it is difficult to grow a sufficient number of layers to obtain the full photonic gap, because the layers exhibit misalignment [24].

On the counterpart the self assembly techniques is really cheap. This method takes place owing to the aggregation of nano-particles, which, after being driven to the growing surface by gravity, relax to the minimum potential energy. The result is the creation of structures with a stochastic mixture of face-centred-cubic and hexagonal close packed ordering [25]. Also in this case it is not possible to achieve big structures, in fact, only few layers of sample can be grown without introducing a significant amount of disorder. This disorder is principally induced by the spheres surface roughness and their polydispersity. (If R is the mean radius of the spheres and the deviation for each sphere from this mean value is ΔR. $\Delta R/R$ is defined as the polydispersity).

The most common structures obtained with the self assembly technique are photonic crystal direct opals [26] and the materials that are used for opal assembly are silica and polymers, in particular polystyrene and polymethyl methacrylate [27]. However the more interesting structures are the inverse opals because they usually present larger band gap with respect to the direct case. Inverse means that instead having of spheres of dielectrics and air between the voids, one has dielectrics in the voids and air spheres. See Inset (II) in figure 1.3. Inverse structures are also relatively easy to obtain, it is necessary to infiltrate

the direct one with another dielectric material and remove the constituent of the spheres in a chemical way [18, 19].

2D Photonic Crystals on membrane: devices

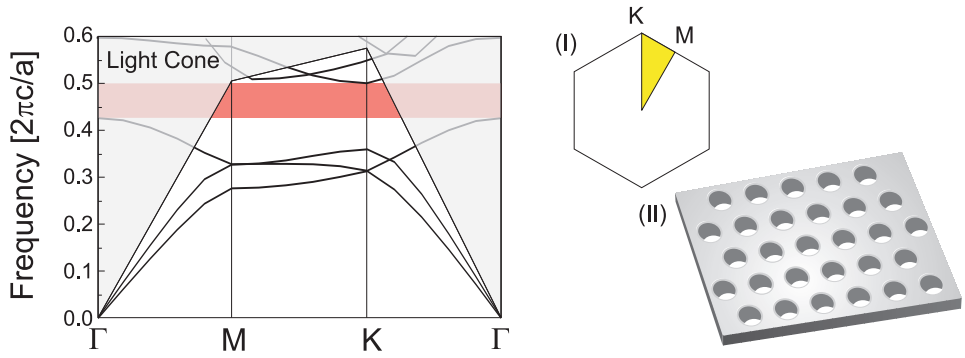

Figure 1.4: Band diagram for a two dimensional photonic crystal slab consisting of an hexagonal lattice of air pores in a Silicon core ($radius_{pore}/a = 0.48$). The band gap opens around $\omega a/2\pi c = 0.45$. Inset (I) schematic representation of the Brillouin zone associated to the structures. Inset (II) is a schematic representation of the structure.

Another alternative way to manipulate light in three dimensions using 2D structures consists in fabricating 2D-photonic crystals on a slab, as depicted in the inset of figure 1.4. These slab structures consist of a 2D photonic crystal (core) surrounded by two layers of lower effective refractive index (usually air) that provide an index guiding by total internal reflection in the direction normal to the plane of the crystal. In this way it is possible to reduce the need for a periodicity in the third dimension [10, 28].

Two dimensional photonic crystals on slab can be fabricated with a very high accuracy with e-beam or optical lithography [29, 30, 31]. The crystal slab consists of a thin film with a high refractive index, usually silicon or gallium arsenide, in which a periodic array of air holes is etched. In figure 1.4 the calculated band diagram for a thin Silicon slab with air pores ordered in a hexagonal lattice is reported. Modes above the light line (grey region) can couple with air states and are not confined in the slab. However, also in this case it exists a range of frequency where the light is confined in the slab and the propagation in the plain is inhibited due to the photonic structure.

Two dimensional photonic crystals are particularly interesting for applications since it is possible to realize defects in such structure with a high accuracy. The easiest example of

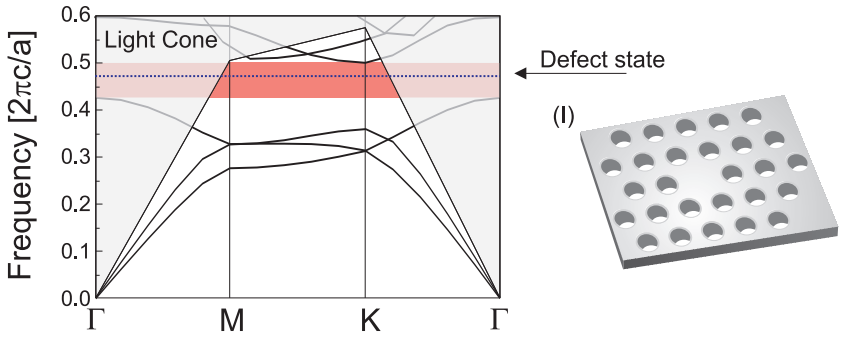

Figure 1.5: Band diagram for a two dimensional photonic crystal slab consisting of a hexagonal lattice of air pores in a Silicon core with a single defect ($radius_{pore}/a = 0.48$). The presence of the defect give rise to a state in the PBG. Inset (I), schematic representation of the structure.

a defect consists in removing one single hole in the structure presented above. The introduction of such defect give rise to a state inside the PBG region. See figure 1.5. The light associated to this state is forced to remains in the defect region, thus it is spatially confined in correspondence of the defect position and consequently the defect can be exploited as a nano-cavity.

The recent development of nano-cavities in photonic crystals has been remarkable [32]. Exploiting the cavity effects could result in very high performance light-emitting devices including low threshold nano-lasers [33] and ultra-high efficiency single-photon emitters [11]. Moreover, when the Q factor of the nano-cavity becomes high enough, the coupling condition between the nano-cavity and the light emitter changes from the so-called weak to the strong coupling regime [12], which could lead to the realization of advanced devices for quantum-information processing [13]. Combining these functionalities with passive elements, like waveguides [34], all the components for a complete photonic circuits are now available.

1.2 Random structures

As it will be discussed in detail in the chapter 4 photonic crystals, no matter how accurately prepared, contain a certain level of disorder. This disorder is due to size fluctuations of the scattering elements and other structural imperfections and it usually plays an important role in determining their optical properties, especially in the case of three dimensional structures. Disorder does not destroy interference, but it makes the optical behavior of photonic crystals much more complex. In order to understand better the light propagation in ordered system with a certain degree of disorder it is convenient to introduce some concepts about the light behavior on completely random (disordered) structures.

Disordered photonic systems are materials in which the dielectric constant varies randomly in space. Light travelling in such material is scattered by their constituent parts, all of which contribute to the scattering process. Under the effect of multiple scattering, both the amplitude and the intensity of the electromagnetic field are strongly modified. To simplify the problem of light propagation in a random media it is convenient to analyze only the propagation of the field intensity, which already provides a good description for many experimental observations.

Diffusion equation and its limits

In order to define a multiple scattering regime it is fundamental that the distance between two successive scattering events is an uncorrelated variable. The photon can be thought to travel one step after the other among scatterers and, since the step size is randomly distributed, the transport is identified as an example of random walk. A schematic picture of a photon random walk in two dimension is given in figure 1.6(a).

Each segment of the picture represents one of 10^4 steps, and corresponds to a displacement $\Delta\vec{r}$ with respect to the position of the previous scattering event. Unlike in mechanics, it is not possible to make deterministic prediction, for example to tell the position of the object performing a random walk, at a given time. A probabilistic outlook is more suitable [35]. The value of the displacement is probabilistic, and each step is a sample from a statistical ensemble. If the probability to have a scattering event is assumed constant, then the probability of a photon to travel undisturbed over the distance Δx , before it is scattered again is exponential. By defining l_s (scattering mean free path)as the average distance of free propagation, one obtains:

$$P(\Delta x) \sim \exp(-\Delta x / l_s). \tag{1.5}$$

In the particular case of uncorrelated low-density scatterers, l_s depends only on the in-

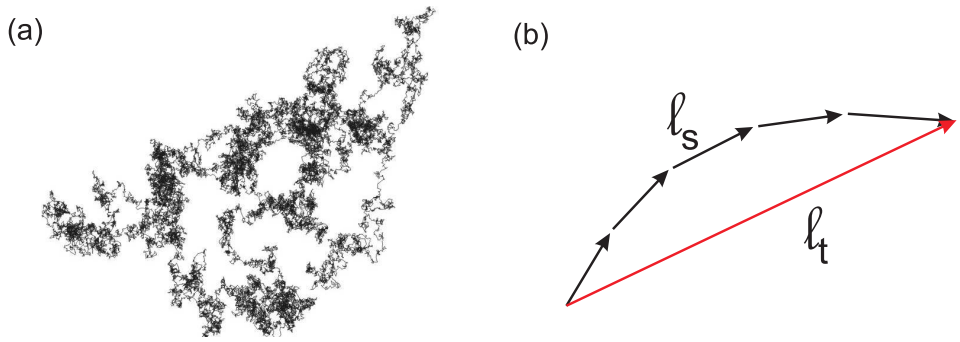

Figure 1.6: (a) Simulation of the random walk of a photon moving in two dimensions. (b) Schematic representation of the transport mean free path l_t may be substantially longer than the scattering mean free path l_s. (The images are a courtesy of Jacopo Bertolotti).

verse product of the scatterer density n and the scattering cross section σ:

$$l_s = \frac{1}{n\sigma} \tag{1.6}$$

If the scattering cross section is not isotropic, another length scale is often defined, the transport mean free path l_t, which formally defined as:

$$l_t = \frac{l_s}{(1 - < \cos\theta >)} \tag{1.7}$$

where $< \cos\theta >$ is the average cosine of the scattering angle, deriving from the differential cross section. See figure 1.6(b). The transport mean free path constitutes the length over which light looses memory of its initial direction of propagation. After a distance comparable with l_t, the scattering events are completely independent and the random walk is random also in the direction of propagation.

The exponential probability distribution of the step size (in equation 1.5) is suggested by Lambert-Beer's law, which describes the intensity of a coherent light beam, transmitted through an opaque, homogeneous, non absorbing medium of thickness L:

$$I(L) = I(0)\exp(-L/l_s) \tag{1.8}$$

In fact, the coherent beam after a length L will be formed in first approximation by all those photons which have not been scattered out of the initial direction of propagation. In order to rigorously define which is the diffused light it is convenient to consider the expansion of

a cloud of photons in a multiple scattering medium. This cloud will have an average radius R, related to the average squared fluctuations in the position of a photon at a given time:

$$R \simeq \sqrt{< X(t^2) >} \tag{1.9}$$

This final position X can be written as the sum of all the displacements δx from x_0 to X, integrated over all possible path [35]. If the observation time is long enough, the photons will have experienced a large number of scattering events, in average $N = t/ < \Delta t >$, where the denominator represents the average time interval between two scattering events. Being all the steps of the random walk uncorrelated, the central limit theorem applies and the variable X results to follow a normal distribution, whose variance grows linearly with time:

$$< X(t^2) > \sim 2Dt. \tag{1.10}$$

Equation 1.10 can be considered a definition for the diffusion constant D, which appears related to the dimensions of the expanding photon cloud. In fact, the distribution of X can be interpreted also as a transition probability, that is to say the probability for a photon to be found in X, coming from the position x_0 at t_0. This probability, associated to the process of random walk, must satisfy a diffusion equation which expresses the trend of the system toward uniformity.

Equivalently, a diffusion equation can be written for the particle (photon) density, or for the energy density of the electromagnetic field (W), which is what will be used in the following derivation. Since the propagation on length scale larger than l_t is random, there will be a net flow of light only in presence of a non uniform energy density. Otherwise all microscopic propagation cancels. The continuity equation, expression of energy conservation, tells that:

$$\frac{\delta W}{\delta t} + \nabla \overrightarrow{J} = S, \tag{1.11}$$

where W is the energy density, $\overrightarrow{J}$ the net flow of light into a unity volume and S is the source of the diffusing light. Since the energy flow is driven by the density variation, its simplest dependence is given by Fick's law:

$$\overrightarrow{J} = -D\nabla W, \tag{1.12}$$

D is the diffusion constant, measured in m^2/s and is related to the parameters of the microscopic transport by the following equation:

$$D = \frac{1}{3} v l_t \tag{1.13}$$

where v is the energy velocity of energy transport. By combining equation 1.11 and 1.12

one obtains the diffusion equation:

$$\frac{\delta W}{\delta t} = D\nabla^2 W + S. \tag{1.14}$$

This equation is extremely general, being associated with the process of Brownian motion, which describes, one for all, the thermal motion of molecules. Being an equation of second order derivatives, the solution of the diffusion equation requires the specification of the boundary conditions, besides some hypothesis on the source term. For an incident plane wave of intensity I_0, the coherent beam, formed by the wave scattered in the forward direction, acts as the source of diffused light. This source term will undergo extinction due to scattering, which is described by Lambert-Beer law:

$$S(r) = \frac{I_o}{l_s}\exp(-z/l_s). \tag{1.15}$$

where z is the depth in the sample. Appropriate boundary conditions for a finite size medium essentially require that the diffused intensity extrapolates to zero at a certain distance z_ϵ from the surface. This parameter is called the extrapolation length and takes into account the angle averaged reflection coefficient of the diffused light at the surfaces (R^D). The latter plays a fundamental role, determining intuitively the magnitude of an additional source term of diffused photons eventually diffused back and reflected onwards. z_ϵ depends also on the mean free path, following the equation:

$$z_\epsilon = \frac{2}{3}\left(\frac{1+R^D}{1-R^D}\right) l_s. \tag{1.16}$$

Interference effects

As a matter of fact, in every day life, in disordered dielectric media such as paints, milk, fog, clouds, light transport can be described by a diffusion process, as if light consisted of particles instead of waves. However, there exist simple experimental observations which cannot be explained in terms of multiple scattering of purely intensity packets, thus following the diffusion approximation.

As an example, object illuminated by coherent light (laser light) are readily observed to acquire a peculiar granular appearance [36]. High intensity spots are alternated with dark zone. In particular, the bright spots result from the constructive interference of many scattered waves, while at the dark spots they cancel out. This is a signature of preserved phase coherence upon multiple scattering. At the bright spots many scattered waves interfere constructively while at the dark spots they cancel out. This effect is called speckle.

Figure 1.7(a) shows a typical pattern observed in the image of a uniformly white reflect-

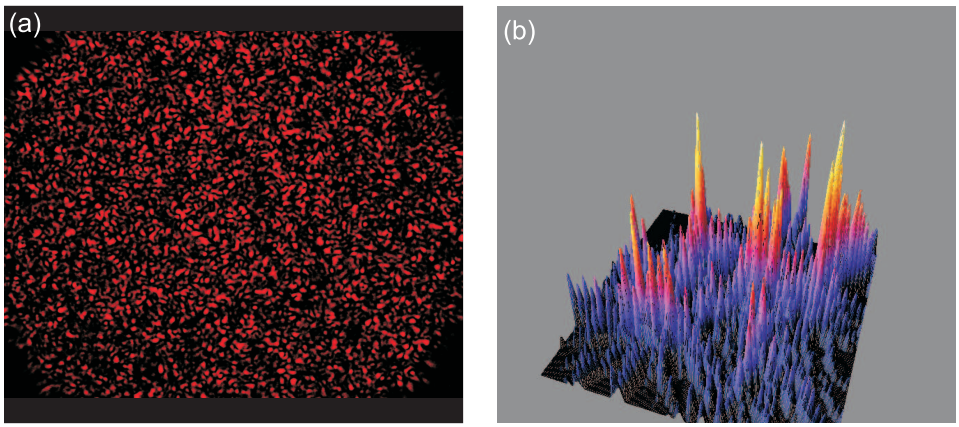

Figure 1.7: (a) Experimental speckle pattern obtained shining with a He-Ne Laser a sheet of paper. (b) Simulated speckle pattern from light incident on a disordered medium. The images are a courtesy of Riccardo Sapienza.

ing object. This image is obtained by simply illuminating with a He-Ne laser a sheet of paper and collecting the reflected signal with a camera. The extremely complex pattern bears no obvious relationship to the macroscopic properties of the illuminated object. Even if it appears chaotic and incomprehensible, this particular pattern is a fingerprint of the sample. Due to the lack of knowledge of the detailed microscopic distribution of the structure under consideration it is necessary to discuss the properties of speckle pattern in statistical terms. By analyzing the statistical properties of such pattern it is possible to gain information about the light propagation in the sample [37, 38, 39, 40]. In chapter 4 it will be show how it is possible to extrapolate from the speckle pattern the transpot mean free path, the diffusion constant and the refractive index of the sample.

Interference of light in random dielectric systems influences the transport of light in a way that is similar to the interference that occurs for electrons when they propagate in disordered conducting materials. As a result, several interference phenomena that are known to occur for electrons appear to have their counterpart in optics as well [41]. Interesting examples are universal conductance fluctuations of light [42], weak localization [43, 44], and Anderson localization [45, 46, 47]. In the case of Anderson localization the interference effects are so strong that the transport comes to a halt and the light becomes localized in randomly distributed modes inside the system.

Anderson Localization

Anderson predicted in 1958 a transition where the diffusion is halted in presence of certain random lattice [45]. Experimental evidence of this prediction was found in the following years when studying this transition in conducting materials. The electric conductivity σ decayed exponentially with the length of the system, when the Anderson localization regime is reached, and the conductor becomes an insulator, because the wave function of electrons is localized inside the sample, stopping the classic diffusion. The origin of this effect is the multiple scattering of the electrons by defects in solids. The same effect is present for photons in strongly disordered dielectrics [41], with the great advantage that no interaction is present for photons with respect to electron-electron interaction in the electronic case. This fact can make photonic systems more suitable for studying Anderson localization than electronic ones. On the contrary obtaining the same scattering efficiency with respect to electronic solids is not so easy in dielectrics. The proposal of John for photonic crystals [47] derived from the necessity to design a strongly scattering dielectric system to study Anderson localization of photons [46, 48, 49]. To obtain localization in a 3D sample, the transport mean free path l_t (the length over which the light has lost its original direction completely) is subject to the Ioffe-Regel condition [50]:

$$kl_t \leq 1 \tag{1.17}$$

where k is the wave vector.

Localization means that the diffusion mechanism of photons is stopped, and the light is trapped inside the sample. The transmission of the sample (without absorption) becomes:

$$T = T_0 exp(-L/\xi) \tag{1.18}$$

where L is the length of sample and ξ is the localization length, that represents the critical dimension for a sample to have localized states. Figure 1.8(a) shows schematically what happens to photons in the localized regime. If S is a point source inside a strongly scattering medium, subject to the Ioffe-Regel condition, two waves that propagates in opposite directions along this loop will acquire the same phase shift and so they interfere constructively. Far from the localization, loops of this type have very low probability to exist and classical diffusion dominates. In figure 1.8(b) is presented the simulated intensity pattern for a random sample in the regime of Anderson Localization. The bright region is spatially localized in a definite region of the sample and its intensity profile decreases exponentially with the distance.

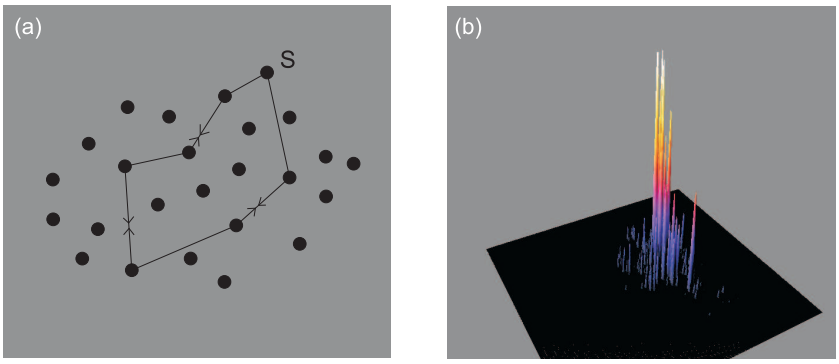

Figure 1.8: (a) Anderson localization in a 3D system is caused by constructive interference of time reversed waves if the Ioffe-Regel criterion is fulfilled. The diffusion is stopped and the light is localized in loops. (b) Simulated light intensity distribution for a random sample in the regime of Anderson localization. Light is trapped in a small regions of the medium, the localized states, which are exponentially confined.

1.3 Near-Field Optical Microscopy

Scanning near-field optical microscopy (SNOM) is at the forefront of science and technology today because it combines the potentials of scanning probe technology with the power of optical microscopy [51]. The main parameters of interest for a nano-structure under investigation are, besides shape and size, its chemical composition, molecular structure, as well as its dynamic properties. In order to investigate such properties, microscopes with high spatial resolution as well as high spectral and temporal resolving power are required. The nano-scale photonics and science, however, have an increasing need for tools that allow to characterize, generate, and manipulate structures as small as a few nanometers in size. Examples are readily found in biology [52], microelectronics, and photonics [53, 54, 55]. Electron microscopes as well as scanning tunneling and atomic force microscopes easily achieve 10 nm spatial resolution and beyond, but they are relatively poor performers with respect to spectral and dynamic properties. Electron microscopes operate in vacuum, which limits their application in life sciences, requires special sample preparation, and complicates sample manipulation. SNOM combines the excellent spectroscopic and temporal selectivity of classical optical microscopy with a lateral resolution reaching well into the sub-100 nm regime. This section is intended to give an overview of some concepts and technological requirements for scanning SNOM operation.

Beyond the diffraction Limit

At the basis of the image formation in microscopy is the interaction of light with the studied object, this interaction results in the generation of both near-field and far-field light components. The far-field light propagates through space in an unconfined manner following the principles of geometric optics. The near-field (or evanescent) light consists of a non-propagating field that exists near the surface of an object at distances of the order of the light wavelength. For a conventional optical microscope (far-field microscope), the spatial resolution is related only to the far-field component and it is thus limited by diffraction. Unless the aperture of the optical components are large enough to collect all the diffracted light, the finer aspects of the image will not correspond exactly to the object [56]. In the early 1870s, Ernst Abbe formulated a rigorous criterion that is now considered as the fundamental resolution limit for a convectional microscope: the minimum resolution (d) is expressed by the following relationship:

$$d = 0.61\frac{\lambda}{NA} \tag{1.19}$$

where λ is the vacuum wavelength and NA is the numerical aperture for the optical component. According to this equation, the best resolution achievable using conventional optical

components is about $\lambda/2$. To overcome this limit and to push the spatial resolution of optical microscopy into the $10-100$ nm regime it is necessary to collect the non-propagating component that exists only near the surface of the investigated object. Light in the near-field carries more high-frequency information and has its greatest amplitude in the region within the first few tens of nanometers of the specimen surface. Because the near-field light decays exponentially within a distance less than the wavelength of the light, it usually goes undetected. In effect, as the light propagates away from the surface into the far-field region, the highest-frequency spatial information is filtered out, and the well known diffraction-based Abbe limit on resolution is imposed.

In order to take advantage of the high spatial resolution of the evanescent waves, already at the beginning of the century, Synge and Bethe [57, 58] suggested to work with apertures characterized by dimensions smaller than the light wavelength: in the direct vicinity of the aperture, the spatial resolution is defined by the dimension of the pinhole rather than by diffraction and can thus be reduced below the diffraction limit by sufficiently decreasing the size of this aperture. Only at the end of the century (in 1984), after the invention of the scanning tunneling microscope [59], nanometer-scale positioning technology was available and an optical microscope similar to Synge proposal was realized [60, 61, 62]. The key innovation was the fabrication of a sub-wavelength optical aperture at the apex of a sharply pointed transparent probe tip that was coated with metal. In addition, a feedback loop was implemented for maintaining the tip at a constant distance (of only few nanometers) with the sample during the scanning.

To extend the spatial resolution beyond the diffraction limit several experimental configurations are common in literature [63]. Figure 1.9 shows the main operational configurations of the near-field microscope. In figure 1.9 (a) is presented the illumination configuration. In this case the probe illuminates a small area of a sample surface (reddish area under the SNOM probe) [62]. The resulting signal from the interaction with the sample is then collected in the far-field both in transmission on in reflection. This configuration can be also used to excite a photoluminescent signal of a sample in the near-field regime and then collect the luminescence in far-field. Figure 1.9 (b) shows the collection configuration. In this case far-field light illuminates the sample (or it is coupled inside it) and the near-field signal is then collected by the probe. This particular technique is commonly used for the direct detection of localized field on the sample, as it will be presented in the chapter 4 of this thesis and, as in the previous configuration, can be exploited for photoluminescence measurements. The configuration presented in figure 1.9 (c) is the illumination/collection configuration. In this case the probe is used both to illuminate and collect the near-field signal. While in the first two configurations the near-field probe consists in a metal coated optical fiber [64], in the illumination/collection case it is convenient to use uncoated probes. Since this configuration is the mainly used in this thesis, it is convenient to highlight that it allows a huge sensitivity as compared with the other two cases

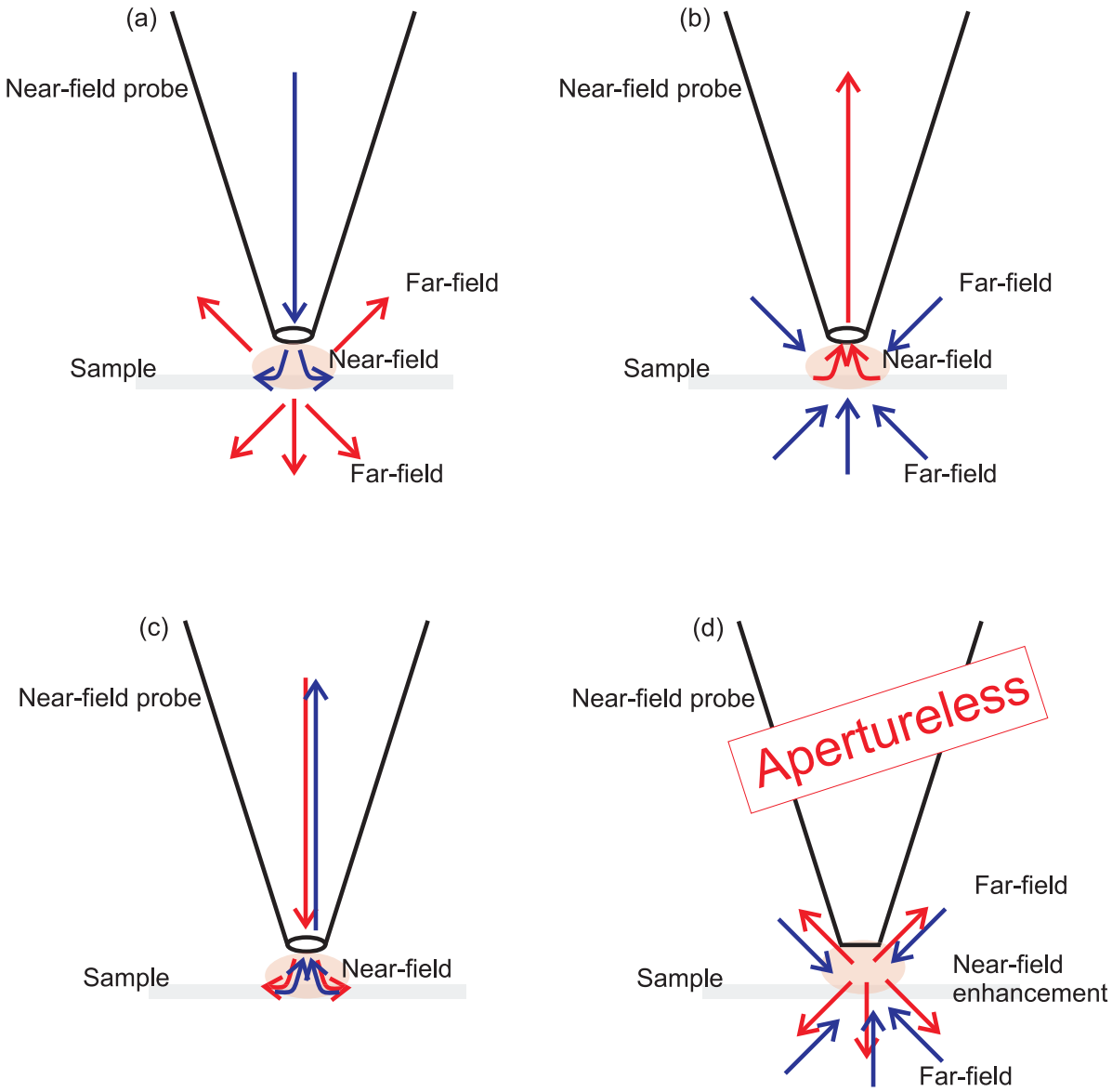

Figure 1.9: Different types of scanning near-field optical microscopes. (a)-(c) Aperture SNOM: three configuration are possible: illumination (a), collection (c) and illumination collection (c). (d) Apertureless SNOM: metal coated tips lead to field enhancement. In the images the two different colors represent excitation light (blue) and the collected light (red).

for photoluminescent experiments. The price to be payed is that the resolution, in such configuration, will be lower with respect to the case of using coated near-field probe, but is always below the diffraction limit. Nevertheless in chapter 2 it will be shown how it is possible, for some particular case, to push the resolution up to coated tip limits exploiting the effects of perturbation induced by the tip to the photonic crystal structures. Finally, figure 1.9(d) shows the apertureless techniques [65]. In this configuration a strongly confined optical field is created at the apex of a sharply pointed probe tip by external far-field illumination. The relevant near-field enhanced signal therefore often has to be extracted from a huge background of far-field scattered radiation. Resolutions ranging from $1-20$ nm have been reported in laboratory experiments. The general applicability of the technique to a wider range of samples is currently being investigated [66].

Tip-sample interaction and image formation

The mechanisms by which some components of the evanescent illuminating field can be transformed into propagating field components that carry information about the sample are at the core of image formation in SNOM. Accurate and versatile computational techniques are mandatory to understand these intricate contrast mechanisms. In general an exact calculation of the electromagnetic field is generally quite involved because of the complex geometric shape of the experimentally used near-field probes and the vector nature of the electromagnetic field. A great effort has been devoted to the theoretical understanding of image formation in near-field optical microscopy [67].

In this thesis the photoluminescence near-field maps will be simply compared with the calculated finite difference time domain (FDTD) electric field distribution associated to the structure under consideration. To that end, one can assume that the near-field map detected by the tip can be retraced by calculating the theoretical map at an effective distance from the sample surface[68]. Such distance does not represent the real height of the tip, but it is an effective free parameter that deals with the fact that the SNOM probe does not collect only the evanescent field of the structure, but in the case of uncoated tip it is also sensitive to the radiative component of the field.

Bibliography

[1] E. Yablonovitch. Inhibited spontaneous emission in solid-state physics and electronics. *Phys. Rev. Lett.*, 58:2059, 1987.

[2] S. John. Strong localization of photons in certain disordered dielectric superlattices. *Phys. Rev. Lett.*, 58:2486, 1987.

[3] M. Born and E. Wolf. *Principles of optics*. Cambridge Univ. Press, Cambridge, UK, 1996.

[4] N.W. Ashcroft and N.D. Mermin. *Solid State Physics*. Harcourt Inc., Orlando, FL, USA, 1976.

[5] C. Kittel. *Introduction to Solid State Physics (Third Edition)*. John Wiley, New York, 1968.

[6] J. D. Joannopoulos, S. G. Johnson, J. N. Winn, and R. D. Meade. *Photonic Crystals: Molding the Flow of Light (Second Edition)*. Princeton University Press, Princeton, 2008.

[7] K. Sakoda. *Optical Properties of Photonic Crystals*. Springer, Berlin, 2001.

[8] T. Asano, B. S. Song, and S. Noda. Analysis of the experimental q factors similar to one million of photonic crystal nanocavities. *Opt. Express*, 14:1996, 2006.

[9] E. M. Purcell. Spontaneous emission probabilities at radio frequencies. *Phys. Rev.*, 69:674 see 681, 1964.

[10] M. Fujita, S. Takahashi, Y. Tanaka, T. Asano, and S. Noda. Simultaneous inhibition and redistribution of spontaneous light emission in photonic crystals. *Science*, 308:1296, 2005.

[11] D. Englund, D. Fattal, E. Waks, G. Solomon, B. Zhang, T. M. Nakaoka, Y. Arakawa, Y. Yamamoto, and J. Vuckovic. Controlling the spontaneous emission rate of single quantum dots in a two-dimensional photonic crystal. *Phys. Rev. Lett.*, 95:013904, 2005.

[12] S. Strauf, K. Hennessy, M. T. Rakher, Y. S. Choi, A. Badolato, L. C. Andreani, E. L. Hu, P. M. Petroff, and D. Bouwmeester. Self-tuned quantum dot gain in photonic crystal lasers. *Phys. Rev. Lett.*, 96:127404, 2006.

[13] K. Hennessy, A. Badolato, M. Winger, D. Gerace, M. Atatüre, S. Gulde, S. Falt, E. L. Hu, and A. Imamoglu. Quantum nature of a strongly coupled single quantum dot-cavity system. *Nature*, 445:896, 2007.

[14] P. Lodahl, A. F. van Driel, I. S. Nikolaev, A. Irman, K. Overgaag adn D. Vanmaekelbergh, and W. L. Vos. Controlling the dynamics of spontaneous emission from quantum dots by photonic crystals. *Nature*, 430:654, 2004.

[15] A. A. Erchak, D. J. Ripin, S. Fan, P. Rakich, J. D. Joannopoulos, E. P. Ippen, G. S. Petrich, and L. A. Kolodziejski. Enhanced coupling to vertical radiation using a two-dimensional photonic crystal in a semiconductor light-emitting diode. *Appl. Phys. Lett.*, 78:563, 2001.

[16] P. St. J. Russell. Optics of Floquet-Bloch waves in dielectric gratings. *Appl. Phys. B*, 39:231, 1986.

[17] E. Yablonovitch, T. J. Gmitter, and K. M. Leung. Photonic band structure: The face-centered-cubic case employing nonspherical atoms. *Phys. Rev. Lett.*, 67:2295, 1991.

[18] J. E. G. J. Wijnhoven and W. L. Vos. Preparation of photonic crystals made of air spheres of titania. *Science*, 281:802, 1998.

[19] A. Blanco, E. Chomski, S. Grabtchak, M. Ibisate, S. John, S. W. Leonard, C.Lopez, F. Meseguer, H. Miguez, J. P. Mondia, G. A. Ozin, O.Toader, and O. M. van Driel. Large-scale synthesis of a silicon photonic crystal with a complete three-dimensional bandgap near 1.5 micrometers. *Nature*, 405:437, 2000.

[20] M. Campbell, D. N. Sharp, M. T. Harrison, R. G. Denning, and A. J. Turberfield. Fabrication of photonic crystals for the visible spectrum by holographic lithography. *Nature*, 404:53, 2000.

[21] C. López. Materials aspects of photonic crystals. *Adv. Materials*, 15:1679, 2003.

[22] A. Farjadpour, D. Roundy, A. Rodriguez, M. Ibanescu, P. Bermel, J. D. Joannopoulos, S. G. Johnson, and G. Burr. Improving accuracy by subpixel smoothing in fdtd. *Optics Letters*, 31:2972, 2006.

[23] S. G. Johnson and J. D. Joannopoulos. Block-iterative frequency-domain methods for Maxwell's equations in a planewave basis. *Opt. Express*, 8:173, 2001.

[24] M. J. A. de Dood, B. Gralak, A. Polman, and J. G. Fleming. Superstructure and finite-size effects in a si photonic woodpile crystal. *Phys. Rev. B*, 67:035322, 2003.

[25] R. C. Salvarezza, L. Vazquez, H. Miguez, R. Mayoral, F. C. Lopez, and Meseguer. Edward-wilkinson behavior of crystal surfaces grown by sedimentation of SiO_2 nanospheres. *Phys. Rev. Lett.*, 77:4572, 1996.

[26] P. Jiang, J. F. Bertone, K. S. Hwang, and V. L. Colvin. Single-crystal colloidal multilayers of controlled thickness. *Chem. Mater.*, 11:2132, 1999.

[27] W. L. Vos, R. Sprik, A. van Blaaderen, A. Imhof, A. Lagendijk, and G. H. Wegdam. Strong effects of photonic band structures on the diffraction of colloidal crystals. *Phys. Rev. B*, 53:16231, 1996.

[28] Y.A. Vlasov, M. O'Boyle, H.F. Hamann, and S. J. McNab. Active control of slow light on a chip with photonic crystal waveguides. *Nature*, 438:65, 2005.

[29] M. Belotti, M. Galli, D. Bajoni, L. C. Andreani, G. Guizzetti, D. Decanini, and Y. Chen. Comparison of SOI photonic crystals fabricated by both electron-beam lithography and nanoimprint lithography. *Microelectron. Engin.*, 73:405, 2004.

[30] D. Peyrade, Y. Chen, A. Talneau, M. Patrini, M. Galli, F. Marabelli, M. Agio, L. C. Andreani, E. Silberstein, and P. Lalanne. Fabrication and optical measurements of silicon on insulator photonic nanostructures. *Microelectron. Engin.*, 61:529, 2002.

[31] M. Francardi, L. Balet an A. Gerardino, C. Monat, C. Zinoni, L. H. Li, B. Alloing, N. Le Thomas, R. Houdré, and A. Fiore. Quantum dot photonic crystal nanocavities at 1300 nm for telecom-wavelength single-photon sources. *Phys. Status Solidi C*, 3:3693, 2006.

[32] S. Noda, M. Fujita, and T. Asano. Spontaneous-emission control by photonic crystals and nanocavities. *Nat. Phot.*, 1:449, 2007.

[33] S. Noda. Seeking the ultimate nanolaser. *Science*, 314:206, 2006.

[34] S.G. Johnson, P.R. Villeneuve, S.H. Fan, and J. D. Joannopoulos. Linear waveguides in photonic-crystal slabs. *Phys. Rev. B*, 62:8212, 2000.

[35] R. Kubo, M. Toda, and N. Hashitsume. *S Statistical Physics I-II*. Springer Verlag, Heidelberg, 1991.

[36] J. W. Goodman. *Statistical Optics*. John Wiley, New York, 1985.

[37] A. Z. Genack. Optical transmission in disordered media. *Phys. Rev. Lett.*, 58:2043, 1987.

[38] J. H. Li and A. Z. Genack. Correlation in laser speckle. *Phys. Rev. E*, 49:4530, 1994.

[39] P. Sebbah, R. Pnini, and A. Z. Genack. Field and intensity correlation in random media. *Phys. Rev. E*, 62:7348, 2000.

[40] A. Z. Genack, P. Sebbah, M. Stoytchev, and B. A. van Tiggelen. Statistics of wave dynamics in random media. *Phys. Rev. Lett.*, 82:715, 1999.

[41] P. Sheng. *Introduction to wave scattering, Localization and Mesoscopic phenomena*. Acedemic Press, San Diego, 1996.

[42] F. Scheffold and G. Maret. Universal conductance fluctuations of light. *Phys. Rev. Lett.*, 81:5800, 1998.

[43] M. V. Albada and A. Lagendijk. Observation of weak localization of light in a random medium. *Phys. Rev. Lett.*, 55:2692, 1985.

[44] P. Wolf and G. Maret. Weak localization and coherent backscattering of photons in disordered media. *Phys. Rev. Lett.*, 55:2696, 1985.

[45] P. W. Anderson. Absence of diffusion in certain random lattices. *Phys. Rev. Lett.*, 109:1492, 1958.

[46] D.S Wiersma, P. Bartolini, A. Lagendijk, and R. Righini. Localization of light in a disordered medium. *Nature*, 390:671, 1997.

[47] S. John. Electromagnetic absorption in a disordered medium near a photon mobility edge. *Phys. Rev. Lett.*, 53:2169, 1984.

[48] E. Abrahams, P.W. Anderson, D. C. Licciardello, and T. V. Ramakrishnan. Scaling theory of localization: Absence of quantum diffusion in two dimensions. *Phys. Rev. Lett.*, 42:673, 1979.

[49] S. Zhang, B. Hu, P. Sebbah, and A. Z. Genack. Speckle evolution of diffusive and localized waves. *Phys. Rev. Lett.*, 99:063902, 2007.

[50] A. F. Ioffe and A. R. Regel. Non-crystalline, amorphous, and liquid electronic semiconductors. *Prog. Semicond.*, 4:237, 1960.

[51] L. Novotny and B. Hecht. *Principles of Nano-Optics*. Cambridge University Press, 2006.

[52] T. H. Taminiau, R. J. Moerland, F. B. Segerink, L. Kuipers, and N. F. van Hulst. $\lambda/4$ resonance of an optical monopole antenna probed by single molecule fluorescence. *Nano Lett.*, 1:28, 2007.

[53] A. F. Koenderink, R. Wüest, B. C. Buchler, S. Richter, P. Strasser, M. Kafesaki, A. Rogache, R. B. Wehrspohn, C. M. Soukoulis, D. Ernig, F. Robin, H. Jäckel, and V. Sandoghdar. Near-field optics and control of photonic crystals. *Photonics and Nanostructures - Fundamentals and Applications*, 3:63, 2005.

[54] P. Kramper, M. Kafesaki, C. M. Soukoulis, A. Birner, F. Müller, U. Gösele, R. B. Wehrspohn, J. Mlynek, and V. Sandoghdar. Near-field visualization of light confinement in a photonic crystal microresonator. *Opt. Lett.*, 29:174, 2004.

[55] L. Lalouat, B. Cluzel, P. Velha, E. Picard, D. Peyrade, J. P. Hugonin, P. Lalanne, E. Hadji, and F. de Fornel. Near-field interactions between a subwavelength tip and a small-volume photonic-crystal nanocavity. *Phys. Rev. B*, 76:041102(R), 2007.

[56] E. Hecht. *Optics*. Addison Wesley, San Francisco, 2002.

[57] E. H. Synge. A suggested method for extending microscopic resolution into the ultra-microscopic region. *Lond. Dubl. Edien. Phil. Mag.*, 6:356, 1928.

[58] H. A. Bethe. Theory of diffraction by small holes. *Phys. Rev.*, 66:163, 1944.

[59] G. Binnig, H. Rohrer, ch. Gerber, and E. Weibel. Surface studies by scanning tunneling microscopy. *Phys. Rev. Lett.*, 49:57, 1982.

[60] D. Pohl, W. Denk, and M. Lanz. Optical stethoscopy: Image recording with resolution $\lambda/20$. *Appl. Phys. Lett.*, 44:651, 1984.

[61] A. Lewis, M. Isaacson, A. Harootunian, and A. Muray. Development of a 500 angstrom spatial resolution light microscope. *Ultramicroscopy*, 13:227, 1984.

[62] A. Harootunian, E. Betzig, M. Isaacson, and A. Lewis. Super-resolution fluorescence near-field scanning optical microscopy. *Appl. Phys. Lett.*, 49:674, 1986.

[63] B. Hecht, B. Sick, Urs. P Wild, V. Deckert, R. Zenobi, O.J. F. Martin, and D. W. Pohl. Scanning near-field optical microscopy with aperture probes: Fundamentals and applications. *Jour. Chem. Phys.*, 112:7761, 2000.

[64] J. A. Veerman, A. M. Otter, L. Kuipers, and N. F. van Hulst. High definition aperture probes for near-field optical microscopy fabricated by focused ion beam milling. *Appl. Phys. Let.*, 72:3115, 1998.

[65] U. Fischer and D. Pohl. Observation of single-particle plasmons by near-field optical microscopy. *Phys. Rev. Lett.*, 62:458, 1989.

[66] T. H. Taminiau, F. D. Stefani, F. B. Segerink, and N. F. van Hulst. Optical antennas direct single-molecule emission. *Nature Photon.*, 2:234, 2008.

[67] J.-J. Greffet and R. Carminati. Image formation in near-field optics. *Prog. Surf. Sci.*, 56:133, 1997.

[68] Y. De Wilde, F. Formanek, R. Carminati, B. Gralak, P. Lemoine, K. Joulain, J. Mulet, Y. Chen, and J. Greffet. Thermal radiation scanning tunnelling microscopy. *Nature*, 444:740, 2006.

2 Spectral Tuning of photonic crystal nano-cavities via near-field probes

In this work we observe a sizeable and reversible spectral tuning of the resonances of a two-dimensional photonic crystal nano-cavities by exploiting the introduction of a sub-wavelength size glass tip. The comparison between experimental near-field data and results of numerical calculations shows that the spectral shift induced by the tip is proportional to the local electric field intensity of the cavity mode. This observation proves that the electromagnetic local density of states in a microcavity can be directly measured by mapping the tip-induced spectral shift with a scanning near-field optical microscope. Moreover, a nonlinear control on the cavity resonance is obtained by exploiting the local heating induced by near-field laser excitation at different excitation powers. The temperature gradient due to the optical absorption results in an index of refraction gradient which modifies the dielectric surroundings of the cavity and shifts the optical modes.

2.1 Introduction

Near-field optical microscopy has already proved to be a powerful tool for studying the optical response of photonic structures and in particular two dimensional photonic crystal nano-cavities [1, 2, 3, 4, 5, 6, 7, 8, 9]. Near-field microscopy permits not only to get information about the optical properties of these structures but it also allows to locally modify their optical behavior. As predicted theoretically in reference [6] and then experimentally demonstrated in references [7, 8, 9], the local introduction of a sub-wavelength dielectric tip in the near-field of a two dimensional photonic crystal cavity induces a reversible tuning of the cavity resonance without necessarily introducing significant losses. Since the strength of the tip induced tuning is proportional to the electric field stored in the structure, by simply mapping the induced spectral shift one can obtain a high resolution map of the local density of electromagnetic states.

A larger tuning efficiency can be obtained also by exploiting the local heating induced by near-field laser excitation at different excitation powers. The temperature gradient due to

the optical absorption results in an index of refraction gradient which modifies the dielectric surroundings of the cavity shifting the optical modes.

Moreover by combining the high spectral and spatial resolution supplied by near-field microscopy with the polarization information it is possible to access not only to the intensity associated to the total electric field inside these kind of structure but also to their in-plane components with a no-diffraction limited resolution.

2.2 Interaction between photonic structure and a near-field probe tip

Central idea

The central idea in this chapter is to investigate how the presence of an external dielectric nanometer-sized object, such as a SNOM tip, can modify the resonance condition of a photonic crystal cavity. This scheme is analogous to a technique common in microwave engineering where the frequency of a resonator is adjusted by insertion of dielectric stubs [10]. In that case, because microwave resonators are typically closed, scattering from the object does not cause any loss, and the cavity quality factor Q is determined by absorption. However, when a dielectric object is placed into the field of an open cavity, such as a photonic crystal slab resonator, scattering may dominate. Indeed, it has been shown experimentally that coupling of a glass fiber tip can shift the resonance frequency of a relatively high-Q micro-resonator at the cost of reducing its quality factor [11]. Since a photonic crystal microcavity has a very small mode volume and relies on the precise arrangement of dielectric material at the sub-wavelength scale, one might expects that introducing the slightest external object would spoil the quality factor, but in the following section it will be shown that this is not necessarily the case.

Sample Description and far-field characterization

The studied sample is a two dimensional photonic crystal nano-cavity fabricated on a suspended membrane. A Gallium Arsenide (GaAs) based heterostructure is used: three layers of high-density Indium Arsenide (InAs) Quantum Dots (QDs) are grown by molecular beam epitaxy (MBE) at the center of a 320 nm thick GaAs membrane. There is a huge literature on the optical properties of QDs [12]. In this context the only relevant property of these QDs is that they provide a strong emission at 1300 nm near the resonances of the photonic structures. The membrane is grown on top of a 1500 nm thick $Al_{0.7}Ga_{0.3}As$ sacrificial layer. The fabrication process consists of patterning of a 150 nm-thick SiO_2 mask by 100 kV e-beam lithography and CHF_3 plasma etching and then transfer on the GaAs layer

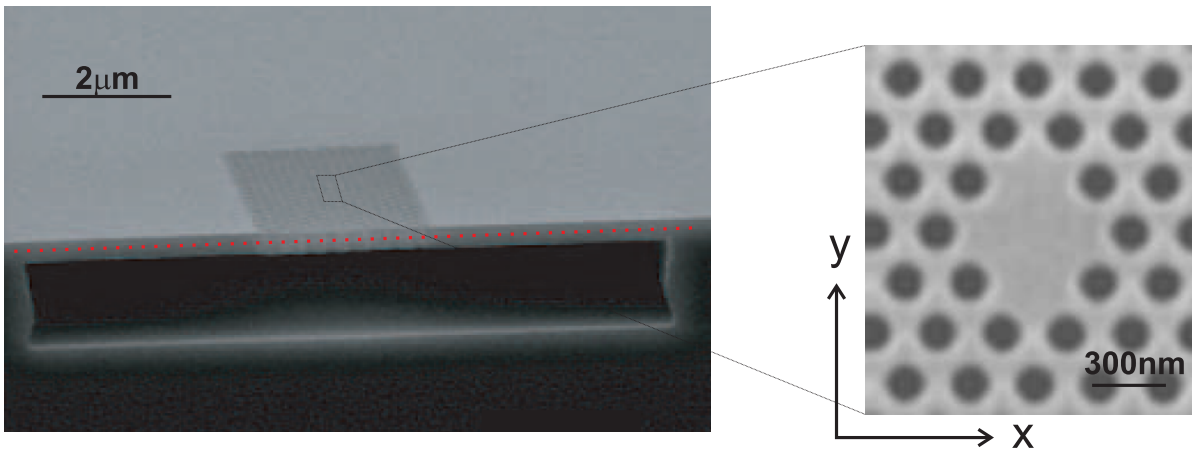

Figure 2.1: Scanning electron microscope (SEM) image of the investigated sample. In the image the GaAs suspended membrane is clearly recognizable. The red dotted line indicate the position of the three layers of $InAs$ quantum dots. In the zoom the cavity region consisting in four missing holes organized in a diamond like geometry, is reported.

by $SiCl_4$ /O_2 /Ar reactive ion etching. The membrane is then released by a selective etching of the $Al_{0.7}Ga_{0.3}As$ sacrificial layer in a Hydrofluoric acid (HF) solution. The structure under consideration consists of a two dimensional triangular lattice of air holes with lattice parameter $a = 301$ nm and filling fraction $f = 35\%$, where the cavity is formed by four missing holes organized in a diamond like geometry. It is important to notice that in this thesis, QDs are exploited only as light source easy to embed in phonic crystal structures, even if their intriguing properties are by themselves another interesting field of research [12].

A scanning electron microscope image is reported in figure 2.1. The design of the cavity is chosen in order to obtain two main resonances characterized by two different polarization states. A preliminary far-field characterization of the sample is obtained using a confocal microscope. The light of a diode laser at 780 nm is used to excite the luminescence of the QDs. In order to achieve a spatial resolution of the order of one micron a $100X$ microscopy objective ($NA = 0.7$) is used both to illuminate the sample and to collect the QDs luminescent signal. The collected light pass through a half-wave plate and a linear polarizer and then it is coupled into a single-mode optical fibre (core diameter of 5 μm) placed in the conjugate point of the focal point (acting as con-focal pinhole). The polarization-dependent spectrum of the cavity mode signal is thus measured by rotating half-wave plate.

Figure 2.2(a) provides a typical photoluminescence (PL) spectrum of the QDs embedded in the photonic structure integrating all the polarization components, while in 2.2(b) the peak intensity angular dependence with respect to direction of the axis of the polarizer is

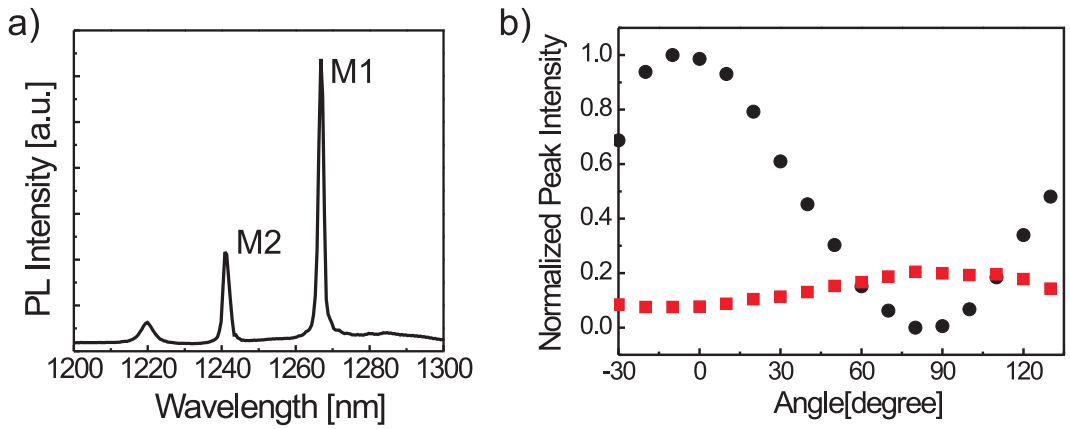

Figure 2.2: (a) Typical micro-photoluminescence spectrum collected in the far-field, the sample is maintained at $200K$ in a cold finger cryostat. (b) Polarization-dependence of the peaks associated to the modes $M1$ (black dots) and $M2$ (red squares) is measured by using linear polarizer and a rotating half-wave plate in front of the collection fiber. 0° correspond to x direction, 90° correspond to y direction

reported. As previously mentioned, the photonic structure is characterized by two main peaks, $M1$ and $M2$, centred around 1252 nm and 1228 nm, respectively. The mode $M1$ is linearly polarized (the ratio between opposite polarization is $1:100$) along the x direction, while the mode $M2$ is characterized by an elliptical polarization ($1:2$) along the y direction.

Near-field Microscope: illumination/collection geometry

All the measurements presented in this thesis (excluding the chapter 4) are obtained using a commercial Scanning Near-field microscope TwinSNOM by Omicron. The big advantage of using a commercial system is to have high stability and consequently high reproducibility in the experimental results. The SNOM system is combined with a traditional Microscope Axiotech by Zeiss and a home-built Confocal Laser Scanning Microscope not only to obtain an accurate positioning of the near-field probe but also to investigate the samples in the far-field region.

To investigate the properties of two dimensional photonic active structures is convenient to use the SNOM in illumination/collection geometry. In this configuration the light of a diode laser (780 nm) is coupled into a mono-mode optical fiber that it is directly connected with the near-field probe. This probe scans at a constant height with respect to the sample surface and excites the active material (excitation density of 10 MW/cm^2). The resulting

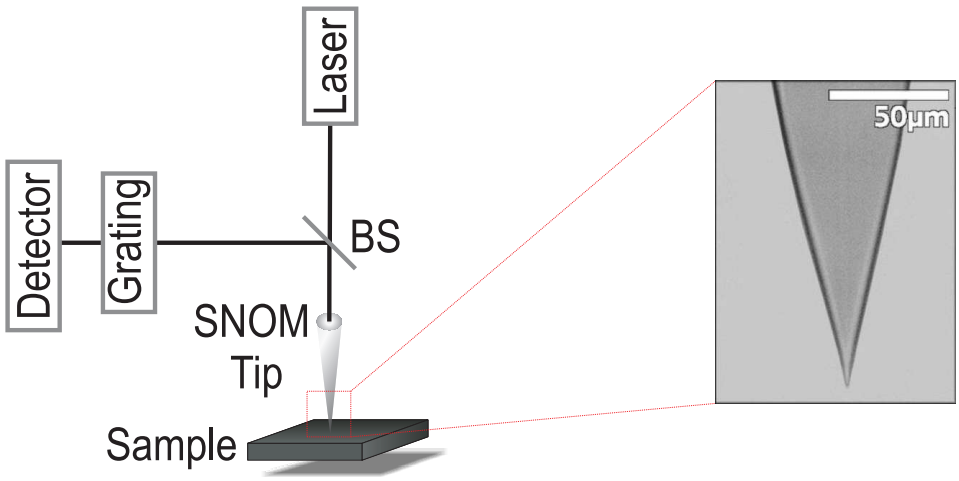

Figure 2.3: Schematic view of the setup; in illumination/collection geometry, the light from a diode laser (780 nm) is coupled into the SNOM tip and excites the sample. The photoluminescence is collected through the same tip in the same point of the excitation. The photoluminescent signal is dispersed in a monochromator, and detected with a cooled InGaAs diode array. From the recorded data, it is possible to obtain, for every frequency, the spatial distribution of the light emitted by the local source, or vice versa, for every position its local spectrum. In the zoom a SEM image of a uncoated SNOM tip is provided.

photoluminescent (PL) signal from the sample is collected at each tip position through the same probe and then dispersed by a spectrometer and detected by a cooled InGaAs array with a spectral resolution of 0.01 nm. The overall spatial resolution, obtained from the experimental is less than 100 nm, which is small enough to observe the details of the optical local DOS of the cavity and, at the same time, large enough to have a good signal to noise ratio in the PL measurements. In all the experimental results presented in this chapter chemically etched uncoated near-field fiber probes (home-built) are used [13].

Figure 2.3 provides a schematic view of the setup and a Scanning Electron Microscope (SEM) image of an uncoated SNOM probe. Moreover, even if the use of a coated tip would improve the spatial resolution, it would have dramatic consequences not only for the transmitted signal but also in the perturbation induced by the tip with consequent complications in the interpretation of the measurements.

2.2.1 Tip induced Tuning

The local introduction of a sub-wavelength dielectric SiO_2 tip can be used for accurate tuning of the resonance frequency of a photonic crystal microcavity without necessarily introducing significant losses. A simple picture for the frequency shift emerges in the weakly perturbative regime where $\frac{\Delta\omega}{\omega} \ll 1$ and the Q is not degraded. In this case the shift of the cavity mode is proportional to the electric field:

$$\frac{\Delta\omega(r_\parallel, z_{\text{tip}})}{\omega} = -\frac{\alpha_{\text{eff}}}{2V_{\text{cav}}} \frac{|E_0(r_\parallel)|^2}{max(\epsilon(r)|E_0(r_\parallel)|^2)} \exp\frac{-z_{\text{tip}}}{d}, \tag{2.1}$$

where the exponential z dependence of the electric field associate to the mode $E_0 = E_0(r_\parallel)\exp\frac{-z_{\text{tip}}}{2d}$ is separated from its dependence on the lateral tip coordinate $r_\parallel$ and it is assumed that the unperturbed field is constant over the small tip cross section [6]. In equation 2.1 d is the typical length within which the cavity mode decays, V_{cav} and α_{eff} represent the modal volume and the effectively polarizability of the tip, respectively. The tip polarizability depends on its geometrical features and on the interaction with the cavity modes. In particular, if r_{tip} and ϵ_{tip} are the radius and dielectric constant of the tip respectively then α_{eff} is given by:

$$\alpha_{\text{eff}} = 3\pi r_{tip}^2 d\frac{\epsilon_{tip}-1}{\epsilon_{tip}+2} \tag{2.2}$$

This dependence of α_{eff} from the exponential decay of the mode assures that the same tip can induce different shift on different modes, depending on d. The direct dependence of the spectral shift on the electric field E_0 can be exploited to map the electromagnetic local DOS, which is essential for the proper characterization of photonic structure. Even if SNOM experiments have proven to have enough sensitivity and spatial resolution for this purpose [1, 2, 3, 4], an unambiguous and artifact free determination of the local DOS has not been achieved so far, due to the complex interaction between SNOM tip and sample.

Near-field Measurements, discussion

The SNOM not only permits to investigate the optical property in the near-field region of the sample but also provides a high resolution topography map. In figure 2.4(a) the shear-force image of the studied cavity is presented. The opportunity of having simultaneously the information about the topography of the sample and the optical signal from the sources permits to localize the signal in determinate positions around the cavity and to access the spatial distribution of the optical modes. In (b) a typical near-field spectrum obtained during the scan is shown. Figure 2.4(c) reports three normalized PL spectra of the $M1$ resonance recorded with the tip located at three different sites of the sample along its vertical axis, as indicated in figure 2.4(a). The spectrum recorded at the apex of the microcavity

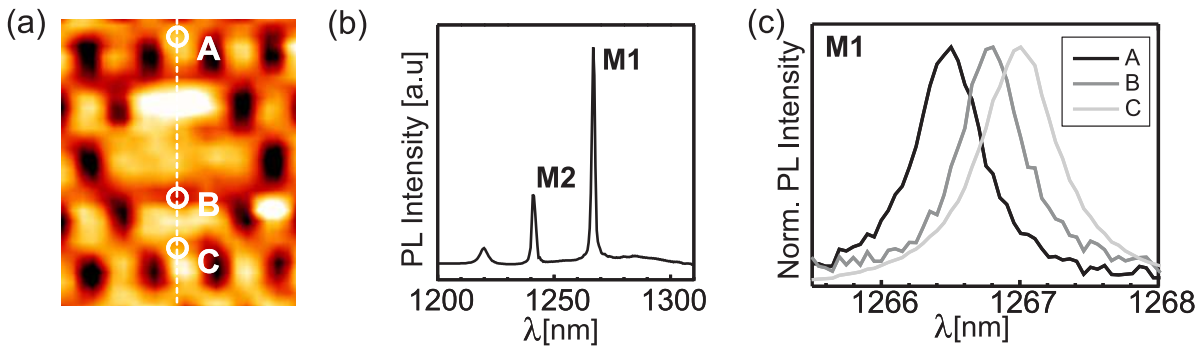

Figure 2.4: (a) Sample topography acquired concurrently with the optical data. The three white circles indicate the position of the tip where the spectra of (c) are collected. (b) Experimental near-field PL spectra. (c) Normalized Near-field PL spectra collected at three different tip positions as indicated in (a).

(position *C* in figure 2.4(a)) shows a clear red shift with respect to the spectrum recorded outside the microcavity (position *A* in figure 2.4(a)). Since the tip induced spectral shift is proportional to the electric field intensity associated to the mode, as described by equation 2.1, by mapping the spectral position of the peak it is possible to reproduce the spatial distribution of the mode.

Figures 2.5(a) and (c) report the spectral position of the peak in function of the spatial coordinate of the tip for the two cavity modes. The map, in a blue-to-white color scale, is obtained by fitting with a Lorentzian curve every emission spectrum in the wavelength range 1260 – 1275 nm, and taking, from one fits curve, the central wavelength of the cavity resonance as a function of the spatial position of the tip.

The theoretical distributions of the electric field intensity associated to the modes reported in figure 2.5(b) and (c) are performed with a commercial three dimensional finite difference time domain code (CrystalWave, Photondesign). The simulation window accurately reproduces the structure using the nominal parameters. The comparison between the experimental data in figure 2.5(a) and the numerical calculation in 2.5(b) clearly indicates that the map of the spectral shift directly corresponds to the electric field intensity associated with the resonance $M1$.

The spatial resolution, defined as the full width at half maximum of the profile of the smallest feature that can be resolved, extracted from figure 2.5 is less than 100 nm. The same analysis performed on the mode $M2$ shows analogous results. The simulated electric field reported in figure 2.5 (b) and (d) is calculated at 30 nm above the membrane, without considering the presence of the tip.

Measurements of the spectral shift form therefore an ideal method for characterizing the

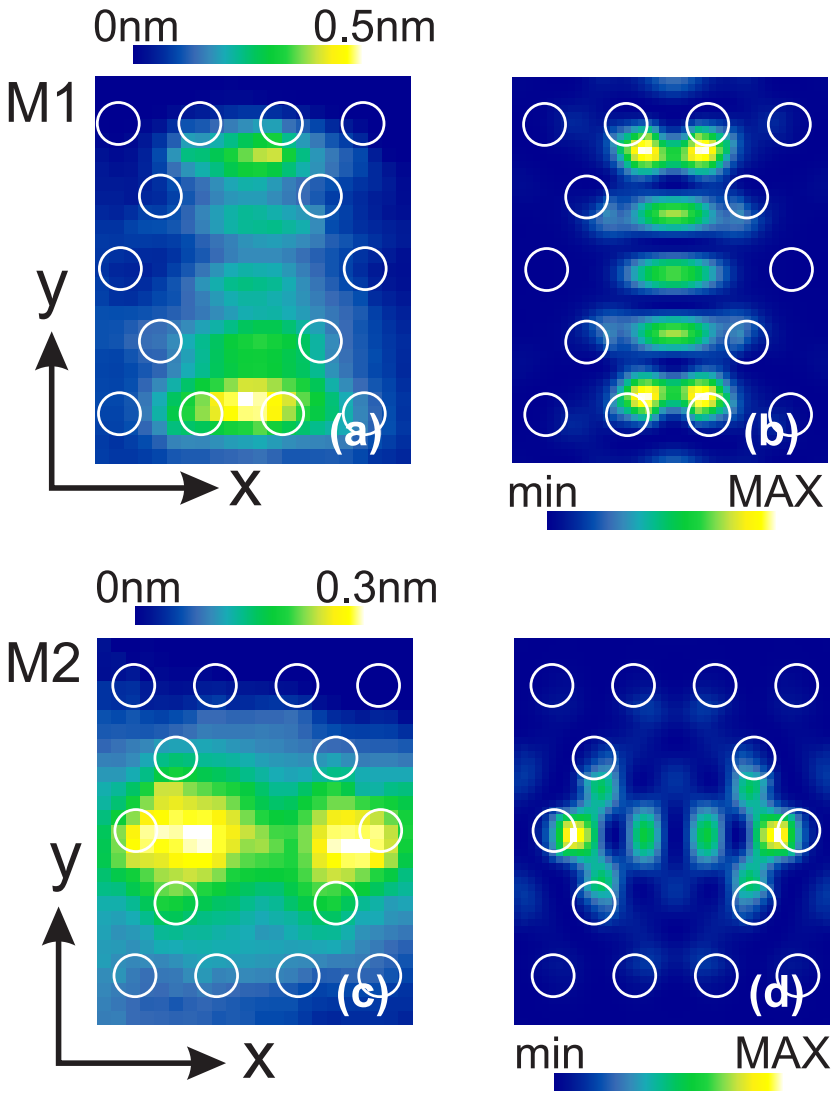

Figure 2.5: (a) Map of the tip induced spectral shift of resonance $M1$, maximum red shift of 0.5 nm. (b) Calculated FDTD spatial distribution of $|E_0|^2$ related to mode $M1$. (c) Map of the tip-induced spectral shift of resonance $M2$, maximum red shift of 0.4 nm. (d) Calculated FDTD spatial distribution of $|E_0|^2$ related to mode $M2$. The position of the photonic crystal pores is superposed to guide the eye. All the images cover an area of $1.15x1.40$ μm.

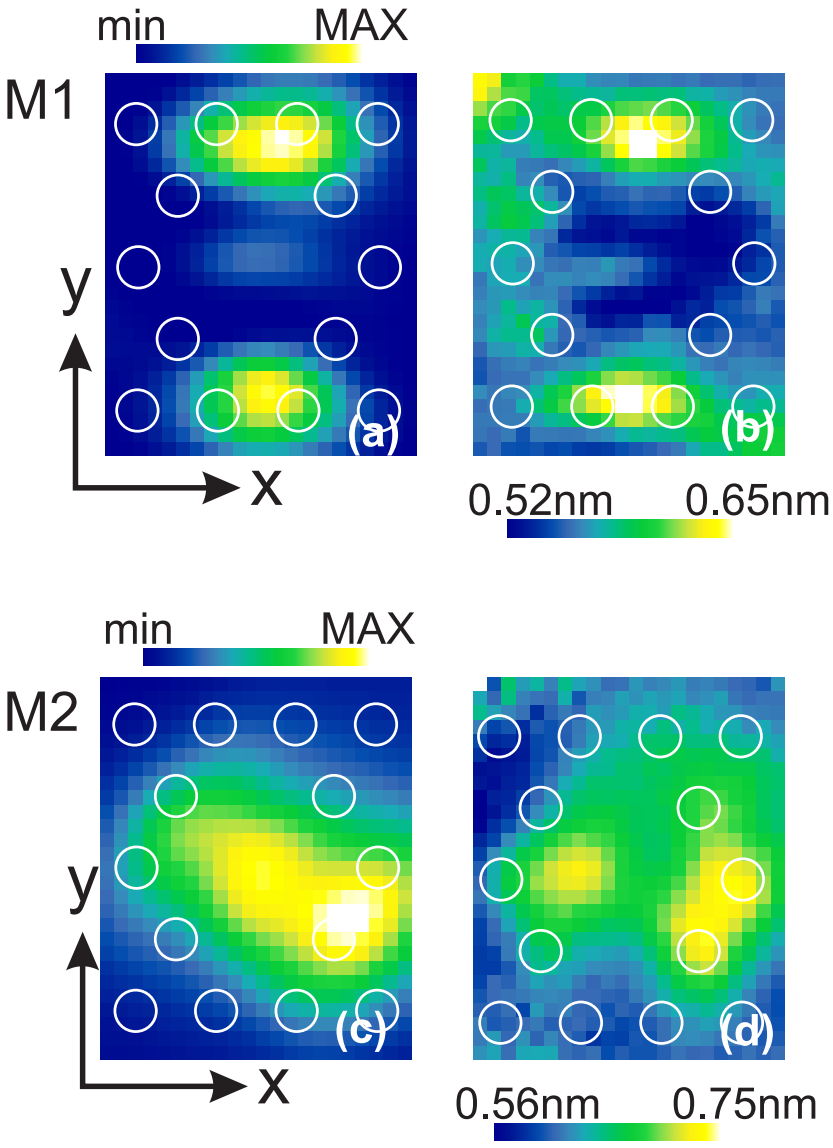

Figure 2.6: Spatial distribution of the PL signal related to resonance $M1$, integrated in the wavelength range between 1266.24 nm and 1267.2 nm. (b) Map of the spectral broadening of resonance $M1$; minimum broadening 0.52 nm and maximum broadening 0.65 nm. (c) Spatial distribution of the PL signal related to resonance $M2$, integrated in the wavelength range between 1240.2 nm and 1241.2 nm. (d) Map of the spectral broadening of resonance $M2$; minimum broadening 0.56 nm and maximum broadening 0.75 nm. The position of the photonic crystal pores is superposed to guide the eye. All the images cover an area of $1.15x1.40\ \mu m^2$.

modes of the system. In conventional SNOM experiments the PL intensity is assumed to directly correspond to the spatial distribution of the electric field intensity [1, 2, 3]. In figure 2.6(a) and (c) is reported the spatial distribution of PL intensity at the frequency of of the peak $M1$ and $M2$, respectively. In this case the maps are less detailed and a worse spatial resolution (250 nm) is obtained. The map of the spectral shift represents a cleaner measurement of the local DOS with respect to the map of the PL intensity. This is a very important result, which is related to the fact that the PL intensity collected through the tip can be affected by different parameters, as the not perfect coincidence of the physical shape of the tip and its optically active region, the eventuality that the tip collects a mixture of evanescent and propagating waves, and the possible inhomogeneity of the quantum dots. Since the strength of the tip-induced spectral shift is proportional to the electric field intensity of the eigenmode, this improved imaging method can be generalized to any microcavity design. An exciting option of the tip induced tuning is the possibility to perturb the optical mode without introducing additional losses.

Figures 2.6(b) and (d) show the map of the resonance broadening of the modes $M1$ and $M2$, respectively. The images are obtained by reporting in a blue-to-white color scale the values of the full width half maximum (FWHM) extracted by the same Lorentzian fits performed to create the maps of the spectral shift in figure 2.6. Numerical calculations [6] already clarified that, even though the losses are expected to be larger where the perturbation of the tip is larger, the relation between the spectral shift and the induced losses is non-trivial, due the fact the scattering into the tip is sensitive to the polarization of the mode at the tip position. Our experimental data show that there are positions where the tip induced tuning presents a local maximum and the spectral broadening has a local minimum, as, for instance, for the resonance $M1$ in the regions just above and below the center of the cavity. It is extremely interesting to note that the maps of the resonance broadening exhibit a close resemblance to the intensity maps: the SNOM tip induces more losses at the locations where it collects more signal.

In order to gain more quantitative understanding, figure 2.7 shows an analysis of the spectral position and FWHM of the mode $M1$. The experimental data of figure 2.7 are obtained by extracting the line profiles along the y direction in the middle of 2.5(a) and 2.5(b). The measured values are compared with the results of the FDTD calculations. The presence of the tip in the simulation is obtained by putting a dielectric cylinder, refractive index of 1.6 and diameter of 200 nm, in contact with the photonic structure.

The agreement between experiment and theory is remarkable. The behavior of the peak spectral position (circles) and of the electric field intensity (grey line) confirms that the tip-induced frequency shift follows the E^2 spatial profile. At the same time, also the FWHM of the cavity resonance (diamonds) has a well defined profile, associated to the cavity losses induced by the tip. The data reported in figure 2.7 show that the maximum tip-induced mode tuning, 0.5 nm, is as large as the resonance itself. It means that it is observed a 100%

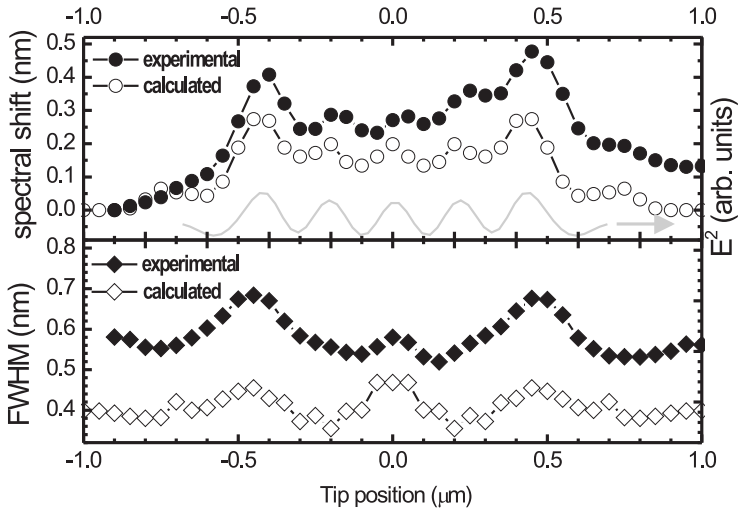

Figure 2.7: Upper panel: Experimental (filled circles) and calculated (open circles) tip-induced spectral shift of the $M1$ resonance. The grey line reports the vertical cross section, 200 nm wide, in the middle of the calculated electric field intensity reported in figure 2.7(b). Lower panel: Experimental (filled diamond) and calculated (open diamond) tip-induced spectral broadening of the M1 resonance.

tuning of the resonance peak in FWHM units and correspondingly the Q is reduced of only about 20%. More generally the spectral shift is accompanied by small changes (even negligible in specific tip positions) in the quality factor indicating that the photonic properties of the device are only slightly perturbed. In the following section it will be shown how it is possible to increase the shift effect by simply increasing the excitation density.

2.2.2 Temperature Tuning

In this section another method to control and tune photonic crystal nano-cavities is reported. By exploiting the local heating induced by near-field laser excitation at different excitation powers the dielectric environment of the photonic crystal micro-cavity is varied inducing a non-linear effect [14]. As explained in the introductive paragraph 2.1, the temperature gradient due to the optical absorption results in an index of refraction gradient which modifies the dielectric surroundings of the cavity and shifts the optical modes. This reversible tuning can be obtained either by changing the excitation power density or by exciting in different points of the microcavity.

In figure 2.8 a schematic representation of the heating mechanism is provided. In principle there are two main mechanisms for optical non-linearities in photonic crystal nanocavities under laser excitation, which can be easily identified by the sign of the mode shift. The first is related to the index of refraction modification due to free carrier generation. This has been shown to produce ultra-fast nonlinear optical tuning of photonic cavity under ps laser excitation and it gives a blue shift of the optical mode [15]. The second non-linear effect is related to the thermal tuning due to dissipation of the absorbed excitation power and it gives a shift to longer wavelengths of the cavity mode. In the data reported in the following, the mode is red shifted and, therefore, one can attribute the power dependent shift to thermal heating as expected for CW excitation. In fact, the laser pumping with a nanometric SNOM tip induces an inhomogeneous heating of the cavity, as schematically illustrated figure 2.8. Since uncoated SNOM tips are used, it is possible to neglect the effects due to the heating of the probe itself, observed in the case of a metal coated tip [16, 17] where the tip-to-sample heat transfer is, however, small [18, 19]. In this case case, the heating mechanism is due to the optical absorption in the sample and it creates a local change of the index of refraction of the sample and therefore a modification of the dielectric environment of the photonic crystal microcavity. The thermal gradient is enhanced due to the reduced heat diffusion out of the photonic crystal membrane.

In the following the results for the mode $M1$ and $M2$ of the cavity studied in the previous paragraph 2.2.1 will be discussed. Figures 2.11 report the spectra of the $M1$ and $M2$ modes detected in correspondence of the maximum (full line) and the minimum (dashed line) of the electric field intensity for different excitation densities (different color lines).

In the following analysis the denomination of spatially resonant excitation will be used for the case of pumping on the position corresponding to a maximum of local DOS and the denomination of spatially non resonant excitation will be used for the case of pumping on a point with a low local DOS. The spectrum recorded in the spatially resonant case, (i.e. in

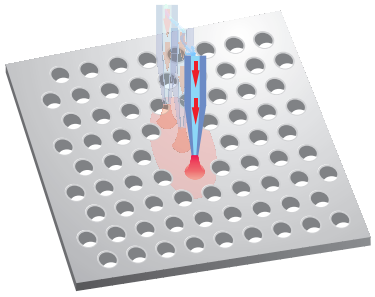

Figure 2.8: Schematic representation of the heating mechanism, the laser pumping with a nanometric SNOM tip induces an inhomogeneous heating of the cavity.

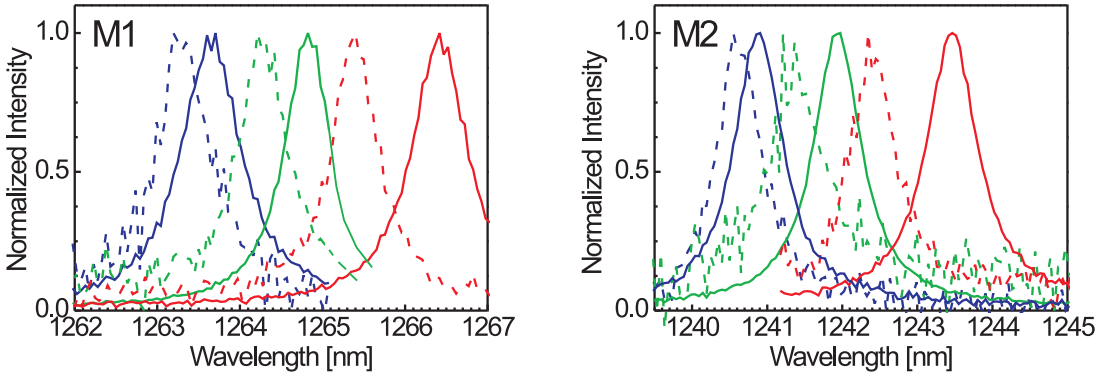

Figure 2.9: Near-field spectra obtained for different power excitation densities (5 MW/cm^2, 14 MW/cm^2 and 23 MW/cm^2 in blue, green and red, respectively) of the mode $M1$ and $M2$, respectively. The spectra reported with a straight line are collected in correspondence of a maximum of the electric field associated to the mode, while the dotted one are collected in correspondence of a minimum of the electric field. See figure 2.5(b) and (d).

correspondence of a maximum of the electric field) shows a clear red shift with respect to the spectrum recorded outside the cavity region (i.e. in the spatially non resonant case). At low excitation power this agrees with the tip induced mode shift associated to the dielectric environment modification of the cavity due to the presence of the near-field tip, already analyzed in the paragraph 2.2.1.

Figure 2.10 shows for the both modes how the map of the spectral shift is degraded as the excitation density is increased. For a low excitation power the map of the spectral shift well reproduces the profile of the electric field intensity, in fact the cavity is perturbed mainly by the effect of the presence of the SNOM tip, see figure 2.10(a) and (d). On the other hands, by increasing the excitation power the frequency shift of the mode starts to be influenced by the temperature gradient associated to the tip induced local heating, see figure 2.10(c) and (f).

In order to map the thermal gradient created in this configuration, figure 2.10(g) shows the spatial decay of the spectral shift of the cavity mode as the excitation density power is increased. For low excitation power (blue dots), the decay constant associated to the mode spectral shift is comparable with the one associated to the photoluminescence intensity (black squares). By assuming an exponential decay of the mode a decay constant of roughly (150 ± 50) nm is obtained. In this case, the heating effect could be neglected and the map of the spectral shift reproduces the map of the electric field intensity associated to the mode.

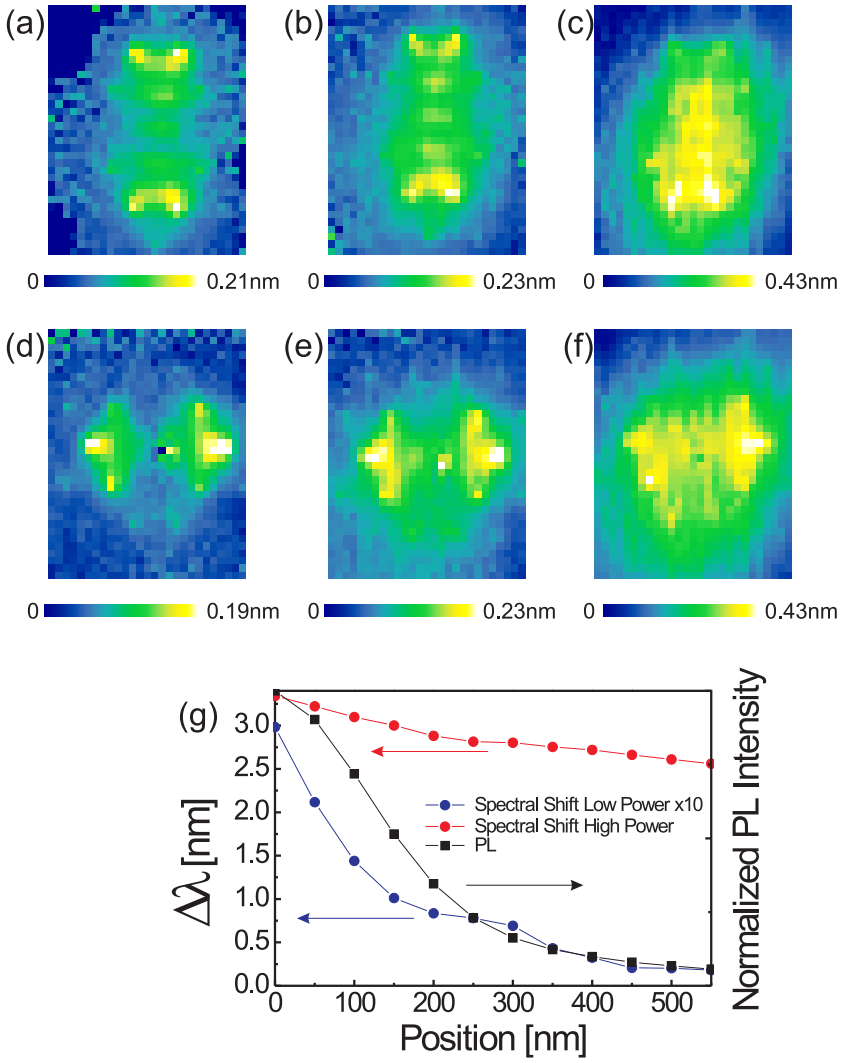

Figure 2.10: (a), (b) and (c) Maps of the tip induced spectral shift of resonance $M1$ for different excitation power: 0.3 MW/cm^2, 0.7 MW/cm^2 and 1.4 MW/cm^2. (d), (e) and (e) Maps of the tip induced spectral shift of resonance $M2$ for different excitation power: 0.3 MW/cm^2, 0.7 MW/cm^2 and 1.4 MW/cm^2.(g) Spectral shift spatial decay of the cavity mode for a excitation density power of 5 MW/cm^2 (blue dots, scaled by a factor 10) and 27 MW/cm^2 (red dots). The decay rate for the case of low excitation density power is comparable with the photoluminescence spatial decay associated to the same mode (black squares, right axis).

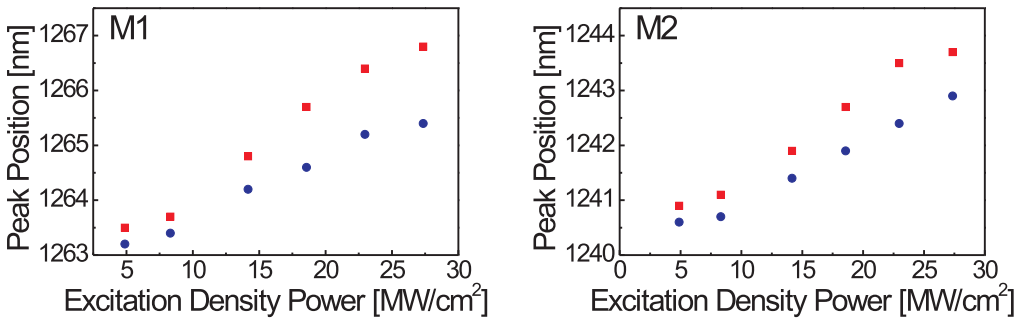

Figure 2.11: The dots in the graph represent the peak positions for the spectra presented in figure 2.9 as the excitation power is increased for the mode $M1$ and $M2$. In particular the red squares indicate the peak position of the spectra collected in correspondence of a maximum of the electric field, while the blue circles indicate the the peak position of spectra collected in correspondence of a minimum of the electric field.

For higher excitation powers, the profile of the mode shift broadens due to the thermal gradient and a reduction of the spectral shift of roughly 1 nm by moving the SNOM tip by 500 nm is obtained. This result indicates that this method allows to obtain information about the spatial distribution of the temperature averaged over the cavity mode volume.

In addition, the mode energy and the strength of the spectral shift depend on the excitation power. In figures 2.11(a) and (b) a summary of the spectral positions of the peak, for six different excitation power densities, is reported for the modes $M1$ and $M2$, respectively. Fixing the position of the tip with respect to the sample and increasing the excitation power, a monotonic shift of the cavity mode is observed. Moreover a larger non linear effect (about 1.3 nm) is observed for the spatially resonant case (for excitation density of 27 MW/cm^2).

In order to interpret in a quantitative manner the experimental results one can consider, at least in the case of spatially non resonant excitation and given to the small volume of the cavity mode, an effective average temperature and neglect the thermal gradient. The thermal tuning of the optical mode has been then quantified by performing low excitation measurements at different temperatures by heating the photonic crystal cavity with a resistor. By linearly fitting the dependence of the mode spectral position on the temperature, a thermal tuning of 0.12 nm K^{-1} is obtained. This means that the 2.1 nm maximum shift experimentally observed under non-resonant excitation would correspond to a global heating of the cavity of the order of $18K$.

From FDTD simulations, a red shift of 2.1 nm can be retrieved by a global increase of the index of refraction of $n = 0.006$ which gives a linear dependence of the index of refraction

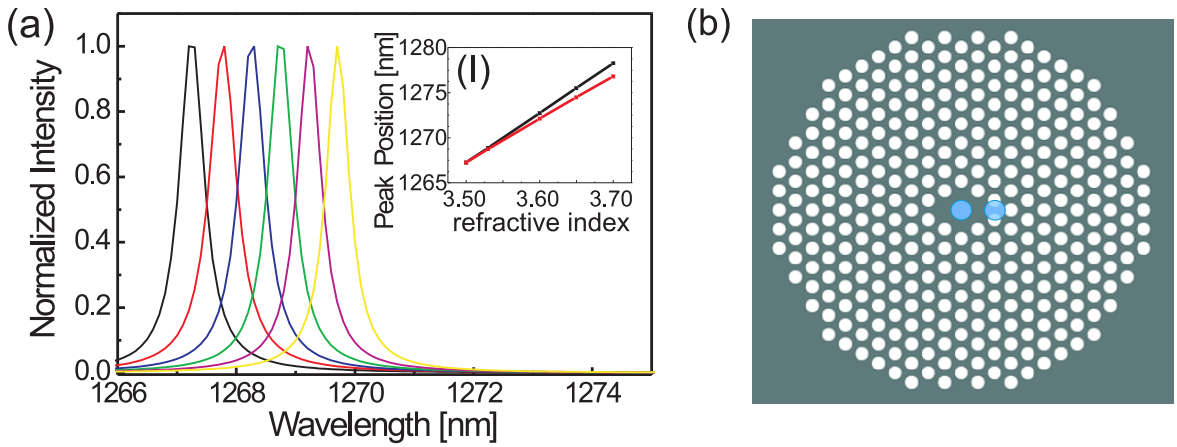

Figure 2.12: (a) Calculated FDTD spectra obtained inserting a dielectric cylinder (diameter of 300 nm) in the center of the cavity for different values of refractive index from 3.50 to 3.55 at step of 0.01. As the refractive index is increased the mode is red-shifted. The inset reports the spectral position of the mode as a function of the refractive index of the cylinder placed in the center of the cavity (red line) and on the vertical apex of the cavity as it is schematized in (b). (b) Simulated profile of the refractive index. The color gray correspond to a refractive index value of 3.5, while the color white correspond to a refractive index value of 1. The blue circles represent the two position where the dielectric cylinder is placed to simulated the tip-induced heating.

$\Delta n/\Delta T = 3.310^{-4}\ K^{-1}$ to be compared with the value of $\Delta n/\Delta T = 2.710^{-4}\ K^{-1}$ reported in the literature for GaAs in the case of vertical cavity surface type optical resonator at wavelength around 1 μm [20]. In the case of spatially resonant excitation the non-homogeneous heating of the cavity cannot be neglected.

In order to evaluate it, the limit case of an additional hot spot in correspondence of the tip position that spatially decays over a distance comparable with the SNOM resolution (300 nm) is considered. When the hot spot is created in correspondence of a maximum of local DOS of the cavity the photo-generated gradient of index of refraction strongly modifies the shape of the dielectric defect, resulting in a slightly different photonic structure. In the FDTD calculation this effect is simulated as an additional cylinder of larger index of refraction placed in different positions of the cavity. Within this crude model, it is possible to obtain a different spectral shift of the mode for different combinations of the dielectric cylinder diameter d and n.

Figure 2.12(a) reports the simulated spectra obtained by placing a dielectric cylinder with $d = 300$ nm in the center of the cavity and increasing at steps of 0.01 the values of its refractive index from 3.5 (that is the same value of refractive index of the cavity), to 3.55. The inset (I) of figure 2.12 shows the behavior of the peak position as the refractive index is increased in the case where the dielectric cylinder is placed in the center or at the vertical edge (see figure 2.12(b)) of the cavity from a value of refractive index of 3.5 to 3.75.

The peak position moves to larger wavelengths with the increase of the refractive index; the slope depends on the overlap between the spatial electric field distribution associated to mode and the position of the cylinder. In other words, if the cylinder is placed in a maximum of the electric field intensity the tuning effect is larger with respect to case where the same cylinder is placed in a position of the cavity with a lower electric field intensity associated to the mode. The theoretical results reproduce the measured spatially resonant shift if it is assumed an increase of $\Delta n = 0.03$ in the refractive index of the dielectric cylinder, corresponding to a local heating of roughly 100 K. Note that the optical shift of the mode is roughly proportional to the hot spot diameter (at least for d smaller that the mode volume); for $d = 400$ nm the local heating decreases to 75 K.

2.3 Polarization dependence of the near-field intensity map

As already introduced in the paragraph 2.2 the studied nano-cavity is characterized by two main peaks, $M1$ and $M2$, centred around 1252 nm and 1228 nm, respectively. The mode $M1$ is linearly polarized (the ratio between opposite polarization is 1 : 100) along the x direction, while the mode $M2$ is characterized by an elliptical polarization (1 : 2) along the y direction. In order to study the polarization-resolved map with the SNOM, the collected photoluminescence pass through a linear polarizer before being dispersed by the spectrometer. To control the polarization of the light inside the fibre a mechanical squeezing mechanism, that acts as a Babinet-Soleil compensator for the light that pass through the fiber, is used. Also in this configuration it is possible to map the tip induced spectral shift if one has a significant amount of signal.

Figure 2.13 provides three near-field spectra (averaged in a region of $2x2$ μm) for three different polarization configurations. In red is reported the spectrum for the polarization configuration 1, where the signal of the mode $M1$ disappears, while in black is reported the spectrum in the orthogonal configuration (configuration 2). Finally in blue the spectrum obtained for an intermediate case is provided.

Figure 2.14 shows the results of the measured tip induced spectral shift for the two main modes in two perpendicular polarization configuration (configuration 1 and 2). As expected, the spectral shift maps obtained for the two cavity modes are independent of the

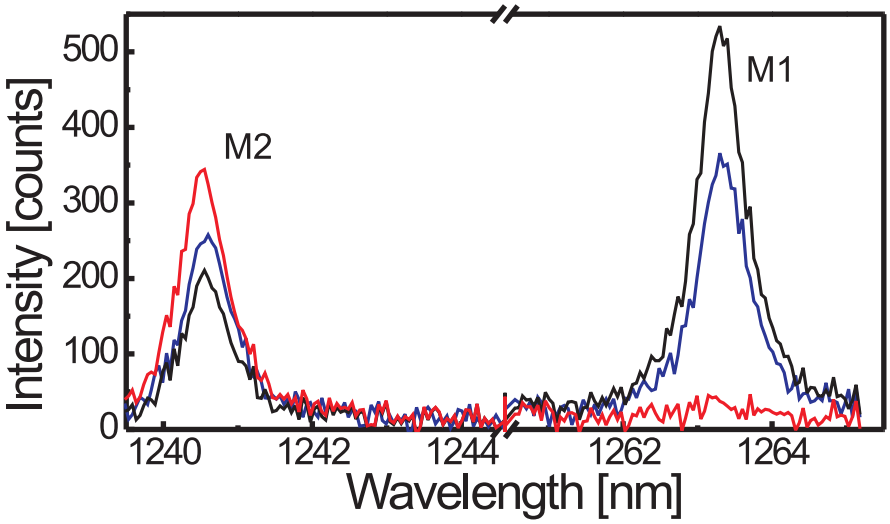

Figure 2.13: Room temperature near-field spectra of the cavity main modes (averaged on a region of $2x2$ μm) for two perpendicular polarization configurations (black and red lines) and an intermediated case(blue). In particular red line is associated to the polarization configuration 1, the black line is to polarization configuration 2. The polarization dependence of the two modes is the same both in the near and far-field measurements.

polarization configuration in the detection and, as explained in detail in the section 2.2.1, they are proportional to the electric field intensity associated to the modes. This is due to the fact that the mechanical control on the polarization does not play any role in the interaction between the near-field probe and the photonic structure.

Note that the poor quality of the map reported in figure 2.14(a) is due to the low signal in the polarization configuration 1, where the mode $M1$ is almost suppressed.

Now it is interesting to consider the PL intensity maps for different polarization detection channel. The PL map associated to the mode $M1$ it is not reported since it has prevalently only one polarization component. Figure 2.15 shows, instead, the spatial distribution of the PL signal associated to mode $M2$ for the three different polarization configurations. In particular, the image reported in figure 2.15(a) is the PL map obtained in the polarization configuration 1. In the orthogonal polarization detection channel 2, as it is shown in figure 2.15(b), the PL map is completely different. In this case the spatial distribution of the two lobes appears rotated of about 90° with respect to the previous situation. By con-

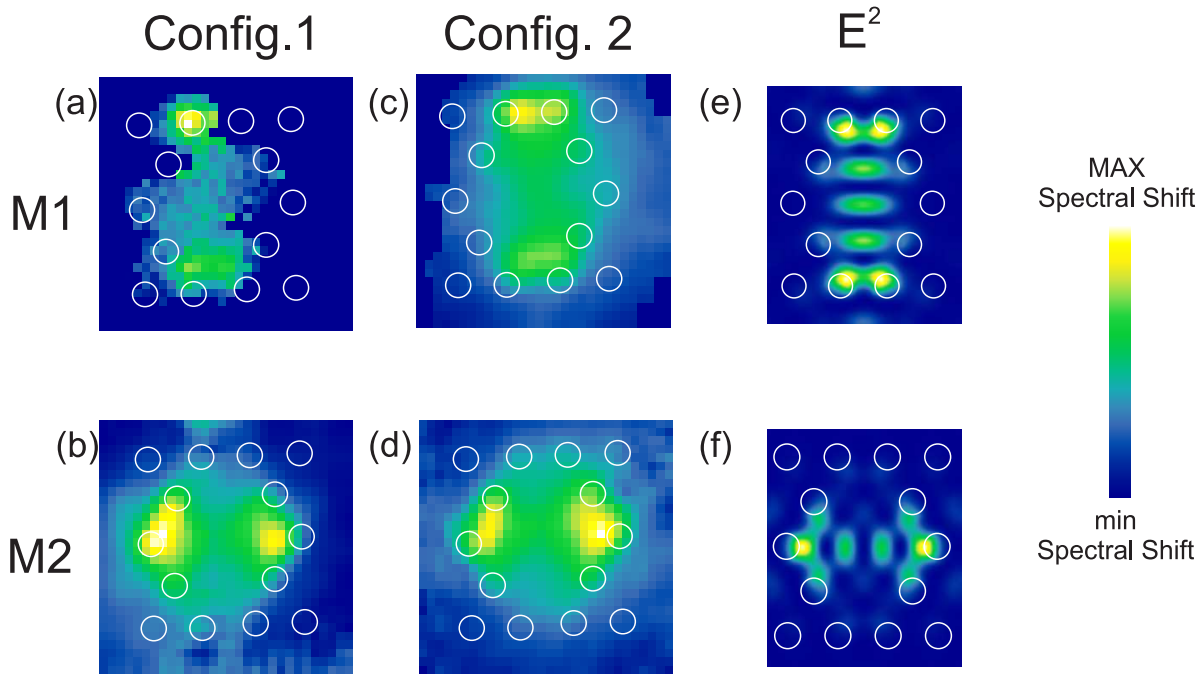

Figure 2.14: (a) and (b) spectral shift map (for polarization configuration 1) associated to the mode $M1$ and $M2$, respectively (image size $1.55x1.55\mu$ m, and maximum spectral shift 0.3 nm). (c) and (d) spectral shift map (for polarization configuration 2) associated to the mode $M1$ and $M2$, respectively (image size $1.55x1.55\mu$ m, and maximum spectral shift 0.3 nm). (e) and (f) simulated electric field map associated to the mode $M1$ and $M2$, respectively. The white circles superimposed on the images denote the topographic positions of the pores of the photonic structure.

sidering an intermediated polarization configuration, the two lobes are tilted by 45° with respect to the first case. In order to better understand these data FDTD calculations are performed. Figure 2.16 shows the total electric field intensity along the x and y axis, for different heights above the sample membrane. The distribution of the electric field in the proximity of the membrane is oriented, in the case of E_y component of the field, along the x direction; while in the case of the E_x the intensity distribution does not show a preferential orientation direction. On the counterpart increasing the distance from the membrane the two components, present perpendicular orientation directions, well reproducing the experimental data.

A good agreement between the experimental data and the FDTD calculation is obtained comparing the PL map obtained in polarization configuration 1, (reported in figure 2.15(a))

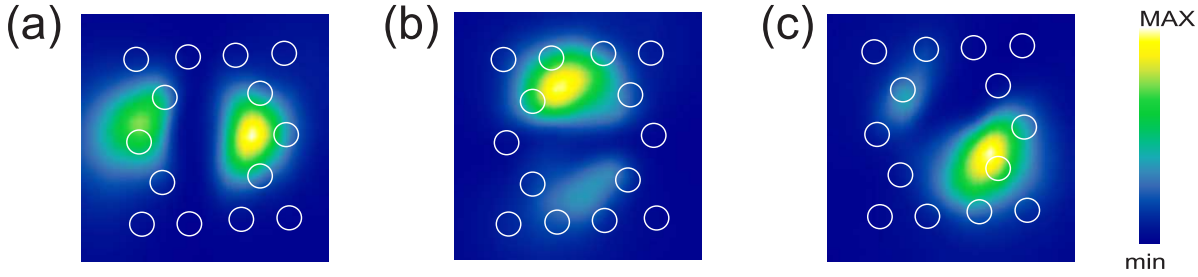

Figure 2.15: (a), (b) and (c) Spatial map of the intensity associated to the mode $M2$ for the polarization configuration 1, 2 and for an intermediated case, respectively.(images size $1.55x1.55\mu$ m).

and the calculated intensity associated to electric field component along the x axis at a distance of the 350 nm above the sample. This can be explained considering that an uncoated SNOM probes collects not only the non-radiative component of the field but also the radiative one. The exact calculation of the amount of the radiative and un-radiative component get by the near-field probe requires the knowledge of the transfer function of the SNOM tip, which depends on the tip itself and also on the emission proprieties of the cavity. To simplify this problem, one can consider that the near-field map detected by the tip can be retraced by calculating the theoretical map at an effective distance from the sample surface, that is in this case 350 nm. Thus, the distance of 350 nm above the sample surface is not the real height where the SNOM probe collects the signal but it is an effective height that permits to take into account the complex interaction between the cavity and the tip [21]. The same results are obtained by comparing the PL map in the polarization configuration 2, figure 2.15(b), with the electric field component along the y axis at a distance of the 350 nm above the sample membrane.

2.4 Conclusion

The results presented in this chapter not only open novel approaches to finely correct and dynamically tune the resonant modes of photonic crystal cavity structures, but also highlight the physic of the near-field probe interaction with the photonic environment.

The flexibility of the tuning mechanism induced by the near-field probe considered in the section 2.2.1 can be exploited for achieving the spectral overlap between resonant modes and embedded quantum dots, that is necessary for reaching the strong coupling regime. Once the right conditions are met, the reversible nature of this mechanism could permit to switch the system in and out of the strong coupling regime. Similarly, it can be used to realize photonic crystal-based switches and to modify the range of operation of photonic de-

vices, like add/drop filters or low-threshold lasers, integrated in a 2D photonic crystal slab. Moreover, this tuning mechanism can be also exploited to obtain a spatial distribution of the mode profile with an optical resolution comparable with $\lambda/13$ that is also beyond the typical resolution of SNOM.

On the other hand, the dynamic tuning of the cavity modes by resonant and non-resonant heating of the sample presented in the section 2.2.2 has the advantage of being completely reversible and also allows to continuously tune the resonance of the cavity with no substantial reduction of the Q value and no significant modification of the field distribution associated to the mode. Moreover, by combining the high spectral and spatial resolution supplied by this technique, it is possible not only to locally modify the photonic crystal cavity mode but also to exploit the mode itself as a local probe for the temperature and therefore for probing the heat conduction in photonic crystal structures.

Finally, section 2.3 demonstrates that it is possible to obtain polarization sensitive maps of photonic crystal cavity modes. In this particular configuration it is possible to access not only to the intensity associated to the total electric field inside these kind of structures but also to their in-plane components with a no-diffraction limited resolution.

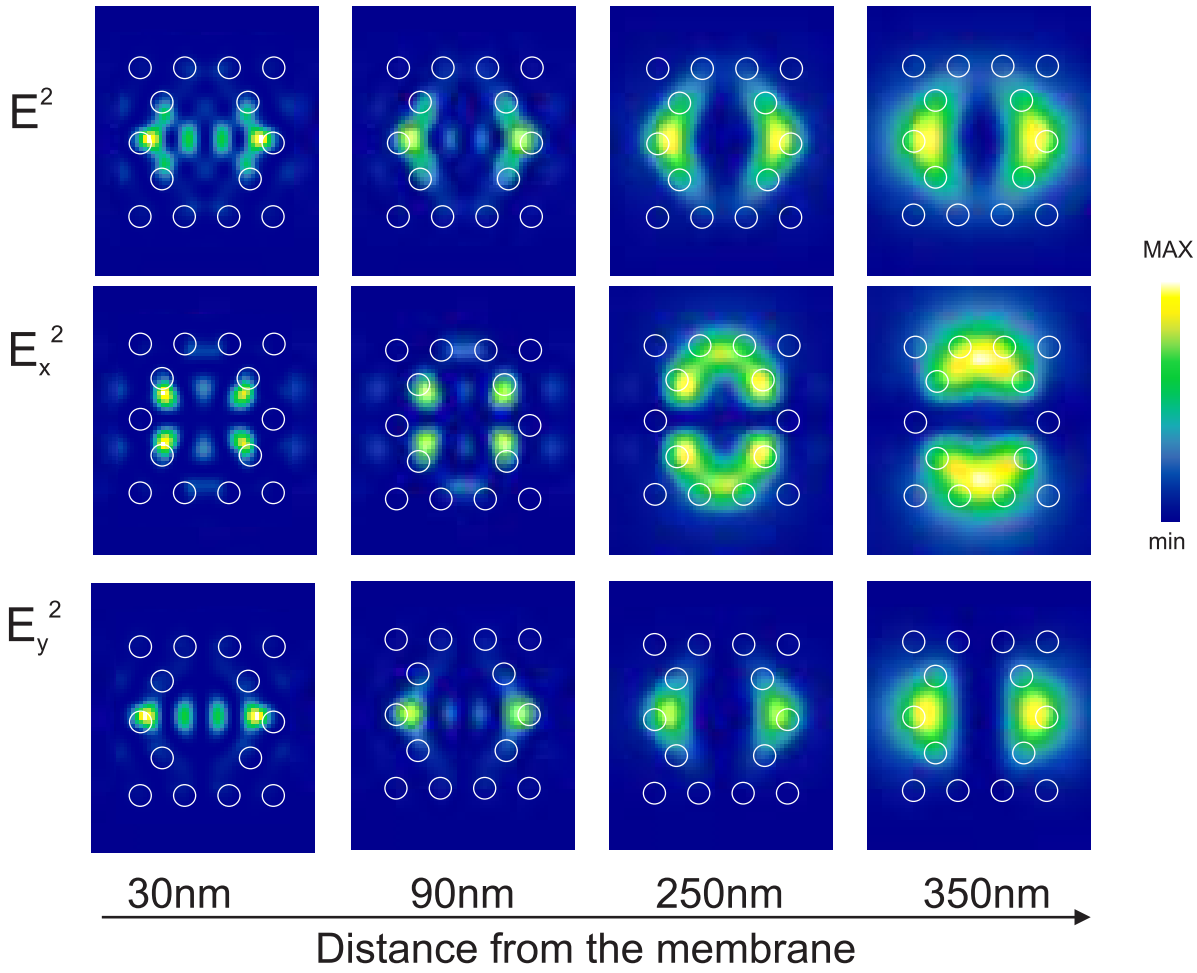

Figure 2.16: FDTD calculation of the electric field intensity E^2, and its components E_x^2 and E_x^2 associated to the mode $M2$ at a distance of 30, 90, 250 and 350 nm far away from the sample surface. The white circles superimposed on the images denote the topographic positions of the pores of the photonic structure, distance between circles 300 nm

Bibliography

[1] N. Louvion, D. Gérard, J. Mouette, F. de Fornel, C. Seassal, X. Letartre, A. Rahmani, and S. Callard. Local observation and spectroscopy of optical modes in an active photonic-crystal microcavity. *Phys. Rev. Lett.*, 94:113907, 2005.

[2] S. I. Bozhevolnyi, V. S. Volkov, J. Arentoft, A. Boltasseva, T. Sondergaard, and M. Kristensen. Direct mapping of light propagation in photonic crystal waveguides. *Opt. Commun.*, 212:51, 2001.

[3] P. Kramper, M. Kafesaki, C. M. Soukoulis, A. Birner, F. Müller, U. Gösele, R. B. Wehrspohn, J. Mlynek, and V. Sandoghdar. Near-field visualization of light confinement in a photonic crystal microresonator. *Opt. Lett.*, 29:174, 2004.

[4] H. Gersen, T. J. Karle, R. J. P. Engelen, W. Bogaerts, J. P. Korterik, N. F. van Hulst, T. F. Krauss, and L. Kuipers. Local observation and spectroscopy of optical modes in an active photonic-crystal microcavity. *Phys. Rev. Lett.*, 94:073903, 2005.

[5] A. F. Koenderink, R. Wüest, B. C. Buchler, S. Richter, P. Strasser, M. Kafesaki, A. Rogache, R. B. Wehrspohn, C. M. Soukoulis, D. Ernig, F. Robin, H. Jäckel, and V. Sandoghdar. Near-field optics and control of photonic crystals. *Photonics and Nanostructures - Fundamentals and Applications*, 3:63, 2005.

[6] A. F. Koenderink, M. Kafesaki, B. C. Buchler, and V. Sandoghdar. Controlling the resonance of a photonic crystal microcavity by a near-field probe. *Phys. Rev. Lett.*, 95:15390, 2005.

[7] S. Mujumdar, A. F. Koenderink, T. Sünner, B. C. Buchler, M. Kamp, A. Forchel, and V. Sandoghdar. Near-field imaging and frequency tuning of a high-Q photonic crystal membrane microcavity. *Opt. Express.*, 15:17214, 2007.

[8] L. Lalouat, B. Cluzel, P. Velha, E. Picard, D. Peyrade, J. P. Hugonin, P. Lalanne, E. Hadji, and F. de Fornel. Near-field interactions between a subwavelength tip and a small-volume photonic-crystal nanocavity. *Phys. Rev. B*, 76:041102(R), 2007.

[9] F. Intonti, S. Vignolini, F. Riboli, A. Vinattieri, D. S. Wiersma, M. Colocci, L. Balet, C. Monat, C. Zinoni, L. H. Li, R. Houdre, M. Francardi, A. Gerardino, A. Fiore, and

M. Gurioli. Spectral tuning and near-field imaging of photonic crystal microcavities. *Phys. Rev. B*, 78:041401(R), 2008.

[10] R. A. Waldron. Perturbation theory of resonant cavities. *Proc. Inst. Electr. Eng.*, 107C:272, 1960.

[11] S. Gotzinger, O. Benson, and V. Sandoghdar. Towards controlled coupling between a high-Q whispering-gallery mode and a single nanoparticle. *Appl. Phys. B*, 73:825, 2001.

[12] D. Bimberg, M. Grundmann, and N. N. Ledentsov. *Quantum Dot Heterostructures*. Wiley, Chichester, 1999.

[13] R. Stoeckle, C. Fokas, V. Deckert, R. Zenobi, B. Sick, B. Hecht, , and U. P. Wild. High-quality near-field optical probes by tube etching. *Appl. Phys. Lett.*, 75:160, 1999.

[14] S. Vignolini, F. Intonti, L. Balet, M. Zani, F. Riboli, A. Vinattieri, D. S. Wiersma, M. Colocci, L. H. Li, M. Francardi, A. Gerardino, A. Fiore, and M. Gurioli. Nonlinear optical tuning of photonic crystal microcavities by near-field probe. *Appl. Phys. Let.*, 93:023124, 2008.

[15] I. Fushman, E. Waks, D. Englund, N. Stoltz, P. Petroff, and J. Vukovic. Ultrafast nonlinear optical tuning of photonic crystal cavities. *Appl. Phys. Lett.*, 90:091118, 2007.

[16] A. H. La Rosa, B. I. Yakobson, and H. D. Hallen. Origins and effects of thermal processes on near-field optical probes. *Appl. Phys. Lett.*, 67:2597, 1995.

[17] M. Stähelin, M. A. Bopp, G. Tarrach, A. J. Meixner, and I. Zschokke-Gränacher. Temperature profile of fiber tips used in scanning near-field optical microscopy. *Appl. Phys. Lett.*, 68:2603, 1996.

[18] MD. Kazantsev, G. Guttroff, M. Bayer, and A. Forchel. Sample temperature measurement in a scanning near-field optical microscope. *Appl. Phys. Lett.*, 72:689, 1998.

[19] P. G. Gucciardi, S. Patanè, A. Ambrosio, and M. Allegrini. Observation of tip-to-sample heat transfer in near-field optical microscopy using metal-coated fiber probes. *Appl. Phys. Lett.*, 86:203109, 2005.

[20] J. Talghader and J. S. Smith. Thermal dependence of the refractive index of gallium arsenide and aluminum arsenide measured using semiconductor multilayer optical cavities. *Appl. Phys. Lett.*, 66:335, 1995.

[21] Y. De Wilde, F. Formanek, R. Carminati, B. Gralak, P. Lemoine, K. Joulain, J. Mulet, Y. Chen, and J. Greffet. Thermal radiation scanning tunnelling microscopy. *Nature*, 444:740, 2006.

3 Re-writable photonic circuits

In this chapter is presented a novel technique that permits to locally infiltrate the pore of two dimensional photonic crystal with liquid suspensions. In particular, a realization of a re-writable and local source inside a Si-based Photonic Crystal nano-cavity is reported. By infiltrating a solution of colloidal PbS Quantum Dots inside a single pore of the structure a Si-based nano-cavity is activated. The resulting spontaneous emission from the source is both spatially and spectrally redistributed due to the mode structure of the photonic crystal cavity. The coupling of the quantum dot emission to the cavity mode is analyzed by mapping the luminescence signal of the infiltrated solution with a Scanning Near-Field Optical Microscope at room-temperature. Spectral characterization and mode profile are in good agreement with a three dimensional numerical calculation.

3.1 Introduction

As already explained in chapter 1, a defect in an perfect photonic crystal structure can lead to localized photonic states in the gap, whose properties would depend on the shape and geometry of the defect. Based on the idea of intentionally introducing crystal defects, a broad range of potentially functional designs, such as integrated micro-cavities, channel drop filters, optical switches, and low-threshold lasers has been proposed [1, 2, 3, 4, 5]. Connecting such devices could essentially enable the photonic version of an integrated electronic circuit. Traditionally, the experimental realization of such structures is limited to simple photonic-crystal design variations, such as missing pores, pores of different sizes, or pores at different positions, all of which must be incorporated at the growth stage of the photonic crystal.

An alternative and much more flexible approach for functionalizing two dimensional photonic crystals consists of locally filling single pores of the crystal with liquids [6, 7]. If the refractive index of the filling material is sufficiently larger than 1, the filled pore behaves the same as a missing pore, except that the defect can be erased and overwritten. The infiltrated liquid can be easily removed by dipping the photonic crystal in an ultrasonic bath, opening the way to rewritable circuits and reconfigurable integrated photonic-circuit chips. Moreover, using polymer composites enables the creation of permanent structures.

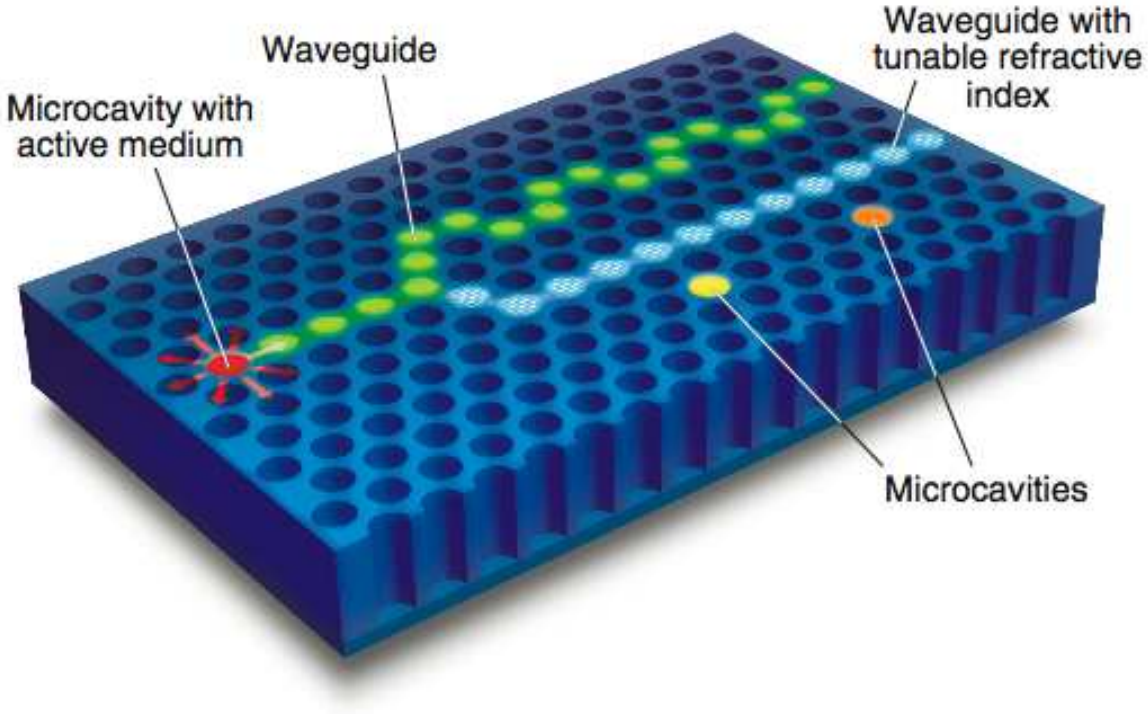

Figure 3.1: A photonic circuit can be obtained by filling the single pores of a 2D photonic crystal with liquids. Different devices can be integrated in the same sample: local light sources, bent waveguides, tunable waveguides, micro-cavities, and so on.

The ability to address a single pore also allows creation of local light sources by filling pores with active materials, such as colloidal quantum dots in solution.

An example of a rewritable circuit is provided in figure 3.1; the photons created by optically pumping the colloidal quantum dots are guided through the sample along a waveguide, obtained by infiltrating adjacent pores in a linear geometry, until they reach a Y-shaped intersection. Here, depending on the alignment of the liquid crystals infiltrated in the lower branch (blue), the photons propagate either in the S-shaped branch or in both arms. Two point-defect micro-cavities are placed along the tunable waveguide and can couple with the light flowing in the waveguide whenever the photon wavelength matches their resonances. The use of liquids with different refractive indices allows the design of cavities that couple light at different wavelengths and thus work as selective add/drop filters.

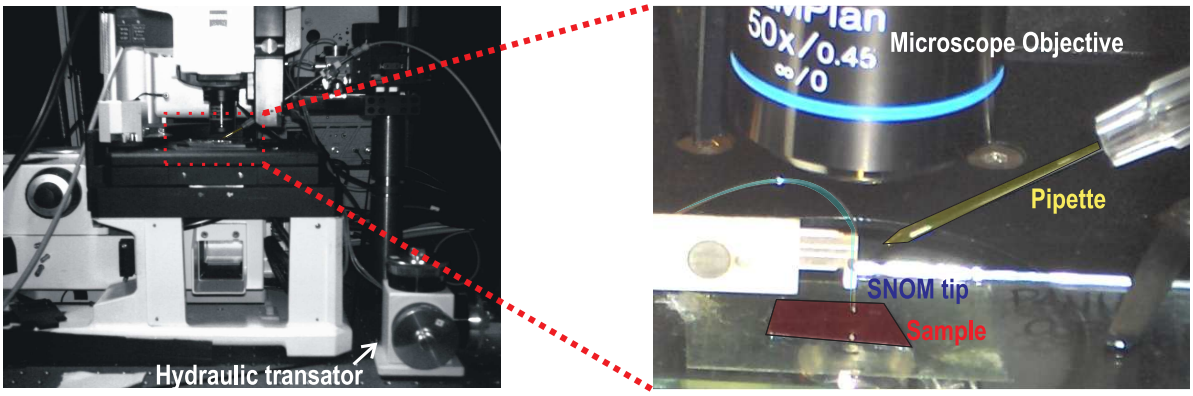

Figure 3.2: Photos of the micro-infiltration setup. In the zoom the pipette used to infiltrate the sample, the tip of the SNOM and the sample are clearly recognizable.

3.1.1 Local micro-infiltration setup

A local micro-infiltration apparatus [6] permits to perform a controlled liquid deposition inside the central pore of the cavity. The system is based on micro-infiltration technology via hollow sub-micron size pipettes. Its practical realization requires a precise control of all the elements of the experimental setup, since the typical amount of liquid inserted in the pores of the photonic structure is of the order of femtoliter or less (three orders of magnitude smaller than the liquid droplets ejected by sophisticated ink jet printers). The infiltration process is monitored by a commercial standard microscope (Zeiss, Axiotech) equipped with a custom built Confocal Laser Scanning Microscope (CLSM) and a micro-infiltration system (Eppendorf, Femtojet), developed for molecular applications, for transferring controlled amounts of liquid in cells. The micro-infiltration system consists of a micropipette with an external diameter of less than 1μm that can be moved with a precision of 0.1μm on the sample surface. Hydraulic transmissions of the pipette movements strongly reduce vibrations. The actual infiltration is performed by bringing the tip of the pipette in contact with the pore. Figure 3.2 is an image of the setup used to perform the infiltration. The optical microscope is used to monitor the approach of the pipette to the sample surface and to choose a specific pore to be infiltrated. When the pipette gets in contact with the sample a light bending of the pipette is observed. Due to the sub-micron diameter of both the pipette and the photonic crystal pores, capillary forces dominate the infiltration process. When the meniscus of the liquid inside the pipette is in contact with the selected pore, due to the capillary forces, the pore is completely filled up with the solution. Note that to trigger the infiltration it is not necessary that the pipette enters the pore, it is sufficient that the liquid inside it just touches part of the pore walls. In order to have enough spatial resolution to recognize the photonic structure an high numerical aperture (NA) objective is

required. Of course, since one has to place the micropipette above the sample surface also a high working distance (WD) is required. The good compromise is obtained by choosing a Mitutoyo Objective with $100X$ magnification and 0.7 NA, and 11 mm of WD.

3.2 Controlled Micro-infiltration for the realization of passive components

In this section the realization of passive photonic components, like wave-guide and cavities, is reported. To that end a solution of water and the organic dye Rhodamine 6G is used to infiltrate the pore of a two dimensional macroporous silicon photonic crystal [8]. The chemical and physical properties of this solution appear particularly appealing for the proposed approach: in fact, the refractive index of the aqueous solution is large enough to induce the realization of localized state inside the photonic band gap. The solution viscosity is small enough to facilitate the deposition in the sample pores, and, at the same time, is not too volatile, in order to guarantee that the photonic crystal modification lasts in time; finally, it is possible to observe if the liquid has been exactly infiltrated in the pores, by directly mapping the photoluminescence of the Rhodamine with the CLSM. This last characteristic is important since the transferred liquid volumes are very small and yet should remain detectable. Once the solution is infiltrated in the pores, it acts as local defect, while the Rhodamine allows to investigate the spatial distribution of the solution by looking at the sample with the confocal laser scanning microscope in luminescence configuration. A schematic representation of the setup is provided in figure 3.3.

The studied samples are characterized by triangular symmetry and lattice constant is 4.2 or 1.5 μm. The silicon pore walls are covered with a thin silicon oxide layer to allow the wetting of the pores. Note that the infiltration experiments are not restricted to this material and can be transferred to any other system with the appropriate wetting properties.

Figure 3.4 shows a successful controlled infiltration at single pore level of the sample with smaller lattice constant. Figure 3.4(a) is recorded with the CLSM in emission configuration exciting at λ = 488 nm, and collecting the luminescence signal of the Rhodamine solution. See figure 3.3(b). In order to block the excitation light, the CLSM is equipped with a dichroic mirror centered at 510 nm and a bandpass filter with transmission band from 520 to 560 nm that has a large overlap with the signal of the Rhodamine dissolved in water centered at 550 nm. The signal from the luminescent solution stems from the center of the image. Figure 3.4(b) is recorded in reflection configuration without changing the scanned region investigated in (a). By simply replacing the dichroic mirror with a standard 50/50 beam splitter and by removing the bandpass filter. See figure 3.3(c). Since the sample structure consists in air pores organized in triangular symmetry etched in bulk silicon, the dark regions, indicating low reflectivity, correspond to the PC pores, while the light regions,

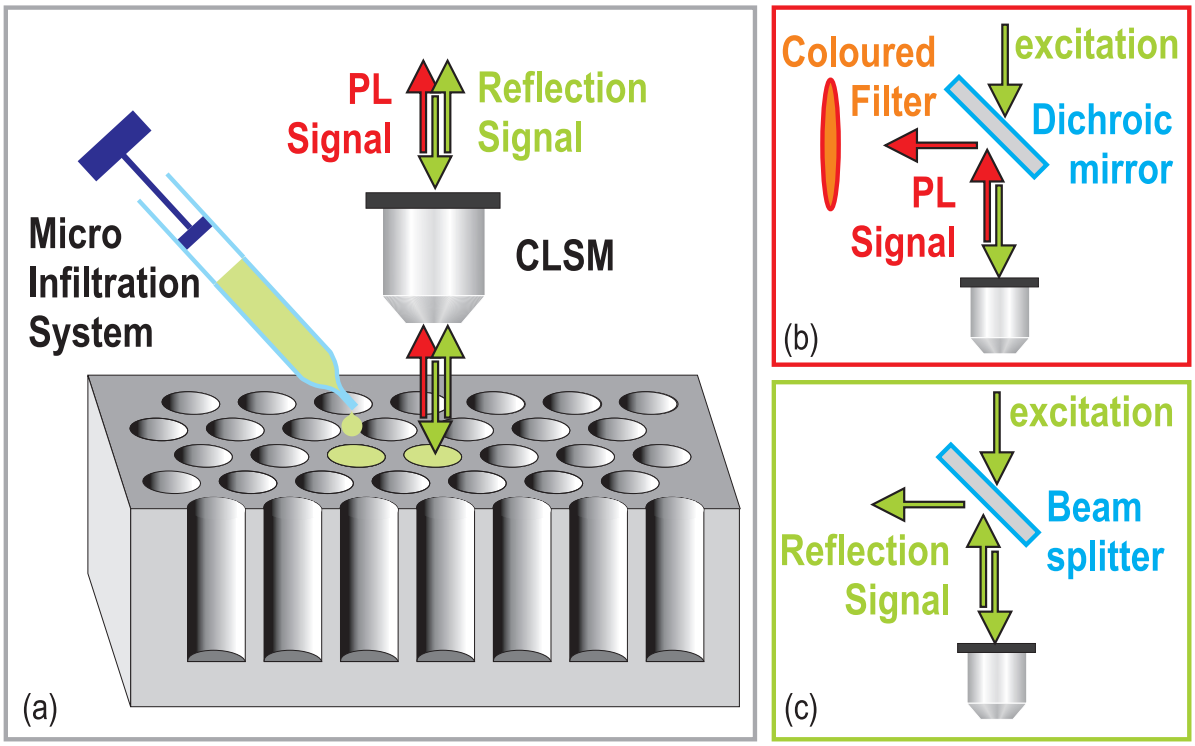

Figure 3.3: Scheme of the experimental setup. (a) The controlled infiltration task is accomplished by a micro infiltration system and monitored with a CLSM that can work both in (b) luminescence configuration and in (c) reflection configuration. The opportunity of switching between the two configurations, without changing the investigated area of the sample, is essential for the control of successful infiltration at single pore level.

indicating high reflectivity, coincide with the silicon veins between the air pores. The comparison between figures 3.4(a) and (b) confirms that the controlled infiltration is successful: the liquid has been introduced solely in the selected air pore.

The horizontal and vertical profiles along the center of the two images, reported in figures 3.4(c) and (d), respectively, highlight that the position where in the first image there is a maximum in the signal, indicating the presence of the Rhodamine solution, corresponds exactly, in the reflection image to a minimum of the signal, that coincides with the position of the air pore.

The emission properties of organic dyes depend, in general, on the solvent in which they are dissolved and, in this case of water and Rhodamine 6*G*, once the water is evaporated the peak position shifts to 570 nm and gets a pronounced tail on the long wavelength side. By

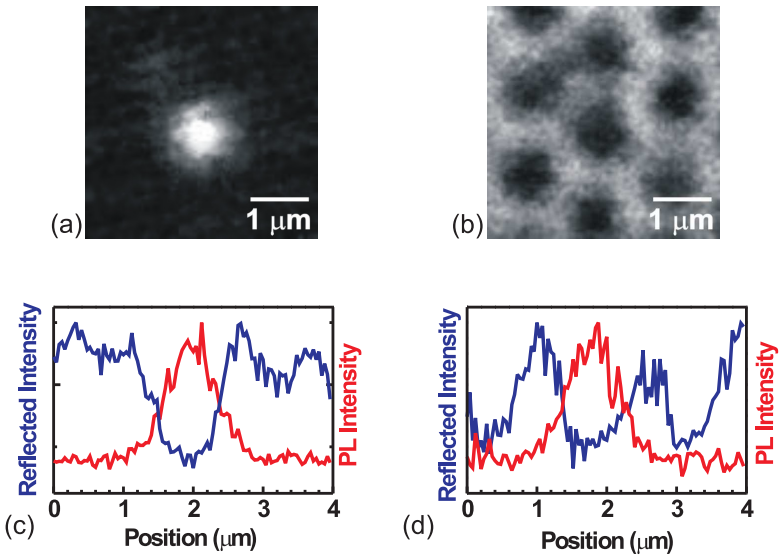

Figure 3.4: (a) Luminescence signal: a single pore of 1 μm in diameter has been infiltrated with the Rhodamine solution. (b) Reflection image of the same sample region. (c) Horizontal and (d) vertical profiles along the center of the images in a) and b). The perfect overlap between the maximum in the luminescence curves (red lines) and the minimum in the reflection curves (blue lines) confirms that the solution is present only in the single selected pore.

detecting this energy shift with opportune filters it is possible to monitor the conditions and the time evolution of the intentionally introduced defects. By collecting the emission image after one month no substantial modifications are observed. This behavior presents a great advantage, both for studying the optical properties of intentionally inserted local defects and for future applications based on the presented idea of rewritable photonic devices. Any liquid can be completely removed by adding *HF* to the liquid to dissolve the silicon oxide layer, thereby converting the hydrophilic surface to a hydrophobic surface and successive heating, and/or by using an ultrasonic bath.

Once demonstrated the feasibility of the technique, various structures are realized. Figure 3.5 shows the results for an *S4 waveguide*, obtained by reiterating a building block of four infiltrated pores organized in a bended geometry. In figure 3.5(a) the luminescence signal from the infiltrated pores is shown. Figure 3.5(b) reports the calculated band diagram associated with this structure, the calculations are performed with definite-frequency

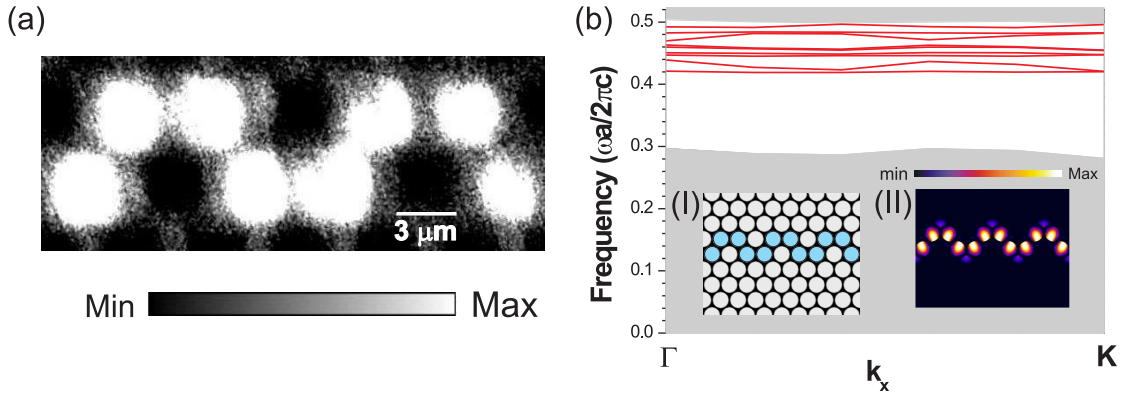

Figure 3.5: Experimental realization of an *S-shaped* waveguide. (a) CLSM image collected in emission configuration in the sample region where successive micro-infiltrations have created an S4-waveguide. (b) Calculated band diagram (for the TE modes) of the structure reported in the inset (II) that simulates the experimental realized waveguide. The bulk sample is characterized by a band gap between $\lambda = 0.3\omega a/2\pi c$ and $\lambda = 0.5\omega a/2\pi c$. The inserted waveguide determines the appearance of a miniband of guided modes around $\lambda = 0.45\omega a/2\pi c$. Inset (I) reports the variation of the dielectric constant that summarize the parameters chosen for simulating the S-shaped waveguide: pore radius, $r = 0.45a$, water dielectric constant,$\epsilon_{H_2O} = 1.77$, bulk dielectric constant, $\epsilon_{Si} = 12$. The light blue spots represent the infiltrated pores. Inset (II) reports the calculated spatial distribution of the electric field intensity associated with one of the mode introduced by the S-shaped waveguide inside the photonic band gap.

eigenstates Maxwell's equations solver free available online [9]. The inset (I) of figure 3.5(b) shows the geometry of the waveguide. The gray regions correspond to propagating modes in the bulk crystal and the white region corresponds to the photonic band gap. The *S4* waveguide introduces a mini-band of guided modes (red curves) in the band gap. As shown in the inset (I) of figures 3.5 the electromagnetic field associated with these modes is completely confined in the waveguide, demonstrating that the linear defect, introduced by the local infiltration of water, gives rise to an S-shaped waveguide in which light can propagate without losses at the sharp bends. By addressing each pore individually one can also design and realize waveguides with different refractive indices in each hole, thereby creating, e.g., adiabatic bends with extremely small losses and solving the problem of impedance mismatching between components.

3.3 Local and Re-writable light source inside a Si-based photonic crystal micro-cavity

This method is also suitable to activate passive material like silicon. In fact, the missing link between electronics and photonics is the lack of a good active element or light source based in a silicon environment. In this chapter it is shown how it is possible to introduce a local source in a silicon based photonic device, using the micro-infiltration technique. The above described infiltration technology permits to deposit, in a controlled way, a suspension of colloidal PbS quantum dots inside the central pore of a photonic crystal nano-cavity. The advantages of merging nano-fluidics with photonics imply the achievement of more functional and compact devices, also making them tunable, reconfigurable and flexible. The developed technique permits to realize and investigate a local source in a silicon photonic crystal cavity on nanometric scale. An additional feature is that the obtained functionality can be erased and rewritten.

Central idea

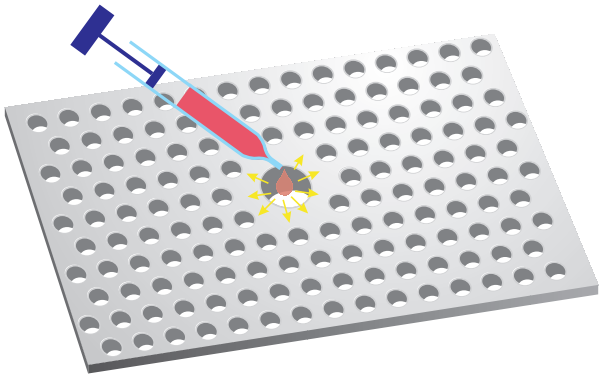

Figure 3.6: Schematic representation of the activation of a nano cavity with the infiltration process.

The opportunity to insert a light emitting element in photonic crystal nano cavities is of interest not only for the applications but also for fundamental physics research [4, 5, 10, 11, 12, 13]. In this chapter the realization of an active structure based on *local* infiltration of liquids in a photonic crystal is reported. In particular, a re-writable local source in the telecom window (at 1.3 μm) inside a silicon photonic crystal micro-cavity is realized. Even if in first experiments such quantum dot solutions were globally infiltrated in the entire photonic crystal, by simply immersing the sample in a quantum dot suspension [14, 15, 16,

17], in this case the solution is located inside only one pore of the photonic crystals. While these initial studies show that it is possible to achieve weak coupling between colloidal quantum dot sources and the modes of the photonic crystal, they do not allow to create local sources that can be combined with other functionalities in the same photonic crystals platform.

The emission spectrum of the infiltrated source is mapped with a spatial resolution of $\lambda/5$ by using a commercial Scanning Near-Field Optical Microscope. The opportunity of having simultaneously the information about the topography of the sample and the optical signal from the local source permits to localize the signal in well-defined positions around the cavity, and to access the spatial distribution of the optical modes. The spectral and spatial redistribution of the emission intensity assures the coupling between the infiltrated sources and photonic crystal cavity modes.

Sample Description

The investigated sample is a two dimensional photonic crystal cavity realized in a suspended silicon membrane with a thickness w = 260 nm. A triangular lattice of air holes with the lattice constant a = 350 nm and hole radius r = 105 nm is the underlying periodic structure. The cavity consists of an air hole, with diameter of 635 nm, that replaces the central hole and its six neighbors. See figure 3.7. The sample is fabricated on a 200 mm Silicon On Insulator (SOI) wafer from SOITEC with 1 μm silicon oxide layer and a thin top silicon layer of 260 nm thickness, by means of Electron Beam Lithography (EBL) followed by Reactive Ion Etching (RIE). A three-layer process is used for pattern transfer [18, 19]. A 500 nm-thick Shipley S18 optical resist bottom layer, a 50 nm thick *Ge* middle layer and a 150 nm-thick polymethylmethacrylate (PMMA) top layer are first deposited on SOI samples. EBL is performed on PMMA resist using a JEOL JBX5D2U vector scan generator at 50 keV energy. After developing the PMMA, patterns are transferred into the other layers by means of standard RIE with CHF_3 gas for the Ge layer and O_2 for the bottom layer. Finally, the silicon top layer (the core of the waveguide) is etched by RIE with a SF_6 and CHF_3 gas mixture under optimized conditions to obtain vertical sidewalls. The remaining resist is finally stripped off. The membrane is obtained by removing the silicon oxide layer by wet etching in a buffered HF solution. A Scanning Electron Microscope (SEM) image of the sample is provided in the inset of figure 3.7. The design and cavity mode calculations are performed by means of a guided-mode expansion method [20]. The main resonant frequency of the cavity is predicted to be near 1300 nm in order to match its resonant frequency with the emission spectrum of *PbS* Quantum Dots (QDs) suspended in toluene. The cavity structure with a large central hole is especially suited for local infiltration, in fact even if the lattice constant of the studied photonic crystals is not resolvable in this condition, the big central hole is well recognizable.

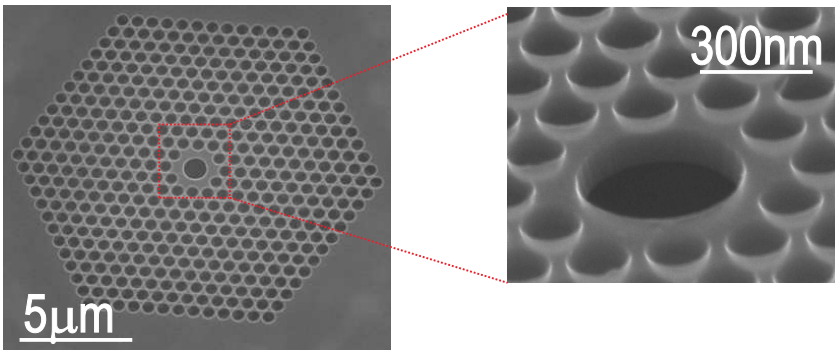

Figure 3.7: Scanning Electron Microscope image of the photonic crystal micro-cavity is provided.

3.3.1 Near-field study of a Local and Re-writable light source

The emission spectra of the infiltrated QDs is collected by using a SNOM with an etched uncoated near-field fiber probe [21] in illumination/collection configuration, as explained in the previous chapter in the section 2.2.1. The sample is excited at 780 nm with an excitation density of roughly 1 MW/cm^2 and the emission spectrum of the infiltrated QDs is collected for each position of the tip. The opportunity of having the spectral information combined with the topography of the sample permits to investigate the mode profile of the cavity and to spatially map its local DOS.

Figure 3.8 shows a typical emission spectra of the QDs as infiltrated in the micro-cavity, compared with a reference spectrum of the same QDs not embedded in a photonic structure. By considering these two spectra, it is clear that the presence of the cavity induces one defined peak centered at d 1315 nm (with a full width at half maximum of about 2 nm) and a broader band at 1257 nm, showing a clear frequency redistribution of the photoluminescence signal. The presence of these peaks assures that the emission of the QDs is coupled with the photonic crystal cavity modes. As will be shown below, these two peaks correspond to the main resonant modes of the studied photonic crystal micro-cavity.

Figure 3.9 shows some spectra collected at several positions inside (A,B,B') and outside (O) the cavity. By comparing the relative amplitudes between the two peaks at 1257 and 1315 nm it is clear that the emission is strongly dependent on position. In particular, in A the contribution of the broader mode dominates, while, outside the cavity region, the mode at 1315 nm is more intense, proving that the two modes have a distinct spatial distribution. The spectra collected in the two symmetric, and therefore ideally indistinguishable, positions (B,B') highlight the role of the disorder in the sample, which can be retraced both to fabrication and to a slightly asymmetric infiltration. In fact, although the integrated signal and the relative amplitudes between the two main cavity modes are quite similar, different

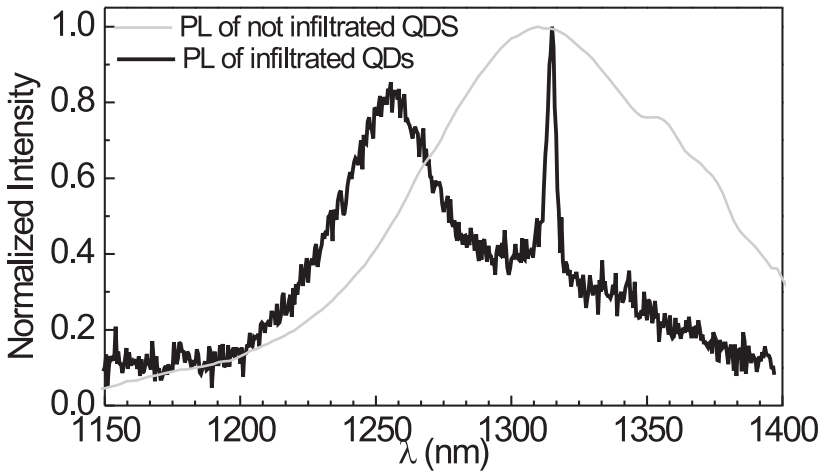

Figure 3.8: Photoluminescence spectrum of QD infiltrated inside the structures (black line) compared with the spectrum of the same QD outside the cavity (grey line).

peaks, especially at high energy, appear more evident in B' with respect to B.

The quality factor (Q) of the infiltrated micro-cavity drastically depends on the quality (grade) of the infiltration process. The introduction of an uncontrollable amount of material, like clustered QDs, inside the central hole can induce a decrease of Q.

In figure 3.10 the QDs emission spectra with two different infiltrations processes are reported. The difference in the quality of the infiltration is clearly visible comparing the topography images recorded after the infiltration process. In particular, in the topography image reported in the inset (II) the presence of clustered quantum dots in the central hole of the cavity does not permit to recognize the position of the central hole, while in the case of the inset (I) the central hole is clearly visible in the topographic image, indicating that a more clean infiltration process has been obtained. In the high quality infiltration (black line) the spectrum is red shifted and the quality factor is increased by a factor of 4 compared to the infiltration reported in gray line. In this last case, in fact, the deposition of clustered quantum dot in correspondence of the hole modify the photonic environment of the cavity and consequently decreases its Q value. To avoid the deposition of uncontrolled amount of clustered material the solution of the colloidal QDs is sonicated before performing the infiltration. Once performed the infiltration, the sample could be cleaned by immersing it in a bath of Toluene, washing it using ethanol finally letting it dry inside an oven.

From the collected data it is possible to obtain, for a selected wavelength, the spatial dis-

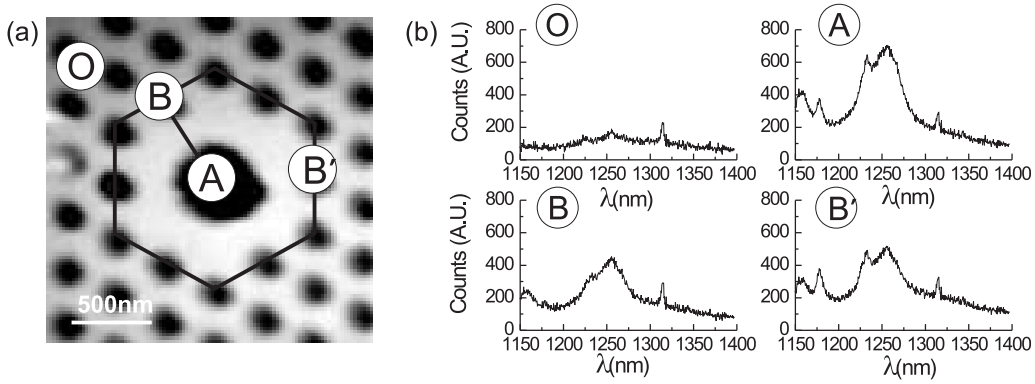

Figure 3.9: (a) Shear force topographic image (2×2 μm) recorded with the near-field scanning optical microscope; the labeled circles represent the regions where the near-field spectra are collected. (b) Near-field spectra collected for different positions indicated in the topographic image in (a).

tribution of the local source signal. Figures 3.11(a) and (b) show the spatial intensity distribution associated to the cavity peak at wavelength of 1315 nm and to the broader band at 1257 nm, respectively. The comparison between the experimental images indicates that the these spectral features present completely different spatial distributions: while the band at 1257 nm is concentrated in the center of the cavity, for the cavity peak the maximum of the signal is located outside the cavity region and it presents a preferential axis.

In order to better understand the experimental results $3D$ FDTD calculation using a commercial FDTD Maxwell equation solver are performed. The system is modeled as a free-standing photonic crystal membrane with micro-cavity, using the nominal parameters of the sample. To excite the cavity modes, the sources are placed in the central hole, whose refractive index is chosen to be 1.45 as in the experimental configuration. Figures 3.11(c) and (d) show the square of the electric field along the x-axis $(\mathrm{Ex})^2$ at a distance $d = 1.37$ μm far from the sample surface for the two modes at 1315 nm and 1257 nm, respectively. In figure 3.11(e) the experimental spectrum obtained integrating the signal in the whole scanning region is compared with the calculated one. As is evident in the results presented in figure 3.11, a good agreement with the experimental data is obtained, reproducing both the spatial distribution of the modes and the emission spectrum.

As already introduced in the previous chapter in 2.2, the exact calculation of what the near-field probe really collects requires, in principle, the knowledge of the transfer function of the SNOM tip, which depends on the tip itself. This analysis is practically not feasible, so that the problem has to be simplified. To that end, one can assume that the near-field

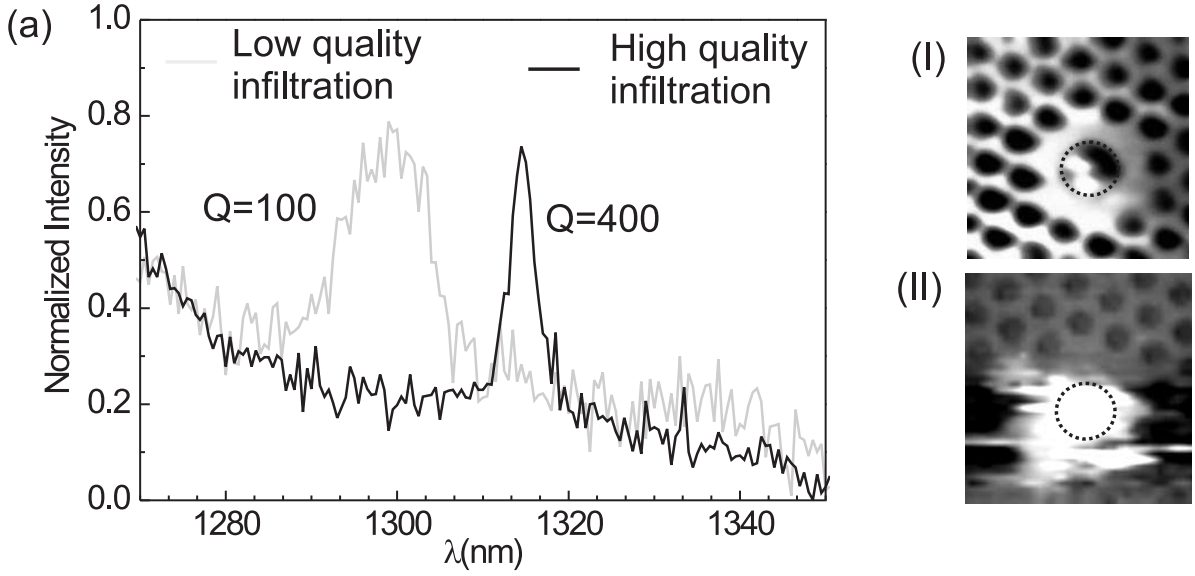

Figure 3.10: Near-field spectra related to two infiltrations performed on different samples with the same nominal parameters. If a not perfect infiltration is performed a reduction of the Q-factor by a factor of 4 is obtained. In the insets the topography images of the samples for the two different infiltrations are reported, in particular the inset (I) presents the topography image (2×2 μm) of the sample surface obtained in correspondence of the spectrum in black line, while the inset (II) corresponds to the spectrum in gray line.

map detected by the tip can be retraced by calculating the theoretical map at an effective distance d from the sample surface [22]. In this way, the value of d does not represent the real height of the tip, but it is an effective free parameter that deals with the fact that the SNOM tip does not collect only the evanescent field of the cavity, but it is also sensitive to the radiative field.

In figure 3.12 it is studied how the spatial distribution $(Ex)^2$ varies as a function of the distance d. For the case of the mode at 1315 nm (figure 3.12(a)) the electric field intensity tends to propagate in two separated angular patterns and the spatial separation between the two lobes increases with d. A good agreement with the experimental data is found for $d = 1.37$ μm (white dotted line in figure 3.12). At this distance, the calculated intensity distribution associated to the cavity modes and the spectrum of $(Ex)^2$ well reproduces the experimental results also for the modes at 1257 nm reported in figure 3.12(b). Moreover the presence of a preferential symmetry axis observed experimentally can be retraced to the presence of an asymmetry in the central cavity hole, which is also visible in the topographic

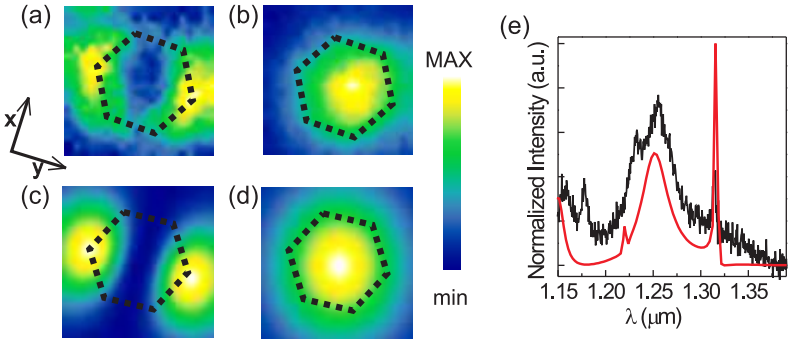

Figure 3.11: (a) and (b), Measured spatial intensity distributions associated to the cavity peak at 1315 nm, and to the broader peak at 1257 nm, respectively. At 1257 nm the emission stems predominantly from the infiltrated pore, while at 1315 nm the intensity distribution is concentrated outside that region. This is a signature that the cavity mode is anyway excited, although the electric field amplitude shows a minimum where the sources are located. (c) and (d), calculated intensity distributions of the electric field component along the x axis, at 1315 nm and 1257 nm, respectively. The size of images (a)-(d) are 2×2 μm. (e), The experimental spectrum obtained integrating all over the image (black line) is compared with the calculated spectrum of the intensity associated to the electric field component along the x axis (red line) over the same scanning region at distance d=1.36 μm.

image provided in figure 3.9(a). In particular, the calculation assures that when the central hole is elongated along the y direction, with an ellipticity of a few percent, the electric field component along the x axis Ex dominates, allowing to compare the experimental data with the $(Ex)^2$ component calculated in a circular cavity. Altogether, the agreement between theory and experiment is fully satisfactory, demonstrating that the cavity structure is close to design and that the effect of spatial and spectral redistribution on QD emission is due indeed to the occurrence of local cavity modes.

3.4 Conclusion

In this chapter a technique that permits to infiltrate, at single pore level two dimensional photonic crystals is presented. This method could be exploited not only to write and functionalize defect in photonic structures, but also to introduce local sources in a Si-based devices. The redistribution of the spontaneous emission of the light emitted by the quantum dots assure the coupling of their emission with the modes of the photonic cavity. The Q and

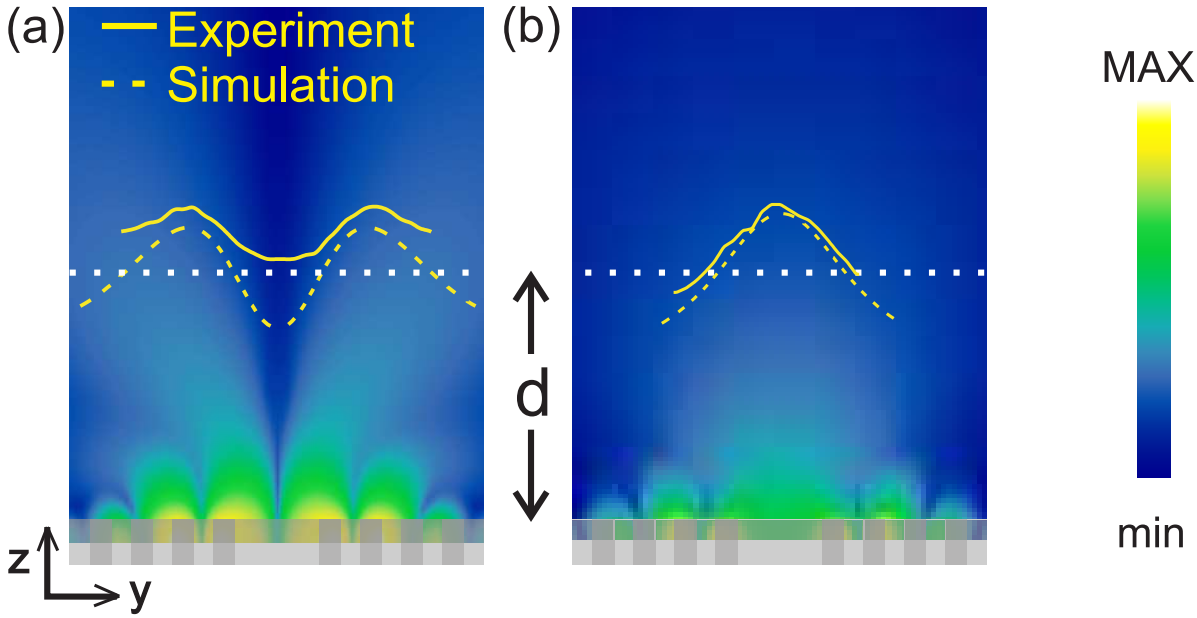

Figure 3.12: (a) and (b), Distribution of the intensity of the electric field component along the x-axis collected in a vertical plane along the y-direction and centered in the middle of the cavity (image size 2.3×3 μm) for the two cavity modes at 1315nm and for the broadened band at 1257nm. The white dotted line represents the effective height in with the simulated profile of the electric field (yellow dotted line) is collected. The yellow continuous lines represent the normalized experimental profile of the photonic crystal cavity mode.

the overall performance of the photonic microstructure in controlling spontaneous emission can be further improved, with the possibility of observing quantum electro-dynamical phenomena like the Purcell effect [23] in a Silicon environment. These results are potentially useful for application in the field of integrated emitting structures because they offer, at the same time, the flexibility to exploit local emitters in silicon substrates and the opportunity to erase and rewrite them. Also, the high sensitivity of the cavity resonance line to local refractive-index variations could be further developed and exploited for nano-scale detection purposes in a silicon environment.

Bibliography

[1] S. Fan, P. R. Villeneuve, and J. D. Joannopoulos. Channel drop tunneling through localized states. *Phys. Rev. Lett.*, 80:960, 1998.

[2] S. Noda, A. Chutinan, and M. Imada. Trapping and emission of photons by a single defect in a photonic bandgap structure. *Nature*, 407:608, 2000.

[3] S. Song, S. Noda, and T. Asano. Photonic devices based on in-plane hetero photonic crystals. *Science*, 300:1537, 2003.

[4] S. Strauf, K. Hennessy, M. T. Rakher, Y. S. Choi, A. Badolato, L. C. Andreani, E. L. Hu, P. M. Petroff, and D. Bouwmeester. Self-tuned quantum dot gain in photonic crystal lasers. *Phys. Rev. Lett.*, 96:127404, 2006.

[5] W. H. Chang, W. Y. Chen, H. S. Chang, T. P. Hsieh, J. I. Chyi, and T. M. Hsu. Efficient single-photon sources based on low-density quantum dots in photonic-crystal nanocavities. *Phys. Rev. Lett.*, 96:117401, 2006.

[6] F. Intonti, S. Vignolini, V. Turck, M. Colocci, P. Bettotti, L. Pavesi, L. S. Schweizer, R. Wehrspohn, and D. S. Wiersma. Rewritable photonic circuits. *Appl. Phys. Lett.*, 89:211117, 2006.

[7] F. Intonti, S. Vignolini, M. Colocci, and D. S. Wiersma. Photons flow in liquid circuits. *Laser Focus World*, 43:8, 2007.

[8] P. Bettotti, L. Dal Negro, Z. Gaburro, L. Pavesi, A. Lui, M. Galli, M. Patrini, and F. Marabelli. P-type macroporous silicon for two-dimensional photonic crystals. *J. Appl. Phys.*, 92:6966, 2002.

[9] S. G. Johnson and J. D. Joannopoulos. Block-iterative frequency-domain methods for Maxwell's equations in a planewave basis. *Opt. Express*, 8:173, 2001.

[10] M. Fujita, S. Takahashi, Y. Tanaka, T. Asano, and S. Noda. Simultaneous inhibition and redistribution of spontaneous light emission in photonic crystals. *Science*, 308:1296, 2005.

[11] D. Englund, D. Fattal, E. Waks, G. Solomon, B. Zhang, T. M. Nakaoka, Y. Arakawa, Y. Yamamoto, and J. Vuckovic. Controlling the spontaneous emission rate of single quantum dots in a two-dimensional photonic crystal. *Phys. Rev. Lett.*, 95:013904, 2005.

[12] S. Noda, M. Fujita, and T. Asano. Spontaneous-emission control by photonic crystals and nanocavities. *Nat. Phot.*, 1:449, 2007.

[13] K. Hennessy, A. Badolato, M. Winger, D. Gerace, M. Atatüre, S. Gulde, S. Falt, E. L. Hu, and A. Imamoglu. Quantum nature of a strongly coupled single quantum dot-cavity system. *Nature*, 445:896, 2007.

[14] I. Fushman, D. Englund, and J. Vuckovic. Coupling of PbSe quantum dots to photonic crystal cavities at room temperature. *Appl. Phys. Lett.*, 87:241102, 2005.

[15] R. Bose, X. Yang, R. Chatterjee, J. Gao, and C. W. Wong. Weak coupling interactions of colloidal lead sulphide nanocrystals with silicon photonic crystal nanocavities near 1.55μm at room temperature. *Appl. Phys. Lett.*, 90:111117, 2007.

[16] Z. Wu, Z. Mi, P. Bhattacharya, T. Zhu, and J. Xu. Enhanced spontaneous emission at 1.55μm from colloidal PbSe quantum dots in a si photonic crystal microcavity. *Appl. Phys. Lett.*, 90:171105, 2007.

[17] L. Martiradonna, L. Carbone, A. Tsndaechanurat, M. Kitamura, S. Iwamoto, L. Manna, M. De Vittorio, R. Cingolani, and Y. Arakawa. Two-dimensional photonic crystal resist membrane nanocavity embedding colloidal dot-in-a-rod nanocrystals. *Nano Lett.*, 8:260, 2008.

[18] M. Belotti, M. Galli, D. Bajoni, L. C. Andreani, G. Guizzetti, D. Decanini, and Y. Chen. Comparison of SOI photonic crystals fabricated by both electron-beam lithography and nanoimprint lithography. *Microelectron. Engin.*, 73:405, 2004.

[19] D. Peyrade, Y. Chen, A. Talneau, M. Patrini, M. Galli, F. Marabelli, M. Agio, L. C. Andreani, E. Silberstein, and P. Lalanne. Fabrication and optical measurements of silicon on insulator photonic nanostructures. *Microelectron. Engin.*, 61:529, 2002.

[20] L. C. Andreani and D. Gerace. Photonic-crystal slabs with a triangular lattice of triangular holes investigated using a guided-mode expansion method. *Phys. Rev. B*, 73:235114, 2006.

[21] R. Stoeckle, C. Fokas, V. Deckert, R. Zenobi, B. Sick, B. Hecht, , and U. P. Wild. High-quality near-field optical probes by tube etching. *Appl. Phys. Lett.*, 75:160, 1999.

[22] Y. De Wilde, F. Formanek, R. Carminati, B. Gralak, P. Lemoine, K. Joulain, J. Mulet, Y. Chen, and J. Greffet. Thermal radiation scanning tunnelling microscopy. *Nature*, 444:740, 2006.

[23] E. M. Purcell, N. Bloembergen, , and R. V. Pound. Resonance absorption by nuclear magnetic moments in a single crystal of caf_2. *Phys. Rev. Lett.*, 70:988, 1946.

4 Vortices and field correlations in the near-field speckle of a three dimensional photonic crystal with a certain degree of disorder

In this chapter an experimental study of near-field speckle observed from photonic crystals is presented and analyzed from different perspectives. Vortices in these speckle patterns and the statistical properties of their morphological parameters are observed and analyzed. This allows to make a comparison between speckle from photonic crystals and that from completely random systems. Analysis of the field correlation functions allows to determine important sample parameters like the transport mean free path, diffusion constant, and effective refractive index.

4.1 Introduction

Photonic crystals, no matter how accurately prepared, contain a certain level of disorder due to size fluctuations of the scattering elements and other structural imperfections. This disorder can be small but it usually plays an important role in determining their optical properties, especially in the case of three dimensional photonic crystals [1]. Disorder does not destroy interference, but it makes the optical behavior of photonic crystals much more complex and it gives rise to multiple scattering which leads to intensity patterns, known as speckle [2]. The phase and amplitude distributions of a speckle pattern contain important information like the local density of states [3], and exhibit interesting features like phase singularities [4, 5, 6, 7]. Even if the understanding of speckle patterns in terms of amplitude and phase for disordered systems is rapidly growing [8, 9, 10, 11, 12], little is know about their behavior in partially ordered systems like photonic crystals. In pioneering theoretical work on this topic, it was shown that the speckle generated by the intrinsic disorder in a photonic crystal contains a lot of useful information like the width of stop-band [13].

Central idea

In this chapter the experimental study and the analysis of speckle patterns generated by three dimensional photonic crystals with a certain degree of disorder are reported. This study is performed in the near-field using a phase-sensitive technique. Different properties of the speckle patterns that are known to exist in random systems are also observed in this case like for example phase singularities (vortices). Moreover, a complete characterization of the electric field for different wavelength can be used to determine sample parameters like the average refractive index, the mean free path, and the diffusion constant of photonic crystals.

4.2 Phase Singularities from a three dimensional Photonic Crystal

Phase singularities are lines in space, or points in the plane, where the phase of the complex scalar wave is undefined. The first experimental observation of phase singularities goes back to the 1973 for sound waves [4]. When an ultrasonic pulse containing few quasi-sinusoidal oscillation is reflected in air from a rough surface the scattered wave trains contains dislocation, which are closely analogous to those found in imperfect crystals. This work was originated in order to understand the radio echoes from the bottom of the Antarctic ice sheet. Up to now a lot of interesting work on phase singularities as topological objects of wave fields appears in a variety of physical scenarios, from radio wave [4], through microwaves [7] to optical frequencies [5], but also in non linear optics [14] to atomic physics [15]. In the following analysis regards optical singularities and their statistical proprieties related to speckles pattern from a three dimensional photonic crystal.

Sample description

The sample under investigation is a three dimensional photonic crystal, in particular a silica stynthetic opal grown using a dip coating technique [16]. The silica nanospheres used to realize the sample are synthesized during the hydrolysis of tetra-ethyl-ortho-silicate (TEOS) using NH_3 as a catalyst and ethanol as a solvent. To that end, given amounts of ethanol (145 mL) and ammonia (32 mL) solution are introduced into a three-neck round flask of 250 mL equipped with a refrigerating system. The mixtures are stirred in a centrifuge at 300 rpm to homogenize them. Then, an ethanolic (58 mL) solution of TEOS (14.5 mL) is prepared separately and introduced continuously in the medium at a precise rate thanks to a single-syringe pump. The reaction occurred at room temperature under continuous stirring for over 24 hours. The spheres diameter obtained in the synthesis is 730 nm, with 4% of polidisperisty. The growth of silica direct opals is performed using the dip-coating

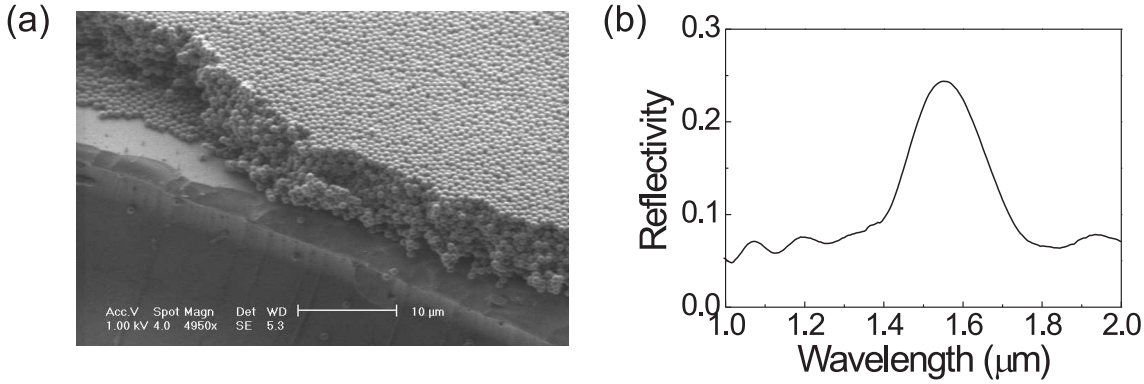

Figure 4.1: Sample description (a) Scanning Electron Microscope image of at the edge of the opal. (b) Reflection measurement along the Γ direction.

technique[16]. It consists of a self assembly method which involves placing a nearly vertical substrate in the suspension of nanospheres (0.2 vol%), as previously obtained. Under suitable conditions ($T = 20-40\circ$ C and $P = 1-10$ torr), the evaporation of the solvent, taking advantage of the meniscus forces, leads to the deposition of ordered three-dimensional packing (FCC structure with [111] plane parallel to the substrate).

A Scanning Electron Microscope image of the sample is provided in figure 4.1(a). Reflection measurements, performed along the Γ direction of the opal, exhibit a Bragg peak centered at 1550 nm with a reflectivity of roughly 30%. See figure 4.1(b). This low value of reflectivity indicates that the opal has an appreciable degree of disorder.

Setup description

In order to completely characterize the electric field in terms of amplitude and phase, the sample is studied using a near-field and phase-sensitive technique. A near-field optical microscope is incorporated into a Mach-Zehnder interferometer as shown in figure 4.2. A tunable light source is split into two parts, denoted signal and reference branch. In the signal branch linearly polarized light is coupled into the structure by focusing it at one side of the [111] plane of the opal, travel through the sample and it is finally collected by an aluminum-coated tapered probe [17]. The light from the two branches is then mixed interferometrically and collected. A set of measurements in the same zone of the sample for different incident wavelengths ranging from 1440 nm to 1590 nm are performed. This technique has been shown to be very efficient in analyzing the optical properties of photonic materials and in particular photonic crystals [18, 19, 20]. Combining a near-field microscope with an interferometer provides amplitude and phase information of the light for

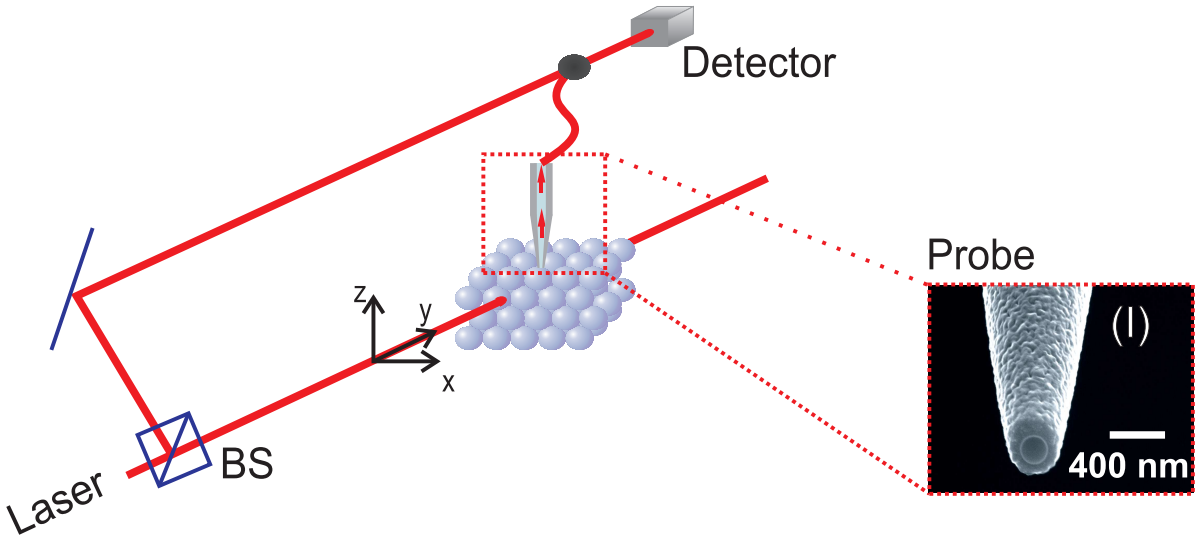

Figure 4.2: Schematic representation of the experimental setup. A tunable laser light source is coupled into the three-dimensional photonic crystal. The probe of the microscope (a scanning electron microscope image is provided in the inset (I)) collects a fraction of the field inside the sample. This light is interferometrically mixed with the reference light of the same laser. Only the resulting interference signal is recorded.

every position of the probe with a sub-wavelength resolution [21, 22].

4.2.1 Phase Singularities parametrization

To understand better the meaning of a phase singularities it is convenient to consider the conventional field representation as:

$$E(x,y) = \sqrt{U(x,y)}\exp\left[i\Phi(x,y)\right] = R(x,y) + iI(x,y), \tag{4.1}$$

where $R(x,y)$ and $I(x,y)$ are the Real and the Imaginary part of the wave function, the intensity U is

$$U(x,y) = R^2(x,y) + I^2(x,y), \tag{4.2}$$

and the phase Φ is

$$\Phi = \arctan\left[\frac{I(x,y)}{R(x,y)}\right]. \tag{4.3}$$

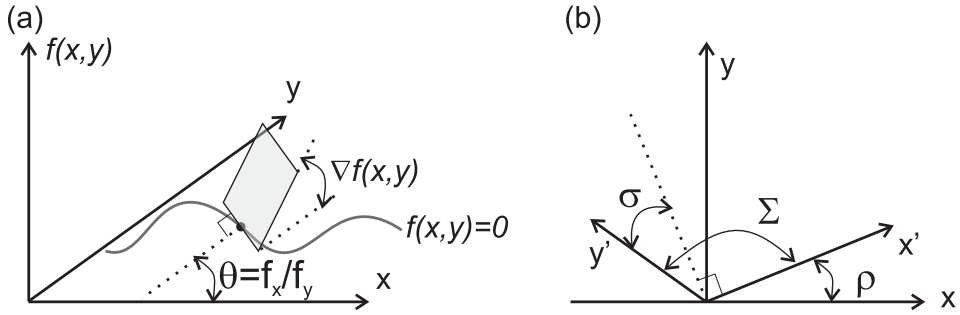

Figure 4.3: (a)Schematic representation of the geometry of the real (/imaginary) tangent plane: the angle that measure the orientation of the plane respect to the x axis is $\tan\theta_R = \frac{R_y}{R_x}$ ($\tan\theta_I = \frac{I_x}{I_y}$), while the slope of the plane is $\nabla R(x,y)$ or $\nabla I(x,y)$.(b) Vortex internal coordinates x' and y', ρ measures the rotation of the vortex coordinate system relative to the laboratory x,y frame. Σ defines the angle between the y' and x' and the σ measures the deviation from the orthogonality of the internal vortex coordinate system, skewness.

In this formalism a phase singularity is defined as a point where both the Real and the Imaginary part of the field are null and consequently the phase Φ remains undefined (singular). Since these points are first order zero of R and I in their vicinity one can consider:

$$R(x,y) = R_x x + R_y y \quad \text{and} \quad I(x,y) = I_x x + I_y y \tag{4.4}$$

where $R_i = \frac{\delta R(x,y)}{\delta i}$ and $I_i = \frac{\delta R(x,y)}{\delta i}$ with $i = x, y$ and the origin of coordinates are moved to the vortex center. From equation 4.4 it follows that four independent parameter are required for a complete characterization of the vortex wave function. Moreover in the proximity of a vortex the phase field could be written as:

$$\Phi(\theta) = \arctan\left(\frac{1 + A\tan\theta}{B + C\tan\theta}\right) \tag{4.5}$$

where $A = \frac{I_y}{I_x}$,$B = \frac{R_x}{I_x}$ and $C = \frac{R_y}{I_x}$. As Φ depends only on θ, contours of constant phase are straight lines that radiate outwards from the vortex center and form a phase star that satisfy:

$$\Phi(\theta + \pi) = \Phi(\theta) + \pi. \tag{4.6}$$

These last two equations imply that the phase is path dependent at the origin and so it is undefined (singular).

In order to describe accurately the vortex field two different parameterizations are pro-

posed [23, 24]. Even if the second type of parametrization is more intuitive, in the following analysis the first type it will be used because it is more suitable for the collected data. In the Freund parametrization the vortex field is described in terms of the local geometry of the Real an Imaginary part of the electric field. Since both functions in the proximity of a vortex center are well approximated by their tangent planes (equation 4.4), the parameter that well characterize the vortices are the slopes and the orientation of these planes. Figure 4.3 shows a schematic representation of the parameters that characterize the vortex field.

In particular, θ_R and θ_I measure the orientations of the Real and Imaginary planes respect to the x axis, respectively. While the slope of these planes are defined by $\nabla R(x,y)$ and $\nabla I(x,y)$.

By considering a new coordinate system defined as in figure 4.3(b), the vortex wave function is described as:

$$E(x',y') = a(x' + i\alpha y') \tag{4.7}$$

where a is the vortex amplitude (that is the spatial dimension of the vortex) and and α is the vortex anisotropy. In this natural coordinate system one obtain that:

where ρ is the vortex orientation angle and σ is the skewness parameter. In terms of Real and Imaginary part of the field the vortex amplitude a and the anisotropy α are:

Using these parameters the wave function is written as:

With the described parametrization the expression for the phase reported in equation 4.5 became:

$$\Phi(\theta,\alpha,\rho,\sigma) = \arctan\left[\frac{\alpha\sin(\theta-\rho-\sigma)}{\cos(\theta-\rho)}\right] \tag{4.8}$$

Once defined the parameters that completely describe the vortex it is more interesting to consider their statistical behavior. In fact, when there are many vortices, the contours of constant phase generally starts to curve as one recedes from the vortex center and the phase pattern becomes more complicated. The utility of each vortex parametrization consists in the ease and the simplicity with which the parameter of different vortices can be measured and compared.

4.2.2 Phase Singularities determination and characterization

As explained in section 4.2 the combination of a near-field microscope with an interferometer provides amplitude and phase information of the light for every position of the probe with a sub-wavelength resolution. Figure 4.4(a) shows a typical map of the electric field amplitude collected by the near-field probe where the speckle fluctuations characteristic of random systems are clearly recognizable. Figure 4.4(b) provides the map of the phase collected in the red square. To locate the vortex position accurately in the maps the lines where both $R(x,y)$ and $I(x,y)$ are zero are identified. The vortex centers are located at the crossing points of these lines. In figure 4.4(c), the zero crossing map of $R(x,y)$ (grey line)

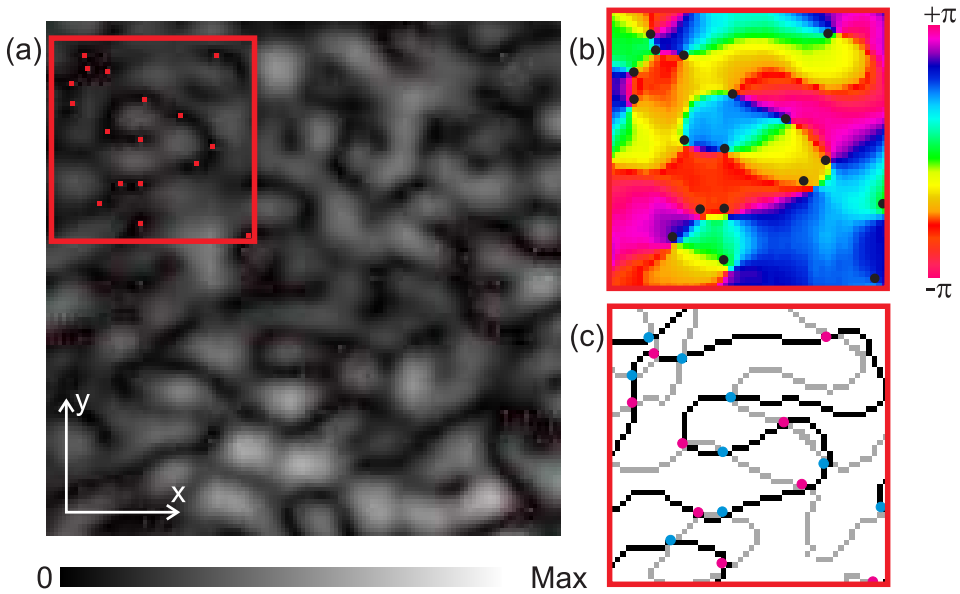

Figure 4.4: (a) Example of the electric field amplitude distribution collected by the near-field microscope at $\lambda = 1442$ nm. The red dots in correspondence of the zero values of the field amplitude correspond to the position of vortices. The dimension of the red box is 4 by 4 μm. (b) and (c) are two zooms in the zone indicated by the red square. In particular, (b) is the map of the phase as a function of position, (c) is the map of the zero lines of the real part and the imaginary part of the field. The intersections of these two lines, indicated with the colored circles, represent the position of vortices.

and $I(x, y)$ (black line) is provided. Now the vortex positions are indicated by the colored circles at the intersections between these lines.

Sign Principle

Freund *et al.* showed that these vortices must obey a fundamental sign-principle, namely that nearest neighbors on the same zero crossing line should be of opposite sign [6]. This means that, when a certain vortex has an increasing phase when rotating clockwise, its adjacent on a zero crossing should have a decreasing phase when rotating in the same direction. The reason behind this concept is topological, and should therefore hold for any type of vortex field, including that one generated by a partially disordered photonic crystal. To verify the sign principle, the derivatives of the phase at the position of the vortices are

calculated along the two directions in the plane, as:

$$\text{sign(vortex)} = \text{sign}(R_x I_y - R_y I_x) \tag{4.9}$$

This method provides a simple way of determining whether the phase increases or decrease when rotating around the phase singularity. It is observed that nearest neighbors are indeed anti-correlated. As much as 85% of the identified vortices have nearest neighbors of opposite sign. The fact that an anti-correlation of 100% is not found can be attributed to errors in the identification of vortices itself, due to the finite spatial resolution.

Vortex morphological parameters distributions

To provide a more detailed characterization of the vortex field, the vortex morphological parameters and their statistical probability densities are calculated from the experimental data. The experimental results are compared with the theoretical results for fully disordered structures [23, 25]. It is convenient to investigate the statistical behavior of the geometrical parameters associated to the tangent planes of R and I at the vortex position as presented in the section 4.2.1.

In figure 4.5(a) the angular distribution ρ is presented. This distribution shows two well-defined maxima in correspondence of $\pm\frac{\pi}{2}$. In the case of a Gaussian random wave field in the far-field the probability density for the vortex rotation angle ρ is uniformly distributed between $-\pi$ and $+\pi$ since there are not any preferred direction for the vortices. The fact that the vortices are predominantly orientated along the y axis (that is, perpendicular with respect the polarization direction) can be attributed to the polarization dependence of the speckle pattern in the near-field [26, 27, 28, 29]. Figure 4.5(b) shows the probability distribution of the vortex skewness σ folded in the interval $-\frac{\pi}{2}/+\frac{\pi}{2}$. The fact that this distribution present a maximum around the value zero assure that the vortex natural coordinate system is usually orthogonal. In figure 4.5(c) the probability distribution of the vortex anisotropy ($\alpha = \frac{\tan\phi_{Im}}{\tan\phi_{Re}}$) is reported. The most probable value of α is $\alpha = 0.75$, indicating that in most cases the vortices present a substantial degree of anisotropy. Finally, figure 4.5(d) shows the probability distribution of the vortex amplitude $a = \tan\phi_{Re}$. This probability distribution is analogous to the one calculate for the isotropic random case. The same statistical behavior of these parameters is observed for the entire wavelength range that it has been investigated in the experiments (from 1442 nm to 1527 nm). These results demonstrate that the effect of the photonic crystal in the vortex morphological parameter is irrelevant, that allows to average over all wavelengths the probability distributions reported in figure 4.5 in order to improve the signal to noise ratio of the analysis.

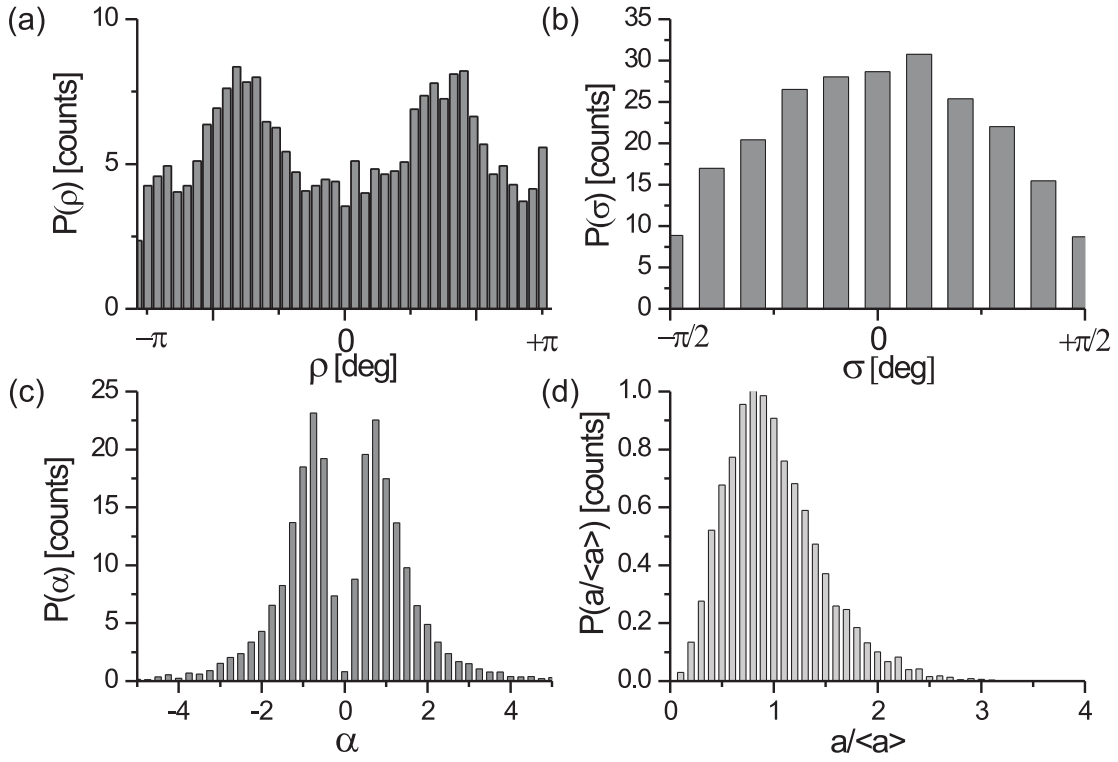

Figure 4.5: (a)-(d) Vortex morphological parameters distributions for ρ, σ, α and $a/<a>$, respectively.

Vortex spatial distributions

In addition to the morphological proprieties of the vortices, it is important to consider their spatial distribution as well [30]. From the experimental data one can observe that the vortices density is comparable, within the error, with the half of the inverse of the coherence area as expected for the far-field case. Figure 4.6(a) presents the histogram of the distance distribution between vortex centers for the first, second and third neighbors. In order to highlight effects of spatial correlation, these distances are compared with the case of a completely random distribution. After defining $\beta = d_m/d_r$ as the ratio of the measured average n-th nearest neighbor separation (d_m) to that calculated for the random distribution (d_r), it is interesting to notice that the vortices are systematically spaced more widely apart than would be expected for a purely random distribution. Figure 4.6(b) shows the values of β for the first seven neighbors, which reveals that the vortices appear to weakly repel one to

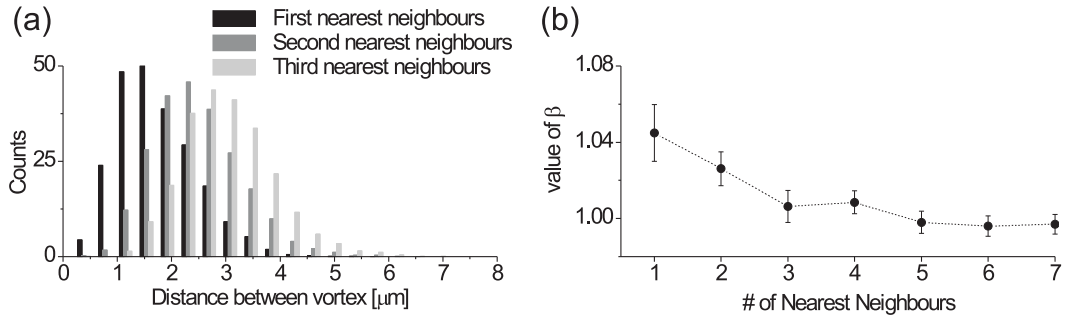

Figure 4.6: (a) Histogram of the distances distribution between vortex centers for the first, second and third neighbors. (b) Value of β for first to seventh nearest neighbors.

another, as expected theoretically [6].

4.3 Correlation properties of the Speckles Field

A speckle pattern contains vast information about the particular realization which produced it and can be described in statistical terms. The statistical properties are well represented by the correlation function, defined as:

$$C_E(\Delta x, \nu) = < E(x,\nu)E^*(x+\Delta x,\nu) > . \tag{4.10}$$

This quantity yields information about the transport proprieties of the sample that are usually hidden inside the speckle pattern. The spatial field correlation function for a fully random system is known for scalar waves and is the sum of a short range, a long range, and an infinite range contribution [11]. In most experimental configurations the short range term, which is basically a measure for the size of the speckle spots in the sample, dominates. Also in this case, it is expected that this term dominates because there is no reason a priori why the theory should apply at all, given the fact that a disordered photonic crystal is considered.

The spatial dependence of the spatial correlation funcion for a monochromatic source has been calculated in Ref. [11] and is given by:

$$C_E(\Delta x, \nu) = \frac{1}{1+2\delta}\left[\delta\frac{\sin k\Delta r}{\Delta r} + \frac{J_1(k\Delta r)}{k\Delta r}\right] \tag{4.11}$$

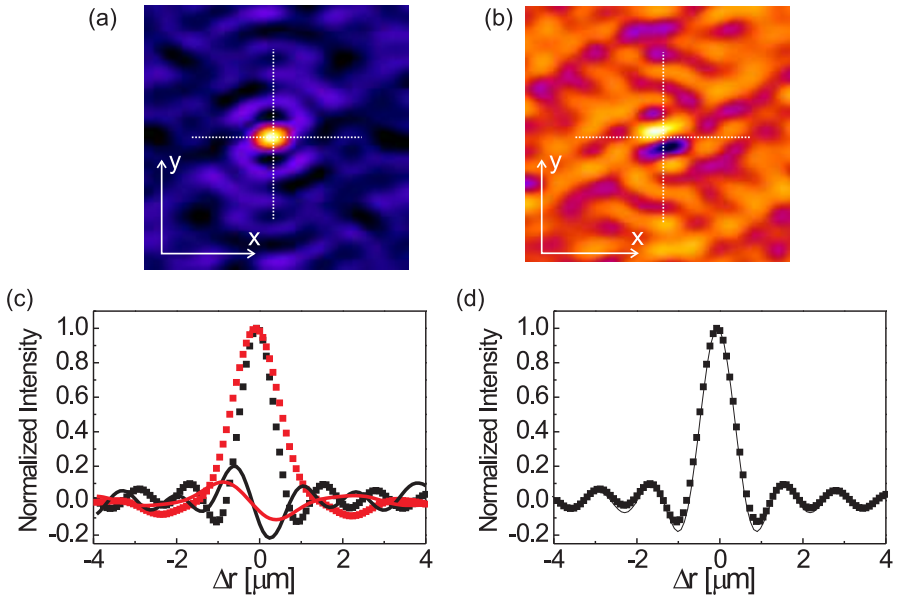

Figure 4.7: (a) Real part of the spatial correlation function of the electric field (dimensions $8x8\mu$m). (b) Imaginary part of the spatial correlation function of the electric field (dimensions $8x8\mu$m). (c) Cuts of the Real (dotted lines) and the Imaginary (straight lines) part of the spatial correlation function of the electric field, in particular the black ones are the cuts along the y axis, while the red ones are along the perpendicular direction. (d) The dotted black line reports the cut along the y direction of the real part of the correlation function, while the the black straight line is the fit of the real part of the correlation function obtained considering the theory for random systems reported in [11].

where $\delta = z_e/l_t$ depends on the extrapolation length and the transport mean free path. This expression shows that the correlation in a speckle pattern is modulated by the sync oscillating on the scale of the wavelength. Equation 4.11 predicts, for the two-dimensional correlation function, a perfect circular symmetry since it is supposed to have a perfectly random sample (no preferential directions) and because no polarization effects are considered. In the case of a photonic crystals, Shapiro in Ref. [13] shows that there is quantitative relation between the angular anisotropy of the intensity correlation function and the with of the stop band of the photonic crystal. In this case the spatial correlation function is presented in figure 4.7.

In particular, figure 4.7(a) and (b) show the Real and Imaginary part of the spatial correlation function obtained from the measurements, at $\lambda = 1442$ nm. In the figure 4.7(a) it is possible to observe an evident radial anisotropy. This preferential direction highlights a

polarization dependencies of the speckle pattern. In particular one can recognize principally two aspects: first, the spatial correlation length of the field is much larger in the direction of the polarization (x) than in the perpendicular direction. Second, there are other anisotropic features that depends on the selected direction and on the wavelength. Since the first type of anisotropy of the correlation function is independent from the wavelength, one can exclude that it is induced by the photonic structure. While in the second case, the other anisotropic features in the image are wavelength dependent and indicate an underlying spatial periodic structure.

For a complete random sample they are expected to vanish exponentially with the distance from the center. Since a complete theory that describes the near-field speckle pattern of an ordered medium with an appreciable degree of disorder is still missing, the results are compared with the ones obtained for a fully random structure. This comparison can still give some insight by looking at the similarities and differences. The fact that the correlation length is larger along the polarization direction respect to the perpendicular direction is well explained considering that speckle pattern in the near-filed is polarization dependent [26, 28, 29].

Moreover, the experimental spatial correlation profile along the y axis matches very well the theoretical curve for random systems, given by Freund *et al.* in [31]. See Fig.4.7(d). This allow to perform a fit to the value of the effective refractive index which gives the value: **n**= 1.07±0.07. This value is constant within the error for all the wavelengths considered and it is in agreement with Maxwell-Garnett theory. The profile along the x axis, on the other hand, does not have the same shape and it is not possible to find a match with the same theory 4.7(c). Figure 4.7(c) also provides the profile along the y and the x axes of the imaginary part of the spatial correlation function. This imaginary part should vanish in a homogeneous isotropic system, as can be easily seen as follows. In this case $C_E(\Delta x) = C_E(-\Delta x)$, due to translational invariance, so that $C_E(\Delta x) = C_E^*(-\Delta x)$. From the image 4.7 one can clearly see that the imaginary part is not zero but exhibits oscillations. These oscillations are most likely due to the underlying photonic crystal structure, which is spatially periodic.

By repeating the measurements for different wavelength is is also possible to calculate the spectral correlation function, defined as:

$$C_E(\Delta\nu) = < E(\nu)E^*(\nu+\Delta\nu) > . \tag{4.12}$$

Where the brackets denote an ensemble average. The correlation function is calculated from the measurements taking the average over different (distant) positions on the sample. From this quantity it is possible to to determine the diffusion constant and mean free path of a system, in fact the formal expression of this quantity is given by [11]:

$$C_E(\Delta\nu) = \frac{\sinh(q_0 a)}{\sinh(q_0 L')} \frac{\sinh(\alpha L')}{\sinh(\alpha a)} \tag{4.13}$$

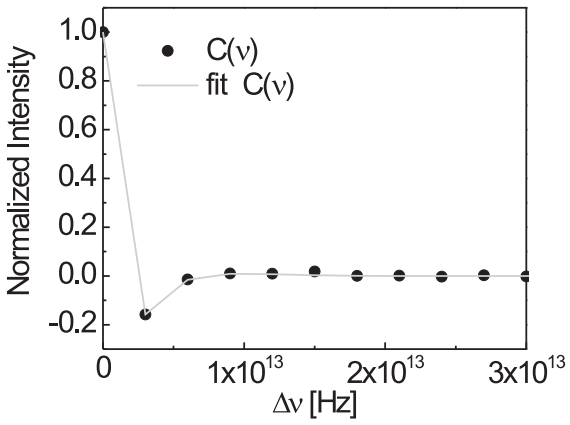

Figure 4.8: Spectral correlation function, the black dots represent the experimental data, while the grey line is the result of the fit for the spectra correlation function(as presented in [11]).

where L is the length of the sample, $L' = L + 2z_e$ is the effective length of the sample, α is the inverse of the absorption length $\alpha = 1/\sqrt{D\tau_\alpha}$ and τ_α is the absorption time and D the diffusion constant. Moreover $a = 5l_t/3$ is the randomization distance and $q_0 = 0.5(\sqrt{\alpha^4 + \beta^4} \pm \alpha^2)$ with $\beta = \sqrt{2\pi\Delta\nu}/D$.

Figure 4.8 provides the spectral correlation function, compared with theory for random systems [11]. A good agreement between the two curves is found by considering a mean free path of $l_t = 2.2 \pm 0.5\mu$m and a diffusion constant of $D = 70 \pm 10\text{m}^2/\text{s}$ fixing for the refractive index the value $n = 1.07$ obtained from the spatial correlation function, and considering the minimum sample dimension of $L = 12 \pm 2\mu$m. From the comparison the absorbtion length is considered larger than the sample thickness. As expected, different values of l_t and D can be obtained from the fit if the sample dimension is changed. $L = 12\mu$m is measured from the SEM images of the sample.

4.4 Conclusions

In conclusion in this chapter the phase and amplitude of speckle generated by photonic crystals is studied in the near-field regime. Phase singularities are observed and the statistical properties of their morphological parameters are analyzed finding analogies and differences with respect to the case of a random structures. Moreover, the field correlations of the near-field speckle are exploited to estimated from that the amount of disorder in the system. Starting from the spatial and spectral correlation function the refractive index,

the mean free path and the diffusion constant of the sample are estimated. An exhaustive theory that take into the account both the effects of random multiple scattering and the underlying photonic crystal is still missing. In order to develop it one would have to calculate the Green's function for propagation taking into account both effects. Of course this calculation should include also the polarization, that, as highlight by the measurements reported in this chapter, is expected to by very important in a photonic crystal based structure.

Bibliography

[1] A. F. Koenderink, A. Lagendijk, , and W. L. Vos. Optical extinction due to intrinsic structural variations of photonic crystals. *Phys. Rev. B.*, 72:153102, 2005.

[2] J. W. Goodman. *Statistical Optics*. John Wiley, New York, 1985.

[3] A. Z. Genack, P. Sebbah, M. Stoytchev, and B. A. van Tiggelen. Statistics of wave dynamics in random media. *Phys. Rev. Lett.*, 82:715, 1999.

[4] J. F. Nye and M. V. Berry. Dislocations in wave trains. *Proc. R. Soc. Lond. A*, 336:165, 1974.

[5] W. Wang, S. G. Hanson, Y. Miyamoto, and M. Takeda. Experimental investigation of local properties and statistics of optical vortices in random wave fields. *Phys. Rev. Lett.*, 94:103902, 2005.

[6] N. Shvartsman and I. Freund. Vortices in random wave fields: Nearest neighbor anticorrelations. *Phys. Rev. Lett.*, 72:1008, 1994.

[7] S. Zhang and A. Z. Genack. Statistics of diffusive and localized fields in the vortex core. *Phys. Rev. Lett.*, 99:203901, 2007.

[8] B. Shapiro. Large intensity fluctuations for wave propagation in random media. *Phys. Rev. Lett.*, 57:2168, 1986.

[9] A. Z. Genack. Optical transmission in disordered media. *Phys. Rev. Lett.*, 58:2043, 1987.

[10] J. H. Li and A. Z. Genack. Correlation in laser speckle. *Phys. Rev. E*, 49:4530, 1994.

[11] P. Sebbah, R. Pnini, and A. Z. Genack. Field and intensity correlation in random media. *Phys. Rev. E*, 62:7348, 2000.

[12] P. Sebbah, B. Hu, A. Z. Genack, R. Pnini, and B. Shapiro. Spatial-field correlation: The building block of mesoscopic fluctuations. *Phys. Rev. Lett.*, 88:123901, 2002.

[13] V. M. Apalkov, M. E. Raikh, and B. Shapiro. Incomplete photonic band gap as inferred from the speckle pattern of scattered light waves. *Phys. Rev. Lett.*, 92:253902, 2004.

[14] F. T. Arecchi, G. Giacomelli, P. L. Ramazza, and S. Residori. Vortices and defect statistics in two-dimensional optical chaos. *Phys. Rev. Lett.*, 67:3749, 1991.

[15] M. R. Matthews, B. P. Anderson, P. C. Haljan, D. S. Hall, C. E. Wieman, and E. A. Cornell. Vortices in a bose-einstein condensate. *Phys. Rev. Lett.*, 83:2498, 1999.

[16] P. Jiang, J. F. Bertone, K. S. Hwang, and V. L. Colvin. Single-crystal colloidal multilayers of controlled thickness. *Chem. Mater.*, 11:2132, 1999.

[17] J. A. Veerman, A. M. Otter, L. Kuipers, and N. F. van Hulst. High definition aperture probes for near-field optical microscopy fabricated by focused ion beam milling. *Appl. Phys. Let.*, 72:3115, 1998.

[18] E. Fluck, N. F. van Hulst, W. L. Vos, and L. Kuipers. Near-field optical investigation of three-dimensional photonic crystals. *Phys. Rev. E.*, 68:015601(R), 2003.

[19] K. Bittkau, R. Carius, A. Bielawny, and R. B. Wehrspohn. Influence of defects in opal photonic crystals on the optical transmission imaged by near-field scanning optical microscopy. *J. Mater. Sci.: Mater. Electron.*, pages pubblished on–line, 2008.

[20] A. Nesci, R. Dändliker, M. Salt, and H. P. Herzig. Measuring amplitude and phase distribution of fields generated by gratings with sub-wavelength resolution. *Opt. Commun.*, 205:229, 2002.

[21] B. Deutsch, R. Hillenbrand, and L. Novotny. Near-field amplitude and phase recovery using phase-shifting interferometry. *Opt. Express*, 16:494, 2008.

[22] M. L. M. Balistreri, , J. P. Korterik, L. Kuipers, and N. F. van Hulst. Local observations of phase singularities in optical fields in waveguide structures. *Phys. Rev. Lett.*, 85:294, 2000.

[23] I. Freund. Optical vortices in gaussian random wave fields: statistical probability densities. *J. Opt. Soc. Am. A*, 11:1644, 1994.

[24] Y. Y. Schechner and J. Shamir. Parameterization and orbital angular momentum of anisotropic dislocations. *J. Opt. Soc. Am. A*, 13:967, 1996.

[25] I. Freund and N. Shvartsman. Wave-fields phase singularities: The sign principle. *Phys. Rev. A*, 50:5164, 1994.

[26] V. Emiliani, F. Intonti, M. Cazayous, D. S. Wiersma, M. Colocci, F. Aliev, and A. Lagendijk. Near-field short range correlation in optical waves transmitted through random media. *Phys. Rev. Lett.*, 90:250801, 2003.

[27] J.-J. Greffet and R. Carminati. Reconstruction of the dielectric contrast profile from near-field data. *Ultramicroscopy*, 61:43, 1995.

[28] A. Apostol and A. Dogariu. Spatial correlations in the near field of random media. *Phys. Rev. Lett.*, 91:93901, 2003.

[29] C. Liu and S.-H. Park. Anisotropy of near-field speckle patterns. *Opt. Lett.*, 30:1602, 2005.

[30] N. Shvartsman and I. Freund. Wave-field phase singularities: near-neighbor correlations and anticorrelations. *J. Opt. Soc. Am. A*, 10:2710, 1994.

[31] I. Freund and D. Eliyahu. Surface correlations in multiple-scattering media. *Phys. Rev. A*, 45:6133, 1992.

5 Anderson Localization from a two dimensional photonic-crystal like structure

In this chapter is discussed the existence of spatially localized modes at the near infrared wavelengths in a system composed of a two dimensional random array of air holes embedded in a GaAs membrane of dielectric material. The near-field intensity spectra and their spatial distributions indicate waves localization in the disordered system. The spatial localization properties are not influenced by out of plane losses while the spectral properties can be dramatically modified by this extra dimension. This result can be considered as a fundamental step in the field of Anderson localization of light in high dimensional systems. Moreover, the considered samples can be analyzed as a disordered version of two-dimensional photonics crystal based devices, where the performance of the device are engineered by engineering the disorder.

5.1 Introduction

When light propagates in a structured inhomogeneous material it is multiply scattered [1], which means that it changes its direction every time it encounter with the elements that constitute such inhomogeneity (scattering elements). If the distance between two scattering events (transport mean free path) is comparable to the wavelength, the interference phenomena can lead to localization. In this condition the diffusion processes vanishes, and transport, that can not be described in a classic way, is inhibited. This peculiar regime is called Anderson Localization [2]. For three dimensional system, there is a phase transition between propagating states and localized state as a function of the disorder strength.

In the case of photons the achievement of strong scattering, that is necessary to have a sufficient disorder strength, is not trivial and consequently the realization of localizing materials is difficult [3, 4, 5]. As for every phase transition, the dimensionality of the system plays an important role. Indeed, the scaling theory predicts that for infinite system in one and two dimensions, all waves are always localized [6]. For one dimensional systems, Anderson localization has been observed for sound [7], light [8], and matter waves

[9, 10]. According with the scaling theory the two dimensional case should be the critical case: lower dimensional systems are all localized, and higher dimensional systems should present both a diffusive regime and a localized regime. The particular case of transverse Anderson localization in two dimension has been observed [11], but the observation of this phenomenon in two dimensional system is still missing.

Central idea

The main concept of the chapter is to study how it is possible to realize a complete two dimensional system that allows to achieve localization of light in the near infrared region. In this case the system consists in a high refractive index membrane with a random assembly of air pore inside. The mechanism of light localization in such two-dimensional disordered waveguides results from an interplay between the scattering from the holes and the ability of the waveguide to guide the scattered waves. This interplay between in-plane localization and lateral confinement induces the formation of modes confined in three dimensions.

Figure 5.1 illustrates schematically such process. Once light is generated or coupled inside the structure, some photons will be guided in the membrane (red arrows), while other photons will immediately leave the membrane and are lost (blue arrows). Each subsequent scattering event produces a broad range of k-vectors. The scattered waves with k-vectors below the light cone, (red arrows in the inset of figure 5.1) will be guided and scattered again, while those with k-vectors above the light cone (blue arrows in the inset of figure 5.1), will be radiated in air, and lost. This out-of-plane losses could decrease the probability of having a random path of constructive interference, hence preventing localization. To have a better idea about localization properties of a two-dimensional random array of air holes sculpted in a dielectric membrane, a series of numerical simulations are performed to investigate the role of the main parameters that define the sample. The scope of the numerical characterization is to define a windows of structural parameters that allow to grow sample where localization effects are observable.

5.2 Anderson Localization in a 2D random slab waveguide

The sample design is optimized by performing numerical calculation. By varying the filling fraction of the structure, the hole dimension and the thickness of the membrane it is possible to obtain a window of frequencies where the in-plain scattering is maximized in order to facilitate the localization process. In this condition the out of plane losses are minimized and the probability to have a random path where the constructive interference takes place is maximized.

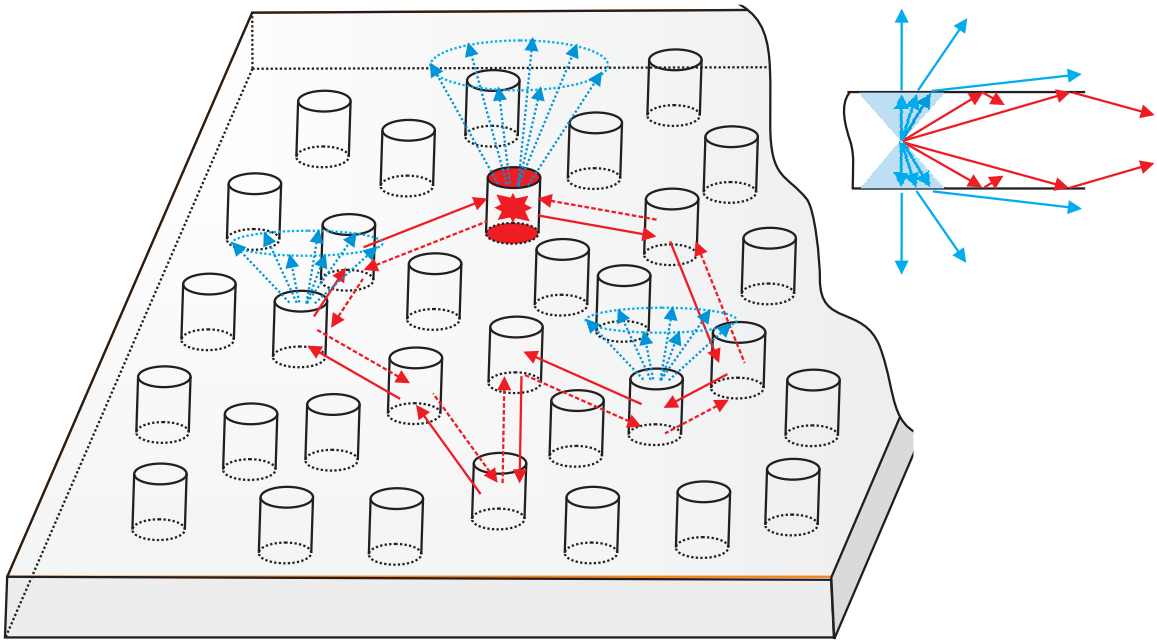

Figure 5.1: Schematic representation of light localization process in a random array of air holes embedded in a slab waveguide. The blue arrows represent the out-of-plain scattering (losses), while the red ones represent the in-plain scattering. The inset shows a cross section of the slab waveguide and it gives an intuitive explanation of the guided and radiative waves. The cyan area in the inset represents the light cone of the light that is not confined in the sample for total internal reflection.

5.2.1 Samples Design

Numerical characterization of the system has been realized solving Maxwell-Equations with a full 3D FDTD code. First simulations have been performed in pure 2D system neglecting the finite thickness of the slab waveguide. Two dimensional simulations are very fast and accurate and allow to characterize the in-plane scattering as a function of the hole diameters and filling fraction of air pores. The simulated system consists on an assembly of randomly placed circular air holes with a diameter 300 nm, in a high refractive index material ($n = 3$) with a dimensions of $25x25$ μm. The refractive index of the bulk is chosen a little bit smaller with respect to the three dimensional case in order to have (both for two and three dimension) localized state in the frequency region around 1.5μm. The diameter has been chosen in order to achieve a high scattering cross section, yet being out of the

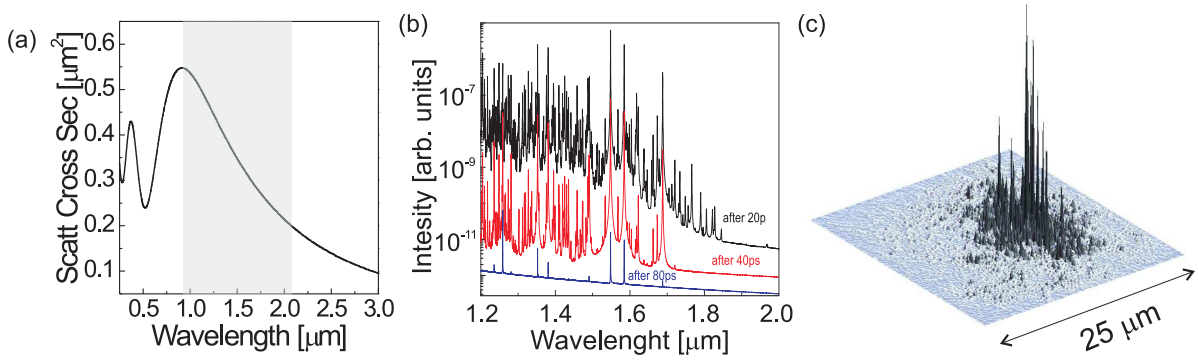

Figure 5.2: (a) Scattering cross section of an air hole of 300 nm of diameter embedded in a high index ($n = 3$) dielectric medium. (b) Spectral distribution of the intensity inside a 2D random sample for different waiting times. The spectra show a set of randomly placed peaks. Their number reduces at long waiting times, when the localized modes with long lifetime survive. (c) Spatial distribution corresponding to a long lifetime peak.

resonant Mie scattering regime. See figure 5.2(a).

The number of holes is chosen to achieve a given air filling fraction ranging from 15% to 35%. The system is excited by launching a 2-fs light pulse centered at the wavelength of 1.5 μm, from a set of randomly distributed dipole sources embedded in the medium. After a certain waiting time the averaged signal from a set of random detectors embedded in the matrix is recorded. By varying this delay time from 20 to 80 ps, it is possible to characterize both the spectrum and the decay rate due to the in-plane losses.

Figure 5.2(b) shows the spectral distribution of the intensity averaged in many position of the sample (where are placed the detectors) after waiting times of 20, 40, and 80 ps in the case of a sample with a filling fraction of air holes of about 35%. The spectral distributions of the intensity shows a peaked structure, characteristic for a localizing system. At long waiting times, only the long-lived (localized) modes survives. In figure 5.2(c) the spatial intensity map associated to a long lifetime peak is shown. The light associated to that mode is spatially confined in a definite sample region and the localization length is about 2 μm. By increasing the filling fraction, the localization length decreases, and the spatial confinement is improved.

To estimate the feasibility of a real experiments on light localization in the real system, full 3D FDTD simulations are performed, considering also the finite thickness of the slab waveguide. The excitation and detection are maintained in the same configuration than in the pure 2D calculation presented above. In the 3D FDTD simulation window the slab thickness is 250 nm and the refractive index of the slab is $n_{slab} = 3.5$. The planar dimension

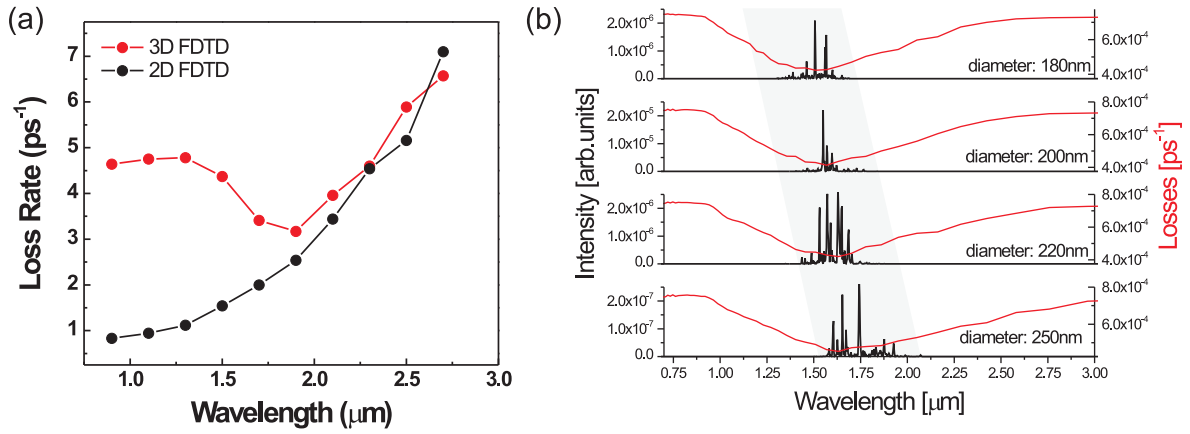

Figure 5.3: (a) Loss rate of the pure two-dimensional system (black points) and of the three dimensional one (red points), where also the finite thickness has been considered. The minimum of the loss rate (between about 1.5μm and 2.2μm wavelength) identifies the best spectral window for long-lived modes to form. This spectral region is defined as the optimum localization window.(b) Loss rate (red lines) and and long lived spectra (blue lines) obtained in a full three dimensional calculation for the case of filling fraction 25% and for four different hole diameter: 180,200,220 and 250 nm.

of the membrane is 25 x 25 μm and it is surrounded by a 2 μm of top/bottom air cladding with a 1 μm of perfect matching layer surrounding the whole simulation box.

Figure 5.3(a) shows the loss rate in these 3D simulations, compared to the 2D cases. At long wavelengths, the characteristic time of the modes is mainly determined by the in-plane losses for the both cases. On the opposite, for short wavelength, the out-of-plane losses are dominant in the 3D system. It follows that, due to the sum of these in- and out-of-plane losses, a spectral region forms having longest-lived modes. The position of this region (localization windows) varies with the hole diameter and the slab thickness, and its width with the density of scatterers. In particular, for a fixed filling fraction of 25%, increasing the dimension of the pores, the localization windows is red-shifted. See figure 5.3(b).

The realized sample consists of a 260 nm-thick planar waveguide of GaAs in which are drilled by chemical etching a 25 x 25 μm arrays of air holes, placed at random positions. A first series of sample has been taken varying the holes diameter (180 nm, 200 nm,220 nm,250 nm), and the filling fraction (15%, 20%, 25% and 30%). Other four series are achieved by over-exposing the previous samples. In this way it is possible to increase the air filling fraction, conserving a constant scatterers density.

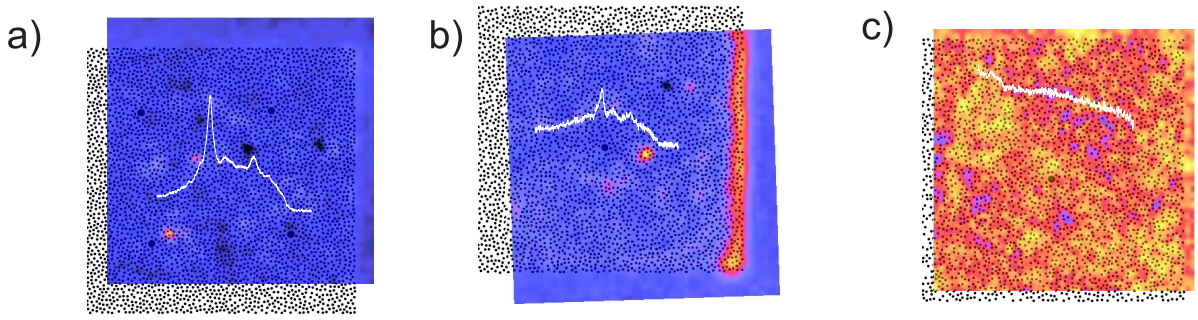

Figure 5.4: Intensity distribution of modes for samples with filling fraction of $f = 30\%$ (a), $f = 25\%$ (b) and $f = 20\%$. The white line superimposed on the image is the wavelength spectrum taken at the maximum intensity of the mode. The random dielectric matrix is superimposed to the intensity profiles together with the wavelength spectrum (white curves) of a typical mode.

In order to activate the samples, the structures are infiltrated with a suspension of colloidal PbS quantum dots diluted in Toluene [12, 13, 14, 15, 16, 17]. In this experiment two different QDs solution are used to activate the structure. In one case the emission of the QDs is centered at roughly 1.3 μm in the other is instead centered around 1.55 μm. Both the suspension have a luminescent signal characterized by a spectral width of 200 nm. The resulting active sample consists therefore of a porous membrane completely infiltrated with QDs.

The sample is then studied using a SNOM in illumination/collection geometry as already reported in 2.2. The luminescence of the QDs is excited through the SNOM tip using a diode laser surce at 780 nm, dispersed in a monochromator and then detected with a cooled InGaAs array. In this configuration it is possible to record for every position of the sample the emission spectrum of the infiltrated QDs. The spatial and the spectral resolution obtained in the measurement are 250 nm and 0.5 nm, respectively.

5.2.2 Near-field characterization

Experimental near-field Intensity maps of the whole set of samples show different spectral and spatial features when sample with different filling fraction or hole diameters are measured. Figure 5.4 shows the spatial intensity distribution (superimposed to the random dielectric matrix) associated to the most significant spectral features that one can recognize scanning through samples with different parameters. In particular, form figure 5.4(a) to (c) the filling fraction decreases from 30% to 20%. Samples with a filling fraction of 30% show many peaks (with similar characteristic to the one presented with white curves in figure 5.4(a)), while decreasing the filling fraction to 25% the density of peaks per unit wavelength

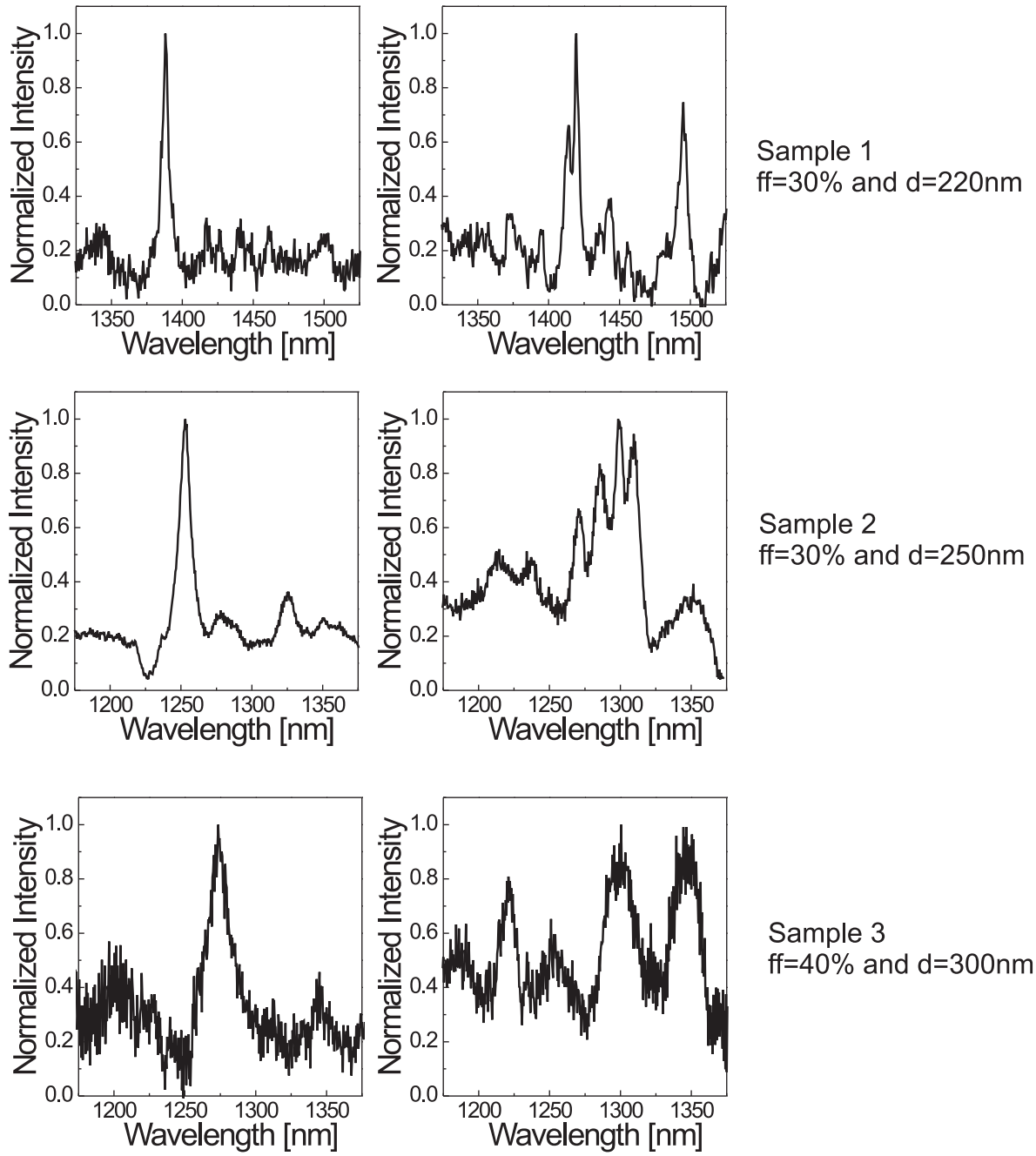

Figure 5.5: Experimental near-field spectra for three different samples (Sample 1, Sample 2 and Sample 3) with different filling fraction and holes diameter.In particular, sample 1 has a $ff = 30\%$ and $d_{holes} = 220$nm, sample 2 has a $ff = 30\%$ and $d_{holes} = 250$nm and finally sample 3 has $ff = 45\%$ and $d_{holes} = 300$nm. The first column show three classes of spectra-single peaks while the second column reports three examples of coupled peaks). Each sample above 25% of filling fraction shows peaks but with a different probability.

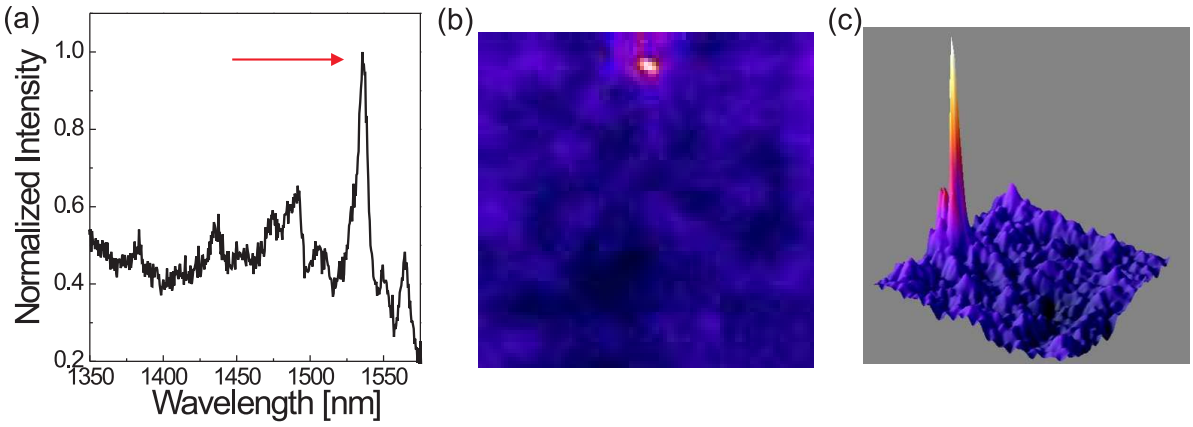

Figure 5.6: (a) Example of a near-field spectrum obtained in the Sample 1. (b) Spatial intensity distribution associated to the peak reported in the spectrum in (a). The spatial dimension of the images is $13.5x13.5\mu$m. The spatially localized mode is well confined within the sample covering a large number of scatters. (c) Three-dimensional view of the image in (b).

and unit area decreases. Finally peaks disappears in sample with filling fraction equal to 20%.

Light localization properties are thus investigated in sample with filling fraction higher than 25% varying also the hole diameter of the air scatters. Figure 5.5 shows a collection of experimental spectra of sample with filling fraction and holes diameters ranging from 30% $< f <$ 45% and 220 nm$< d_{holes} <$300 nm, respectively. In this figure the the main representative examples of measured spectra are reported. In the following these three sample will be nominated as Sample 1, Sample 2 and Sample 3.

Spectra with single, isolated peaks, as well as coupled peaks or bunch of peaks are observed. All samples above the threshold of $f >$ 25% are able to support all kind of these spectra. The main difference between samples is the probability to find each class of spectra. In particular the first line of the images matrix shows typical spectra of sample with a filling fraction of 30% and hole diameters of 220 nm. In these samples are observed spatial regions with spectra characterized by a single resonant peak (SP-spectra) and regions with spectra characterized by coupled peaks (CP-spectra).

Increasing both the hole diameter and filling fraction (second and third line of the image's matrix) a similar peaks zoology is observed. The building block of each class of spectra has Lorentian line-shape with a well defined average FWHM that increase as the filling fraction increase.

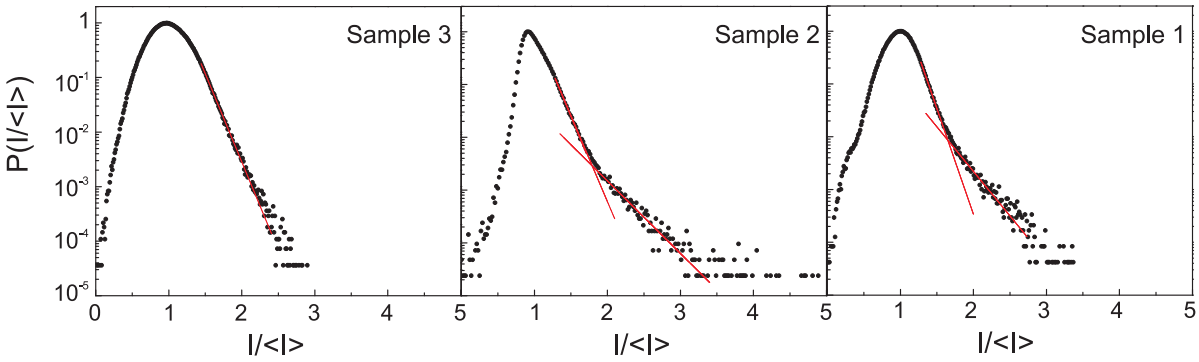

Figure 5.7: Near-field intensity distribution for Sample 3, Sample 2 and Sample 1, analyzed in figure 5.5. The high intensity tail in sample 3 can be fitted with a single exponential, while the high intensity tail of Sample 2 and Sample 1 can show a deviation from the single exponential behavior.

Figure 5.6(b) shows a typical near-field map of a well localized mode obtained in the case of Sample 1. The localized mode is composed of a main lobe covering a large number of scatters and several less intense bright spot surrounding it. Figure 5.6(c) is three dimensional rendering of the same mode.

Further information about light localization behavior can be extracted from the intensity distribution associated to the peaks. Figure 5.7 shows the near-field intensity distribution for the three samples analyzed in figure 5.5. Because the lack of a theory about near-field statistic in two dimensional confined (out of plane losses) random system, it is not possible to fit the data with a well defined function. In any case a clear difference between the intensity statistics in the three sample is clear. In particular, the intensity distribution of Sample 3 can be easily fitted with a single exponential, while the intensity distributions of Sample 2 and Sample 1 show a clear deviation from the single exponential behavior. The change in slope can be considered as an indication of the emergence of rare high intensity events, corresponding to spatially localized modes.

In order to characterize the losses of the system the behavior of the average spectral width as a function of the sample parameters is studied. Figure 5.8(a) shows the experimental average FWHM of the Lorenzian as a function of the density of holes, for different hole diameters. For a fixed hole diameter the average spectral width increase linearly with the density of holes and decrease for smaller hole diameters.

Finally in order to have a complete characterization of localization properties the average spatial extension of localized modes as a function of samples parameters is considered. Figure 5.8(b) shows the mean spatial radius of the localized modes as a function of the hole diameter for a given filling fraction. Although the overall variation of the mean spatial

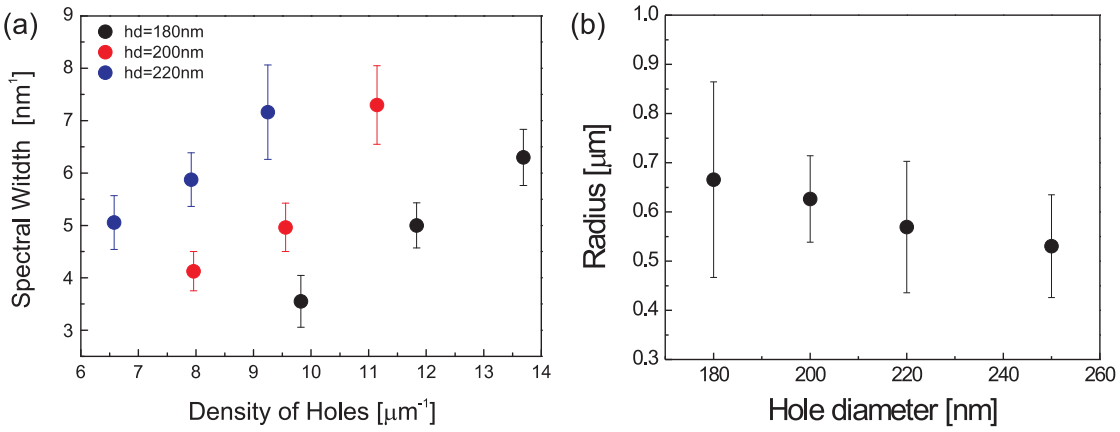

Figure 5.8: Average spectral width as a function of the density of holes for samples with different holes diameter. The average spectral width decrease, decreasing the hole diameter. b) Average spectral width of localized modes as a function of the hole diameter for fixed filling fraction.

width is small, the trend is clearly observable. Indeed the mean spatial width decreases as the hole diameter increase.

5.3 Conclusion

Combining together spatial and spectral results it is possible to draw a consistent interpretation of the experimental results showed above. Indeed, the experimental results presented in the chapter shows that it is possible to detect localized modes only above a certain filling fraction that is around $f = 25\%$.

By increasing the density of holes, the samples start to show randomly positioned resonant peaks in the near-field spectra that correspond to spatial localized modes inside the random system. Moreover, increasing the filling fraction or the hole diameter, the in plane scattering strength increases hence decreasing the mean radius of the modes. If the scattering strength increase also the losses increase, as a consequence this out-of-plane scattering strength induces a spectral broadening of the resonant peaks in the spectra. Increasing the scattering strength of the sample, localized modes are forced to be confined in a smaller spatial region at the expense of an increase of the out-of-plane radiated light. The overall variation of the spectral width is significative (about a factor of four), while the overall variation of the spatial width is very small being of the order of 30%. This trend is very similar

to those observed in two-dimensional photonic crystals cavities on slab waveguide, where a small variation in the hole position around the cavity induces a strong variation in the lifetime of the photonic mode [18], while the spatial profile is almost conserved. This system can be seen as a disordered version of the typical photonic systems studied for telecom applications. As a certain amount of disorder is unavoidable in the realization of such systems, these observation can help to study the future issues that will have to be faced for the engineering of such systems.

Bibliography

[1] P. Sheng. *Introduction to wave scattering, Localization and Mesoscopic phenomena*. Acedemic Press, San Diego, 1996.

[2] P. W. Anderson. Absence of diffusion in certain random lattices. *Phys. Rev. Lett.*, 109:1492, 1958.

[3] E. Abrahams, P.W. Anderson, D. C. Licciardello, and T. V. Ramakrishnan. Scaling theory of localization: Absence of quantum diffusion in two dimensions. *Phys. Rev. Lett.*, 42:673, 1979.

[4] D.S Wiersma, P. Bartolini, A. Lagendijk, and R. Righini. Localization of light in a disordered medium. *Nature*, 390:671, 1997.

[5] S. Zhang, B. Hu, P. Sebbah, and A. Z. Genack. Speckle evolution of diffusive and localized waves. *Phys. Rev. Lett.*, 99:063902, 2007.

[6] E. Abrahams, P. W. Anderson, D. C. Licciardello, and T. V. Ramakrishnan. Scaling theory of localization: Absence of quantum diffusion in two dimensions. *Phys. Rev. Lett.*, 42:673, 1979.

[7] R. L. Weaver. Anderson localization of ultrasound. *Wave Motion*, 12:129, 1990.

[8] Z.Daozhong, Hu Wei, Zhang Youlong, Li Zhaolin, Cheng Bingying, and Yang Guozhen. Experimental verification of light localization for disordered multilayers in the visible-infrared spectrum. *Phys. Rev. B*, 50:9810, 1993.

[9] G. Roati, C. D'Errico, L. Fallani, M. Fattori, C. Fort, M. Zaccanti, G. Modugno, M. Modugno, and M. Inguscio. Anderson localization of a non-interacting bose-einstein condensate. *Nature*, 453:895, 2008.

[10] J. Billy, V. Josse, Z. Zuo, A. Bernard, B. Hambrecht, P. Lugan, D. Clément, L. Sanchez-Palencia, P. Bouyer, and A. Aspect. Direct observation of Anderson localization of matter waves in a controlled disorder. *Nature*, 453:891, 2008.

[11] T. Schwartz, G. Bartal, S. Fishman, and M. Segev. Transport and Anderson localization in disordered two-dimensional photonic lattices. *Nature*, 446:52, 2007.

[12] F. Intonti, S. Vignolini, V. Turck, M. Colocci, P. Bettotti, L. Pavesi, L. S. Schweizer, R. Wehrspohn, and D. S. Wiersma. Rewritable photonic circuits. *Appl. Phys. Lett.*, 89:211117, 2006.

[13] S. Vignolini, F. Riboli, F. Intonti, M. Belotti, M. Gurioli, Y. Chen, M. Colocci, L. C. Andreani, and D. S. Wiersma. Local nanofluidic light sources in silicon photonic crystal microcavities. *Phys. Rev. E*, 78:045603(R), 2008.

[14] I. Fushman, D. Englund, and J. Vuckovic. Coupling of PbSe quantum dots to photonic crystal cavities at room temperature. *Appl. Phys. Lett.*, 87:241102, 2005.

[15] R. Bose, X. Yang, R. Chatterjee, J. Gao, and C. W. Wong. Weak coupling interactions of colloidal lead sulphide nanocrystals with silicon photonic crystal nanocavities near 1.55μm at room temperature. *Appl. Phys. Lett.*, 90:111117, 2007.

[16] Z. Wu, Z. Mi, P. Bhattacharya, T. Zhu, and J. Xu. Enhanced spontaneous emission at 1.55μm from colloidal PbSe quantum dots in a si photonic crystal microcavity. *Appl. Phys. Lett.*, 90:171105, 2007.

[17] L. Martiradonna, L. Carbone, A. Tsndaechanurat, M. Kitamura, S. Iwamoto, L. Manna, M. De Vittorio, R. Cingolani, and Y. Arakawa. Two-dimensional photonic crystal resist membrane nanocavity embedding colloidal dot-in-a-rod nanocrystals. *Nano Lett.*, 8:260, 2008.

[18] Y. Akahane, T. Asano, B. S. Song, and S. Noda. High-Q photonic nanocavity in a two-dimensional photonic crystal. *Nature*, 425:944, 2003.

Conclusion

In this thesis complex photonic nano-structures from perfect periodic to completely random ones are studied and modified by using a scanning near-field microscope.

For the ordered case, and in particular for two dimensional photonic crystal nanocavity is presented a method to finely correct and dynamically tune the cavity resonances. In the second chapter it is demonstrated that the interaction between the SNOM probe and the photonic structures spectrally shift the cavity modes and since it is proportional to the electric field intensity, can be exploited to map local density of state associated to the mode with an optical resolution resolution smaller than $\lambda/13$. In the same chapter an additional dynamic tuning effect can be obtained by locally heating the sample by exploiting the near field probe. Also in this case the tuning method has the advantage of being completely reversible and allows to continuously tune the resonance of the cavity with no substantial reduction of the Q value. By combining spectral and spatial information supplied by this technique it is possible to exploit the mode itself as a local probe for the temperature in photonic crystal structures. At the end of the chapter a method to obtain polarization-sensitive map of the photonic crystal cavity mode is presented, the polarization information permits to access not only to the intensity associated to the total electric field inside these kind of structures but also to their in-plane components with a no-diffraction limited resolution. In the third chapter is presented a method that permits to write into two dimensional photonic crystal all the necessary components to realize a photonic circuit. This technique is exploited to introduce local sources in a Si-based two dimensional photonic crystal nanocavity.

In the second part of the thesis the role of disorder in perfect periodic structures is considered. By analyzing the near-field speckle generated by a three dimensional photonic crystals phase singularities are observed and the statistical properties of their morphological parameter are analyzed finding analogies and differences with respect to the case of a random structures. Moreover, from the spatial and spectral correlation function the refractive index, the mean free path and the diffusion constant of the sample are estimated.

In the last part of the thesis two dimensional random structures are studied. Combining the spatial and spectral information provided by the SNOM localized modes are observed. The result presented in the last chapter of this thesis can be considered as a fundamental step in the field of Anderson localization of light in high dimensional systems. Moreover, the considered samples can be analyzed as a disordered version of two-dimensional

photonics crystal based devices, where the performance of the device are engineered by engineering the disorder.

Ringraziamenti

Il primo ringraziamento è per Diederik, che durante questo dottorato mi ha permesso di lavorare in piena libertà, mostrandosi sempre pronto al dialogo e aperto alle mie iniziative. Un grazie, altrettanto importante, va a Francesca che ha saputo starmi vicina e mi ha costantemente incoraggiata in questi tre anni. Ringrazio Massimo, Anna e Marcello che mi hanno dato la possibilità di lavorare con loro e dai quali ho imparato tanto.

Un ringraziamento speciale va senza dubbio anche alle persone con cui ho condiviso la quotidianità in questi tre anni: per prima Costanza. La sua amicizia è stata davvero preziosa per me. Un grazie anche agli altri componenti (ed ex componenti) del gruppo: Stefano, Francesco, Margherita, Jacopo, Pier e infine Riccardo, i cui consigli mi hanno fatto capire che questo lavoro mi piace davvero. Grazie anche a David e a Cefe cuin cui ho avuto la possibilità di lavorare a Madrid senza mai sentire la nostalgia di casa. Infine un grazie è d'obbligo per Matteo e Kobus che mi hanno accolto nella fredda Amsterdam.

Un ringraziamento di cuore va alla mia famiglia, ai miei genitori Carlo e Carla e a mia sorella Giulia. Loro mi hanno sempre incoraggiata e accompagnata in questo cammino così diverso da quello che prima di cominciare questo dottorato mi sarei mai potuta aspettare. Infine grazie a Lorenzo, Alberto, Francesco, Anna, Silvia, Marta e Alessio che mi hanno sempre capita e aiutata in tutte le mie decisioni. Sintetica anche nei ringraziamenti non avrò sicuramente reso l'idea di quanto la vostra presenza sia stata importante per me, ma per questo c'è sempre tempo...

List of publications related to this thesis

Near-field imaging of coupled photonic crystal microcavities

S. Vignolini, F. Intonti, M. Zani,F. Riboli, D. S.Wiersma, L. Balet, L. H. Li, M. Francardi, A. Gerardino, A. Fiore, and M. Gurioli

Appl. Phys. Lett., **94**, 151103, (2009).

Polarization-sensitive near-field investigation of photonic crystal microcavities

S. Vignolini, F. Intonti, F. Riboli, D. S.Wiersma, L. Balet, L. H. Li, M. Francardi, A. Gerardino, A. Fiore, and M. Gurioli

Appl. Phys. Lett. **94**, 163102, (2009).

Local nanofluidic light sources in silicon photonic crystal microcavities

S. Vignolini, F. Riboli, F. Intonti, M. Belotti, M. Gurioli, Y. Chen, M. Colocci, L. C. Andreani, and D. S. Wiersma

Phys. Rev. E, **78**, 45603(R), (2008).

Nonlinear optical tuning of photonic crystal microcavities by near-field probe

S. Vignolini, F. Intonti, L. Balet, M. Zani, F. Riboli, A. Vinattieri, D. S.Wiersma, M. Colocci, L. H. Li, M. Francardi, A. Gerardino, A. Fiore, and M. Gurioli

Appl. Phys. Lett., **93**, 023124, (2008).

Spectral tuning and near-field imaging of photonic crystal microcavities

F. Intonti, S. Vignolini, F. Riboli, A. Vinattieri, D. S. Wiersma, M. Colocci, L. Balet, C.Monat, C. Zinoni, L. H. Li, R. Houdre,M. Francardi, A. Gerardino, A. Fiore, and M. Gurioli.

Phys. Rev. B, **78**, 41401(R), (2008).

Near-field mapping of quantum dot emission from single-photonic crystal cavity modes

F. Intonti, S. Vignolini, F. Riboli, A. Vinattieri, D.S. Wiersma, M. Colocci, M. Gurioli, L. Balet, C. Monat, L.H. Li, N. Le Thomas, R. Houdre, A. Fiore, M. Francardi, A. Gerardino, F. Roemer and B. Witzigmann

Phys.E, **40**, 1965, (2008).

Rewritable photonic circuits

F. Intonti, S. Vignolini, V. Turck, M. Colocci, P. Bettotti, L. Pavesi, L. S. Schweizer, R. Wehrspohn, and D. S. Wiersma.

Appl. Phys. Lett., **89**, 211117, (2006).

Fotonica liquida

S. Vignolini, F. Intonti, M. Colocci, and D. S. Wiersma.

Le Scienze, **474**, 100, (2008).

Photons flow in liquid circuits

F. Intonti, S. Vignolini,M. Colocci, and D. S.Wiersma.

Laser FocusWorld, **43**, 8, (2007).

Vortices and field correlations in the near-field speckle of a three dimensional photonic crystal

S. Vignolini, M. Burresi, S. Gottardo, K. L. Kuipers, and D. S. Wiersma

in preparation.

Complete Trapping of Light by Anderson localization

F. Riboli, S. Vignolini, P. Bartelemy, F. Intonti, S. Combrie, A. de Rossi and D. S. Wiersma

in preparation.

Contacts: vignolini@lens.unifi.it

http://www.complexphotonics.org/